Fakultät für Naturwissenschaften

Tailored non-linear processes for quantum technologies

Once upon a time-frequency...

Author
Jano Gil Lopez

Supervisor
Prof. Dr. Christine Silberhorn

Tailored non-linear processes for quantum technologies

Der Naturwissenschaftlichen Fakultät
der Universität Paderborn
zur Erlangung des Doktorgrades
Dr. rer. nat.
vorgelegt von

JANO GIL LOPEZ

2021

Erklärung der Selbstständigkeit

Hiermit versichere ich, die vorliegende Arbeit selbstständig verfasst und keine anderen als die angegebenen Quellen und Hilfsmittel benutzt sowie die Zitate deutlich kenntlich gemacht zu haben.

Paderborn, den November 28, 2021 Jano Gil Lopez

Erstgutachter:	Prof. Dr. Christine Silberhorn
Zweitgutachter:	Prof. Dr. Marc Aßmann
Vertreter des Mittelbaus:	Dr. Matthias Reichelt
Vorsitzender der Prüfungskommission:	Prof. Dr. Artur Zrenner
Tag der Abgabe:	29.11.2021

Contents

Erklärung der Selbstständigkeit **A**

Summary **V**

Zusammenfassung **VII**

Preface **IX**

Introduction **1**

I Theoretical framework **3**

1 Waveguides in a nutshell **5**
1.1 Waveguide field confinement and modes 6
1.1.1 Guided modes in the asymmetric slab 7

2 Non-linear optics **11**
2.1 The non-linear polarization 11
2.1.1 Non-linear polarization density 13
2.2 Non-linear coupled-wave equations in waveguides 13
2.2.1 Quasi-phase-matching and periodic poling 15
2.2.2 Phase-matching function 16
2.2.3 Evolution and efficiency of the generated field 17
2.3 Pulsed non-linear processes 18
2.3.1 Efficiency of pulsed processes 19
2.3.2 The transfer function 19
2.4 Non-linear waveguide platforms 20
2.4.1 Lithium niobate 21
2.4.2 Titanium diffused LN waveguides 22
2.4.3 Potassium titanyl phosphate 22
2.4.4 Rubidium exchanged KTP waveguides 23

2.5 Waveguide inhomogeneities and where to find them . . . 24

3 A quantum language **27**
3.1 Hilbert spaces and the quantum alphabet . . . 28
3.2 Operators and projectors: reading quantum states . . . 29
3.2.1 Projectors . . . 29
3.2.2 Reading quantum states . . . 30
3.3 Encoding information in photon states . . . 31
3.3.1 Temporal modes . . . 31
3.4 Quantum non-linear optics: parametric down conversion . . . 33
3.4.1 Finding PDC temporal modes . . . 35
3.5 The quantum pulse gate . . . 36
3.5.1 QPG non-linear device realisation . . . 37
3.5.2 The mode selectivity . . . 38

II Design and application of Quantum non-linear devices **41**

4 Quantum networks: state of the art **43**
4.1 Quantum light sources . . . 44
4.1.1 Single emitters . . . 45
4.1.2 PDC sources . . . 45
4.2 Quantum memories . . . 46
4.3 Quantum information processing . . . 47
4.4 The challenges for realistic quantum devices . . . 48

5 QFC: design and characterization **51**
5.1 Study of inhomogeneities on QPG devices . . . 51
5.1.1 Revised LN fabrication process . . . 53
5.2 Improved QPG device . . . 54
5.2.1 Analysis of the waveguide inhomogeneities . . . 56
5.2.2 Temperature inhomogeneities . . . 59
5.3 QFC design . . . 61
5.3.1 Interfacing a quantum dot with a streak camera . . . 62
5.3.2 Design guidelines . . . 62

6 The QPG at work **65**
6.1 QPG experimental setup . . . 65
6.1.1 Spatial light modulators for spectral shaping . . . 67
6.2 Quantum metrology . . . 69
6.2.1 Fisher information and parameter estimation . . . 69
6.2.2 Quantum parameter estimation with the QPG . . . 71
6.2.3 Multiparameter estimation . . . 71
6.2.4 Coherence effects . . . 74
6.3 Randomized compressive tomography . . . 76
6.3.1 State description . . . 78
6.3.2 RCT method . . . 79

6.3.3 Experimental realization 80

7 Orchestrating high-dimensional PDC states **85**
7.1 Tailoring the JSA 85
7.1.1 Measuring the modal composition 87
7.2 Generation of high-dimensional maximally entangled states 87
7.2.1 JSI function measurements 89
7.2.2 $g^{(2)}$ measurements 90
7.2.3 Resolution limit 90

Conclusions **93**

Acknowledgements **95**

Bibliography **97**

Summary

A child of five could understand this.
Send someone to fetch a child of five.

Groucho Marx

In this thesis, we experimentally investigate the limits of state of the art integrated non-linear devices for photonic and quantum technologies and seek new applications for them.

First, following a thorough characterization of the impact of fabrication parameters on titanium in-diffused lithium niobate waveguides, we present an optimized quantum pulse gate device with a fourfold increase in length over previous efforts. Additionally, we detail a ccomputational method to identify and characterize waveguide inhomogeneities. Quantum frequency conversion is introduced as a frequency interface between quantum devices and we present design guidelines to interface quantum devices.

Next, the quantum pulse gate process is experimentally exploited in two different applications. We demonstrate multi-parameter estimation of the properties of a two-incoherent field mixture down to the quantum limit. Moreover, we demonstrate that the presence of coherence in such system does not hinder the technique. Finally, the quantum pulse gate is used to implement a novel compressive state tomography, in an order of magnitude less measurements than scan tomography methods.

To take advantage of high-dimensional quantum communication protocols and systems. a novel PDC source of high-dimensional maximally entangled bi-photon states is presented. The source relies on the dispersion engineering of a titanium tytanyl phosphate waveguide and the spectral shaping of the pump field.

Zusammenfassung

In dieser Arbeit loten wir die Grenzen moderner integrierter, nicht-linearer Bauteile für photonische und quantenoptische Technologien aus und suchen nach neuen Anwendungen.

Zuerst stellen wir, nach gründlicher Charakterisierung der Einflüsse der Fabrikationsparameter auf Titan-in-diffundierte Lithium-Niobat-Wellenleiter, ein optimiertes, vierfach längeres Quanten-Puls-Gate (QPG) vor. Zusätzlich beschreiben wir detailliert eine numerische Methode zur Identifizierung und Charakterisierung von Inhomogenitäten in Wellenleitern. Quanten-Frequenz-Konversion wird als eine Schnittstelle zwischen Quanten-Bauteilen eingeführt und Design-Richtlinien um sie zu verbinden werden präsentiert.

Als Nächstes wird das QPG in zwei Anwendungen genutzt. Wir demonstrieren eine Multi-Parameter Abschätzung der Eigenschaften einer Mischung zweier inkohärenter Felder bis an das Quanten-Limit. Darüber hinaus zeigen wir, dass die Gegenwart von Kohärenz in diesem System die Methode nicht behindert. Schließlich wird das QPG genutzt um eine neuartige, kompressive Zustandstomographie, mit einer Größenordnung weniger Messungen als bei scanbasierten Methoden, zu implementieren.

Um Vorteile hoch-dimensionaler Quantenkommunikationsprotokolle und -systeme auszunutzen, wird eine neue PDC-Quelle hoch-dimensionaler, maximal verschränkter Bi-Photonen vorgestellt. Diese Quelle beruht auf der Dispersionsmanipulation eines KTP Wellenleiters und dem spektralen Formen des Pump-Feldes.

Preface

Siempre harás más de lo que has hecho;
acuérdate, acuérdate.

José Antonio Labordeta Subías

This doctoral thesis is the result of the work carried out from 2017 to 2021 in the integrated quantum optics (IQO) group under the leadership of Prof. Dr. Christine Silberhorn. The task proposed for the work was to improve the performance of non-linear devices integrated in lithium niobate (LN) waveguides for quantum technologies and find new applications for the processes. Initially, the performance of LN waveguides under different fabrication parameters was studied to identify sources of error and asses them. As a result of the work, the fabrication process was improved and new samples were produced with improved performance. In particular, long quantum pulse gate (QPG) devices that had been suffering from fabrication limits were produced with enhanced benchmarks. The impact of fabrication inhomogeneities on the waveguides was studied with new computational methods to retrieve the profile of the inhomogeneities and their impact on the devices' performance. Moreover, the experimental conditions that also had a negative impact on the QPG, were also investigated.

The QPG is one of the central devices of this thesis. Besides improving its performance through an enhanced fabrication process and more controlled experimental conditions, we found new applications for its photon temporal mode projection operation. First, in a collaboration with the groups of Prof. Dr. Luis Sanchez-Soto, Prof. Dr. Jaroslav Řeháček and Prof. Dr. Zdeněk Hradil, we extended a previously demonstrated single-parameter quantum estimation scheme with the QPG to a multi-parameter scenario. We experimentally demonstrated the estimation of three different parameters from the incoherent mixture of two fields, beyond the classical resolution bound and saturating the quantum limit. Furthermore, we investigated the effect of the presence of coherence between the two fields and demonstrated that coherence does not have any negative repercussion on the method. We investigate possible ways to exploit it.

Finally, we implemented a novel quantum state tomography scheme in a collaboration with the groups of Prof. Dr. Luis Sanchez-Soto and Prof. Dr. Hyunseok Jeong, using the QPG. Exploiting the projective measurements implemented by the QPG, we reconstructed few-photon level states in the time-frequency domain with high fidelities and no a-priori information about the original states. This new method outperforms common scan tomography schemes by performing the same task while requiring an order of magnitude less measurements to fully reconstruct an state. It presents a promising perspective towards efficiently characterising quantum systems.

Additionally, the spectral properties of general quantum frequency conversion processes were studied in detail. The aim was to design the most efficient frequency conversion process to interface

different quantum devices working at different frequencies with the available resources. This design paradigm was put to the test with a sum frequency process to convert light from quantum dots in the infra-red to the visible in order to measure their temporal properties. Therefore, the process was designed to convert the light with the maxmium possible efficiency while maintaining the spectral properties of the original quantum dot emission. This process was succesfully tested experimentally in Dortmund in the group of Prof. Dr. Manfred Bayer with whom we collaborated for this project.

To complement the temporal mode operation of the QPG experiments, we investigated the generation of high-dimensional photon states. These states can be directly manipulated with the QPG and present advantages to many quantum communication protocols due to their higher information capacity and spectral correlations. By engineering a parametric down conversion source and designing a spectral shaping setup for pulses, we produced maximally entangled pairs of photons in up to six dimensions. This one of a kind photon source clears the path for many high dimensional quantum systems.

The discussions and results presented in this thesis are the conclusion of my own individual work. However, the work was carried out in the context of a research group and in collaboration with colleagues from different universities. Hence, many people has contributed to parts of the work.

First author publications

- J. Gil-Lopez, M. Santandrea, G. Roland, B. Brecht, and C. Silberhorn, *Improved non-linear devices for quantum applications*, New J. Phys. 23 063082 (2021).
- J. Gil-Lopez, Y. S. Teo, S. De, B. Brecht, H. Jeong, C. Silberhorn, and L. L. Sánchez-Soto, *Universal compressive tomography in the time-frequency domain*, Optica Vol. 8, Issue 10, pp. 1296-1305 (2021).

Author contributions

- V. Ansari, B. Brecht, J. Gil-Lopez, J. M. Donohue, J. Řeháček, Z. Hradil, L. L. Sánchez-Soto, and C. Silberhorn, *Achieving the Ultimate Quantum Timing Resolution*, PRX Quantum 2, 010301 (2021).
- S. De, J. Gil-Lopez, B. Brecht, C. Silberhorn, L. L. Sánchez-Soto, Z. Hradil, and J. Řeháček, *Effects of coherence on temporal resolution*, Phys. Rev. Research 3, 033082 (2021)

Introduction

> The most exciting phrase to hear in science, the one that heralds the most discoveries, is not "Eureka!" but "That's funny..."
>
> *Isaac Asimov*

In the last two decades we have seen the birth of the first quantum technologies. Devices such as quantum memories, logical gates or quantum protocols like quantum key distribution and Gaussian boson sampling, aim at surpassing classical performance and lead us into a new scientific revolution, a quantum era. The application of quantum devices into everyday life can impact many fields: medicine with the improved simulation of drugs and chemical compounds, energy production with more efficient devices and better and safer communication with entangled particles, to name a few.

Currently, many of these devices have been experimentally proven and there exists theoretical models for many applications. Moreover, companies around the world are already working on building quantum computers, highlighting their economic potential. However, we are still far from realistic final applications as most devices are actually full sized experimental setups occupying rooms and many don't reach their expected performance or a significant advantage over classical systems. A common bottleneck for both problems is the integration of the technologies into small footprint devices. Just like the computational era began with the integration of electronics into miniaturised circuitry, quantum technologies will rely on their miniaturisation to succeed.

One promising platform for the integration of the devices are photonic technologies. Photonic systems utilize the quantum properties of light, exploiting photons as the information carrier. Photons have the advantage of weakly interacting with the environment. Furthermore, being light fields, classical light guiding optics can be used to integrate photonic systems using waveguide structures in different materials and exploiting non-linear effects in these materials. However, the low number of photons typically involded in quantum systems presents a problem: the photonic devices must be highly efficient to ensure that photons are not lost. This implies a new challenge for the integration and application of quantum optical integrated platforms as the quality of the devices has higher requirements than classical applications.

The work in this thesis is carried out in this context, enhancing photonic integrated technologies to reach the requirements of final real world devices. In particular, the work carried out focuses on waveguide integrated non-linear effects for the generation of interesting photon states for quantum information science applications and the processing of quantum information.

In part I of the thesis, the theoretical background that back the experimental results is laid

down. Each chapter in this part starts with a brief review of the history of the field discussed in the chapter, highlighted in blue. The intention of the author is to emphasize the key role of interdisciplinary work and solid knowledge of the state of the art theories and technologies in the advance of science. This is fundamental for quantum technologies, due to the current wide variety of platforms and approaches in development, making these compatible and designing the devices with the big picture in mind allows us to benefit from prior works and design systems that can work together, exploiting the advantages of different technologies.

Chapter 1 discusses the basic characteristics of optical waveguides. These are the structures in which we integrate photonic devices. Next, in chapter 2, second order non-linear processes are reviewed. The origin of these effects, their nature and characteristics are discussed. We focus on the parameters that will allow us to design specific processes for quantum applications and their performance with the pulsed light fields later exploited in this thesis. The characteristics of the two non-linear materials used in the presented work, lithium niobate and potasium titanyl phosphate, are discussed as well. Finally, in part 3, the quantum mechanical principles exploited for information encoding and processing in photons are discussed. The temporal mode framework to encode information in the energy degree of freedom of photons is detailed. Furthermore, the theoretical foundation for the exploitation of non-linear processes for the generation and processing of temporal mode encoded photons is introduced. To that end, the processes of parametric down conversion (PDC) and the quantum pulse gate (QPG) are discussed.

In part II, we present the experimental results. In chapter 4, the state of the art of quantum devices is discussed to give a context to the experiments carried out in this thesis. In chapter 5, the limitations of current quantum frequency conversion processes in waveguides are studied and addressed. This leads to the fabrication and characterisation of a QPG device four times longer than any before that improves the performance in all the benchmarks studied. Additionally, a design paradigm for frequency conversion interfacing quantum dots with other devices is detailed.

Additionally, in chapter 6, the versatility of the QPG is exploited in two quantum schemes, i.e. parameter estimation and state tomography. First, the QPG is used to estimate three spectral parameters of two incoherent overlapping fields with resolution saturating the quantum limit and surpassing the classical bound. Next, the effects of the presence of coherence are studied in the parameter this estimation scenario. We experimentally demonstrate that coherence doesn't enhance or handicap the scheme and propose ways to exploit it to sort the information in the two fields. Finally, the QPG is used to introduce a groundbreaking quantum state tomography method to reconstruct quantum states. The randomized compressive tomography scheme reconstructs states with high fidelity while requiring an order of magnitude less measurements than typically used scan tomography methods. We experimentally demonstrate the RCT scheme by reconstructing photon states of different types.

To conclude, a novel PDC source of high-dimensional maximally entangled photons is introduced and experimentally demonstrated in chapter 7. The engineering of the properties of the non-linear process combined with the spectral shaping of the pump field allows one to generate two photon states with a controlled number of maximally entangled modes.

Part I

Theoretical framework

> Nothing in life is to be feared; it is only to be understood.
>
> *Marie Skłodowska-Curie*

The experimental results of this work are built upon a deep understanding of the physics underlying non-linear quantum devices and their language. First, in order to tame non-linear effects to the very particular needs of photons, the basics of non-linear processes must be well understood. Then, to understand these processes and use them to speak a quantum language, one needs a quantum alphabet. In this part, we will go from the basic description of non-linear processes to the characteristics that allows us to tailor them towards quantum applications. Next, we will learn how to communicate with them in the quantum world by building an alphabet with photonic temporal modes. Note that we will follow the mathematical calculations with just enough detail to obtain the results that support the experimental work carried out in the following parts. When proper, the reader will be directed to more detailed literature should they wish to dive deeper into the vast ocean of maths behind the presented work.

Chapter 1

Waveguides in a nutshell

The development of waveguides is a great example of how science, technology, and even economical interests influence the development of new discoveries. Electromagnetic phenomena bloomed into one of the most important field of physics after the work of Faraday and Maxwell at the end of the XIX century. One of the most important questions was the propagation of electromagnetic waves in the vacuum and different media. The only type of propagating wave recognized at first was the transverse electromagnetic field observed in conducting wires; that is the mode of a transverse plane wave with electric and magnetic fields perpendicular to the propagation axis. Therefore, that was taken as the paradigm to study the problem in general. With that mindset, Heaviside concluded in his study of electromagnetic waves that single line conductors (what we would call today a waveguide) were not possible without parallel conductors or a "return" to earth. Hollow tube waveguides were not possible [1] missing an inner conductor. These systems were thus considered to have the same behaviour as electricity.

However, in 1897, Lord Rayleigh came to study the problem with his broad experience of waves from sound theory, light waves and fluids. He solved Maxwell's equations under the boundary conditions of a small (centimeter scale) hollow cylindrical structure and found that waves could indeed be transmitted through such structures [2]. Furthermore, the electromagnetic waves propagated in well-defined sets of modes constrained by the properties of the structure. Finally, Rayleigh found that there was a cut-off frequency, defined again by the structure, at which waves with lower frequencies didn't propagate anymore in fully confined modes.

At this point, the study and experimental demonstration of waveguides would have quickly sprouted had it not been for the direction that the electromagnetic community had already adopted. The lack of high frequency electromagnetic sources needed for Rayleigh's structures and the huge interest and economical potential of radio waves (using low frequencies) for communication, displaced Rayleigh's findings out of the spotlight.

It took almost thirty more years and the independent (and secretive) efforts of George C. Southworth (with the very important contributions of at least one female mathematician Sallie P. Mead) and Wiltner L. Barrow to prove and experimentally demonstrate the propagation of electromagnetic waves in hollow tubes, that is, the first ever kind of waveguide. They both had to rediscover Rayleigh's findings on their own. It is fun to learn about this today, knowing the scientific and economic impact that waveguides, optical fibers in particular, have had in scientific development. We are, so to speak, thirty years behind our own discoveries.

In this chapter, we will lay down the basic working principles of waveguides. We will discuss the solution of Maxwell's equations in guiding structures, which lead to the definition of a guided mode (a.k.a. waveguide mode) and to the derivation of necessary conditions for the existence of a guided mode.

1.1 Waveguide field confinement and modes

The simplest form of waveguide is the dielectric slab. It consists of three dielectric material regions with different refractive indexes, the core of width d, embedded between the substrate and cladding regions, with lower refractive index, as depicted in figure 1.1. The regions extend infinitely in the xz plane.

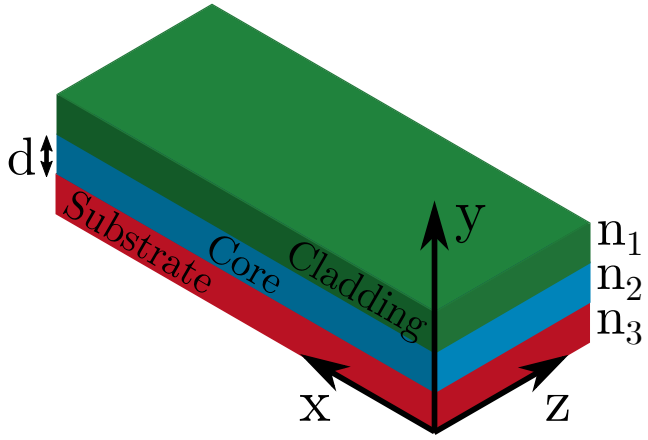

Figure 1.1: Slab waveguide on the reference axis. The three regions: core, substrate and cladding, are differentiated by colors. The refractive index n of each region is noted on the side.

It is useful to start with the description of the slab waveguide as it is one of the few guiding structures where an analytical solution can be found, and the results provide good approximations to more complex waveguide structures under the proper assumptions. One can use plane-wave optics to solve the propagation of light through a slab waveguide. Total internal reflection within the dielectric slab allows for the confinement of the field.

The light entering the core with a certain angle θ_2, as shown in figure 1.2, on the cladding (or substrate) will be reflected and diffracted the interface following Snell's law

$$n_2 \sin\theta_2 = n_\mathrm{i} \sin\theta_i, \tag{1.1.1}$$

where i= 1, 3.

For the field to be confined, it must be totally reflected with $\theta_i = 90°$. In that case, there is no diffracted light and we obtain the critical angle of interface i $\theta_{i,c}$:

$$\theta_{i,c} = \arcsin\left(\frac{n_i}{n_2}\right), \tag{1.1.2}$$

so that if $\theta_2 > \theta_{i,c}$, there is total internal reflection at both interfaces and the field is confined inside the waveguide when $n_2 > n_i$, this is illustrated in figure 1.2 with a ray optics description of the fields. However, the condition $\theta_2 > \theta_{i,c}$ is a necessary but not sufficient condition for guiding light into a dielectric slab. In fact, constructive interference among all the reflected waves inside the structure needs to occur, in order to maintain a lossless, propagation solution which we call a mode. When the correct self-consistency condition is imposed, one finds that propagation can occur only for a finite set of angles [3], each defining a so-called propagation mode.

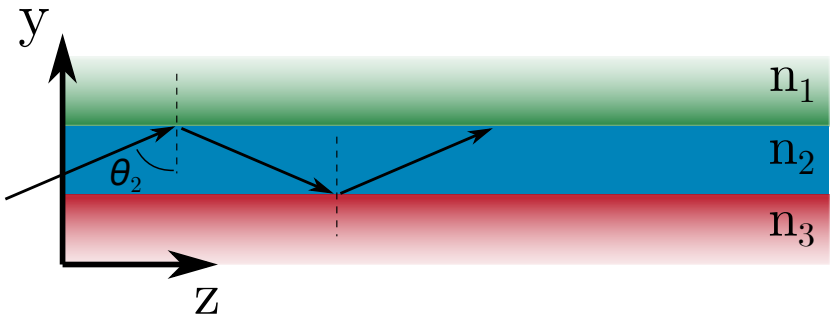

Figure 1.2: Representation of an optical ray confined inside the slab waveguide at an angle $\theta_2 > \theta_{\mathrm{i,\ C}}$

The approach described above works quite well for multi-mode waveguides, i.e. waveguides that support many modes of propagation. For single-mode waveguides, which are at the core of the experimental work of this thesis, this explanation is not sufficient. Therefore, the next section will outline the problem considering the full mathematical description, stemming from Maxwell's equations. This way we get a full understanding of the propagation of the fields and how the structure can modify the behaviour.

1.1.1 Guided modes in the asymmetric slab

Maxwell's equations can be written as

$$\nabla \times \mathbf{H} = \varepsilon_0 n^2 \frac{\partial \mathbf{E}}{\partial t} \tag{1.1.3}$$

$$\nabla \times \mathbf{E} = -\mu_0 \frac{\partial \mathbf{H}}{\partial t}, \tag{1.1.4}$$

with $\mathbf{H}$ and $\mathbb{E}$ the magnetic and electric vectors, and ε_0 and μ_0 the dielectric permivitty and magnetic permeability of vacuum. We will consider that the refractive index is constant in the propagation direction z and in y, $n = n(x)$.

It can be shown that Maxwell's equations lead to two distinct sets of guided modes for a slab waveguide. These mode are defined as transverse electric (TE) or transverse magnetic (TM), depending on whether the field has no electric or magnetic component along the propagation direction, respectively. This division is rigorous for 2D slab waveguides and is a good approximation for waveguides with dimensions greater than the wavelength of the guided light. This links directly with the polarization of the fields and which components $[E_x, E_y, E_z]$ and $[H_x, H_y, H_z]$ of the fields are present. We will study TE modes in detail as they are sufficient to discuss the key properties of waveguides for this thesis. TM modes can be obtained analogously.

TE modes

TE modes are usually recognized as horizontally polarized fields as waveguides usually sit on experimental setups on the xz plane as in figure 1.1, with components E_y, H_x and H_z. To solve equations 1.1.4 and 1.1.3, we consider solutions in the form of harmonic fields like

$$\mathbf{E_y}(z,t) = E_y e^{\mathrm{i}(\omega t - \beta z)}, \tag{1.1.5}$$

taking into account the translational symmetry of the waveguide along z. It describes the $\mathbf{E_y}$ component of the electric field travelling along the propagation direction z, β the z component of the propagation constant inside the waveguide and E_y the amplitude of the component.

From Maxwell's equations, with no variation in y, we obtain

$$-\mathrm{i}\beta\mathbf{H_x} - \left(\frac{\partial \mathbf{H_z}}{\partial x}\right) \mathrm{i}\omega\varepsilon_0 n^2 \mathbf{E_y} \tag{1.1.6a}$$

$$\mathrm{i}\beta\mathbf{E_y} = -\mathrm{i}\omega\mu_0\mathbf{H_x} \tag{1.1.6b}$$

$$\frac{\partial \mathbf{E_y}}{\partial x} = -\mathrm{i}\omega\mu_0\mathbf{H_z}. \tag{1.1.6c}$$

We have considered a weakly guiding waveguide such that $n(x)$ varies slowly over one optical wavelength. This is the case for waveguides where the refractive index change between regions is relatively small[1].

Substituting 1.1.6b and 1.1.6c into 1.1.6a, we obtain the reduced wave equation of E_y

$$\left(\frac{\partial^2 \mathbf{E_y}}{\partial x^2}\right) + (n^2k^2 - \beta^2)\mathbf{E_y} = 0, \tag{1.1.7}$$

with $k^2 = \omega^2\varepsilon_0\mu_0$. Solving 1.1.7 we can find the modes of $\mathbf{E_y}$ with different propagation constants $\beta_\mathrm{m} = \beta_\mathrm{m}(\omega)$, where m is the number of the mode. It is useful to introduce the effective refractive index n_eff now such that:

$$\boxed{\beta_m = n_{\mathrm{eff},m}k.} \tag{1.1.8}$$

The effective refractive index describes the "average" refractive index of the guided mode due to the confined nature of the propagated field [4].

Equation 1.1.7 can be considered separately for each region of the waveguide and one can apply the continuity condition of the fields to find $\mathbf{E_y}$ and β_m for each mode. We write the equations

$$\left(\frac{\partial^2 \mathbf{E_y}}{\partial x^2}\right) + (n_1^2k^2 - \beta^2)\mathbf{E_y} = 0, \qquad \text{for } x < d \tag{1.1.9a}$$

$$\left(\frac{\partial^2 \mathbf{E_y}}{\partial x^2}\right) + (n_2^2k^2 - \beta^2)\mathbf{E_y} = 0, \qquad \text{for } 0 < x < d \tag{1.1.9b}$$

$$\left(\frac{\partial^2 \mathbf{E_y}}{\partial x^2}\right) + (n_3^2k^2 - \beta^2)\mathbf{E_y} = 0, \qquad \text{for } x < 0. \tag{1.1.9c}$$

[1] This is the case for the structures investigated in this work

It is important to note the term $(n_i^2 k^2 - \beta^2)$ in equations 1.1.10. The nature of $\mathbf{E_y}$ is greatly influenced by this term. The solution of equations 1.1.10 is an oscillating field confined in the waveguide core and produces a guided mode only if $k_0 n_1 < \beta_m < k_0 n_3$. For $\beta > k_0 n_3$, the solutions diverge, and thus describes unphysical solutions (no guiding possible). If $\beta < k_0 n_1$, then the solution oscillates between the substrate/cladding. These solutions constitute a continuum of guided modes, with power "confined" outside the guiding region. Therefore, despite there being a solution to Maxwell's equations, they are usually regarded as leaky or lossy modes, since power is not confined in the region of interest. Therefore, not every mode is a guided mode and the values of β_m will determine the propagation properties of the waveguide.

Restricting ourselves to guided modes, the solutions of 1.1.10 are

$$\mathbf{E_y}(x) = E_1 e^{-\gamma_1 (x-d)}, \qquad \text{for } x < d \tag{1.1.10a}$$

$$\mathbf{E_y}(x) = E_2 \cos(\kappa_2 x - \phi), \qquad \text{for } 0 < x < d \tag{1.1.10b}$$

$$\mathbf{E_y}(x) = E_3 e^{-\gamma_3 x}, \qquad \text{for } x < 0, \tag{1.1.10c}$$

where $\gamma_1^2 = \beta_m^2 - k_0^2 n_1^2$, $\gamma_3^2 = \beta_m^2 - k_0^2 n_3^2$ and $\kappa_2^2 = k_0^2 n_2 - \beta_m^2$. Following the steps of Lord Rayleigh in his at-first-forgotten work, we introduce the boundary conditions now. Fields must be continuous in the waveguide region interfaces at $x = 0$ and $x = d$, this produces the following expression (after some rearranging)

$$\kappa_2 d - \phi - \varphi = \mathrm{m}\pi, \qquad \text{with } \tan\varphi = \frac{\gamma_1}{\kappa_2} \text{ and } \tan\phi = \frac{\gamma_3}{\kappa_2} \tag{1.1.11}$$

Equation 1.1.11 can be solved numerically and gives different values of β_m, for different integer m. However, the number of possible modes is finite (there exist a maximum m). This gives the total number of modes in a waveguide. The n_eff for each mode is defined as β_m/k, and it represents the effective index seen by light travelling in the structure in the specific guided mode. Finally, the cut-off waveguide width d_cutoff is defined by the value of d for which m> 1 and the waveguide is not single-mode anymore.

Chapter 2

Non-linear optics

In 2021, we celebrate the 61st anniversary of the invention of the laser by Maiman in 1960 [5]. The laser has since been squeezed (figuratively and literally) to the point that we cannot imagine optics without it. It should not come as a surprise then that we are also celebrating the 60th anniversary of what is considered the first non-linear optics experiment: the discovery of second-harmonic generation by Franken et al. in 1961 [6], only one year after Maiman's invention.

The invention of the laser itself relied on magnetic non-linearity [7] and some authors [8] might point out the fluorescence saturation discovered by Lewis in 1941 [9] or even the non-linear effects discovered by Kerr on the second half of the XIX century [10, 11] as the first non-linear optical effects. However, the generation of a second-harmonic by Franken, i.e. the generation of a field at twice the frequency of the original field, was the first all-optical non-linear effect observed experimentally. The discovery of two photon absorption by Kaiserr and Garret [12] followed very closely the same year; the process had been predicted by Maria Goeppert-Mayer, the third woman to earn the physics Nobel prize, in her PhD. Both discoveries were only achievable thanks to the high intensity fields and the coherence provided by the laser invented one year before.

In this chapter, we will go from the physical origin of non-linear processes to the equations describing the generated fields. The properties of waveguides discussed in the previous chapter will be included in the formalism to describe the non-linear integrated devices studied in this thesis.

2.1 The non-linear polarization

The phenomena discovered by Franken, Kaisser, Garret and their associates (and all the new effects that were discovered thereafter) are the results of the changes of the properties of a material induced by the presence of light. Changes that depend non-linearly on the light fields present in the medium.

In general, the light fields modify the dipole moment per unit volume, the polarization $P(t)$ of the material. First, this was used to explain linear effects with the polarization given by $P(t) = \chi E(t)$, where $\chi^{(1)}$ is the linear susceptibility. The solution of Maxwell's equations in the medium include the polarization term which is the source of the effects. By including higher order terms of $P(t)$ through a Taylor expansion

$$P(t) = \chi^{(1)}E(t) + \chi^{(2)}E^2(t) + \chi^{(3)}E^3(t) + ..., \tag{2.1.1}$$

where $\chi^{(2)}$ and $\chi^{(3)}$ are the second- and third-order non-linear susceptibilities, we find the non-linear polarization terms. This is how optical linear and non-linear effects measured were first explained and described by Bloemberg, Pershan and others in 1962 [13, 14]. We are going to restrict our description to the second-order processes used in this work, described by the second term in equation 2.1.1,

$$P^{(2)}(t) = \chi^{(2)} E^2(t). \tag{2.1.2}$$

For the time being, we will restrain ourselves from fully deriving the expressions for the generated fields. We will start by unearthing all the non-linear processes that arise from the polarization.

The second order non-linear phenomena arise from the interaction of the optical field $E^2(t)$ and the susceptibility $\chi^{(2)}$. Let's imagine that the incident field $E(t)$ has two frequency components

$$E(t) = E_1 \mathrm{e}^{-\mathrm{i}\omega_1 t} + E_2 \mathrm{e}^{-\mathrm{i}\omega_2 t} + c.c., \tag{2.1.3}$$

which, substituted into equation 2.1.2 results in

$$\begin{aligned} P^{(2)}(t) = \chi^{(2)} [& E_1^2 \mathrm{e}^{-\mathrm{i}2\omega_1 t} + E_2^2 \mathrm{e}^{-\mathrm{i}2\omega_2 t} + && (2.1.4)\\ & 2E_1 E_2 \mathrm{e}^{-(\omega_1+\omega_2)t} + && (2.1.5)\\ & 2E_1 E_2^* \mathrm{e}^{-\mathrm{i}(\omega_1-\omega_2)t} + c.c.] + && (2.1.6)\\ & 2\chi^{(2)} [E_1 E_1^* + E_2 E_2^*], && (2.1.7) \end{aligned}$$

where all the different (second-order) non-linear processes can arise:

1. Second-harmonic generation (SHG) can take place doubling the frequency of one of the incident components.
2. Sum-frequency generation (SFG) when the original frequency components are summed.
3. Difference-frequency generation (DFG) when they are subtracted.
4. Optical rectification (OR) which is not the source of any propagating electromagnetic field (notice the absence of a frequency component) and generates a static electric field in the medium.

These processes are known as three-wave mixing processes as they involve three frequency components.

The first non-linear experiments that we reviewed earlier were performed in bulk materials. In 1971, ten years after these first non-linear process demonstrations, D. B. Anderson and J. T. Boyd used a GaAs planar waveguide [15]. Soon after, the advantages of waveguides became clear: field confinement and longer interaction lengths leading to higher efficiencies, integration potential and stability among others. As early as in 1988, Stegman and Stolen discussed and investigated the extent of the advantages of waveguided non-linear processes in several materials [16].

The non-linear susceptibility is a property of the material that defines the non-linear polarization. To understand how different materials produce non-linear interactions, the description of $\chi^{(2)}$ is given in the next section. Then, in section 2.2 and onward, we are going to obtain the expressions describing the generated fields of second-order non-linear processes in waveguides, with a focus on

SFG. We will first derive the solutions for monochromatic fields and then discuss how to extend the results to pulsed fields. The use of pulses and their spectral properties will be a key to the experimental results of this work. We will discuss them in section 2.3.

2.1.1 Non-linear polarization density

The non-linear polarization of a material is the source of the non-linear processes. The susceptibility $\chi^{(2)}$ couples the three interacting fields and can be described through non-linear coefficients d_{il} when the processes are far away from the resonant frequencies of $\chi^{(2)}$ and under Kleinman's symmetry conditions [8]. In this case, the non-linear polarization density can be related to the incident field polarization with

$$\begin{pmatrix} P_x(\omega_3) \\ P_y(\omega_3) \\ P_z(\omega_3) \end{pmatrix} = M\varepsilon_0 \begin{pmatrix} d_{11} & d_{12} & d_{13} & d_{14} & d_{15} & d_{16} \\ d_{21} & d_{22} & d_{23} & d_{24} & d_{25} & d_{26} \\ d_{31} & d_{32} & d_{33} & d_{34} & d_{35} & d_{36} \end{pmatrix} \begin{pmatrix} E_x(\omega_1)E_x(\omega_2) \\ E_y(\omega_1)E_y(\omega_2) \\ E_z(\omega_1)E_z(\omega_2) \\ E_y(\omega_1)E_z(\omega_2) + E_z(\omega_1)E_y(\omega_2) \\ E_x(\omega_1)E_z(\omega_2) + E_z(\omega_1)E_x(\omega_2) \\ E_x(\omega_1)E_y(\omega_2) + E_y(\omega_1)E_x(\omega_2) \end{pmatrix}. \tag{2.1.8}$$

From equation 2.1.8 it is straigthforward to classify the different types of second order non-linear processes depending on the polarization of the fields and the corresponding non-linear coefficient:

$$\begin{pmatrix} \overbrace{d_{11} & d_{12} & d_{13}}^{\text{Type 0/I}} & \overbrace{d_{14} & d_{15} & d_{16}}^{\text{Type II}} \\ d_{21} & d_{22} & d_{23} & d_{24} & d_{25} & d_{26} \\ d_{31} & d_{32} & d_{33} & d_{34} & d_{35} & d_{36} \end{pmatrix}, \tag{2.1.9}$$

with d_{11}, d_{22} and d_{33} the type 0 coefficients. If we take SFG processes, then:

- **Type 0**: the polarization of the three fields is the same.
- **Type I**: the polarization of the generated field E_3 is different from that of the incident fields E_1 and E_2.
- **Type II**: the two incident fields have different polarization. The generated field polarization depends upon phase-matching conditions.

The non-linear coefficients of a crystal are defined by its structural symmetries[1], limiting which processes are possible.

2.2 Non-linear coupled-wave equations in waveguides

We are ready now to derive the wave equation from Maxwell's equations in the non-linear material. We will start with a planar wave description and then modify it for waveguides. The displacement field **D** contains the material non-linear polarization P_{NL},

[1] Crystals can be classified in crystallographic classes depending on their symmetries [17]

$$\mathbf{D} = \varepsilon_0 \varepsilon_r E + P_{\mathrm{NL}}. \tag{2.2.1}$$

With this, we obtain the wave equation

$$\nabla \times \nabla \times E_n + \frac{n_n^2}{c^2}\frac{\partial^2}{\partial t^2}E_n = -\frac{1}{c^2}\frac{\partial^2 P_n}{\partial t^2}, \tag{2.2.2}$$

where the subindexes n denote the three interacting fields in the medium ($n = 1, 2, 3$) and we have neglected energy loss. Note the subindex under the refractive index n, this refers to the effective refractive index of the fields as they propagate through the waveguide. We introduce now a common naming convention for the fields names as described in figure 2.1: pump, signal and idler fields.

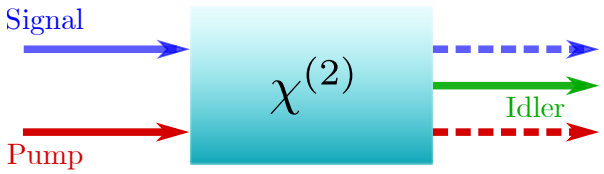

Figure 2.1: Sketch and nomenclature of the fields for classical $\chi^{(2)}$ three-wave mixing processes. This sketch represents SFG and DFG processes, for SHG the signal is the same field as the pump. The dashed line represents the unconverted/undepleted throughput fields through the medium.

With our continuous-wave (CW) monochromatic fields written as

$$E_n = A_n \mathrm{e}^{i(\beta_n z - \omega_n t)}, \tag{2.2.3}$$

where β_n is the propagation constant of the field in the waveguide, z is the propagation axis and $A_n = A_n(z)$ is the amplitude of the field. The non-linear polarization is then

$$P_n = M\varepsilon_0 d A_i A_j \mathrm{e}^{i(\beta_i \pm \beta_j)z}, \tag{2.2.4}$$
$$\text{with } n, i, j \in [1, 2, 3] \text{ and } n \neq i \neq j.$$

with M a multiplicity factor with value 1 for type 0/I SHG and 2 in all other cases, and d the non-linear coefficient for the process under study. The sign between the βs depends on the process as well as the frequencies (for example, $\beta_3 = \beta_1 + \beta_2$ for SFG).

Substituting the three fields 2.2.3 and the polarization into equation 2.1.1, we obtain the coupled-wave equations of the field amplitudes

$$\frac{dA_1}{dz} = -i\sqrt{\frac{8\pi^2 d^2 \omega_1^2}{n_1 n_2 n_3 c^3 \varepsilon_0}}\theta A_2 A_3 \mathrm{e}^{-i\Delta\beta z} \tag{2.2.5a}$$

$$\frac{dA_2}{dz} = -i\sqrt{\frac{8\pi^2 d^2 \omega_2^2}{n_1 n_2 n_3 c^3 \varepsilon_0}}\theta A_1 A_3 \mathrm{e}^{-i\Delta\beta z} \tag{2.2.5b}$$

$$\frac{dA_3}{dz} = -i\sqrt{\frac{8\pi^2 d^2 \omega_3^2}{n_1 n_2 n_3 c^3 \varepsilon_0}}\theta A_1 A_2 \mathrm{e}^{i\Delta\beta z}, \tag{2.2.5c}$$

with $\Delta\beta = \beta_1 + \beta_2 - \beta_3$ the momentum mismatch between the fields and θ the field overlap in the axes orthogonal to the propagation direction z,

$$\theta = \int dxdy E_1(x,y) E_2(x,y) E_3^*(x,y) d(x,y). \tag{2.2.6}$$

These are the coupled-wave equations that describe the three fields propagating through the non-linear medium. The amplitudes of the three fields are coupled and the generated field is defined by this coupling with the input fields.

This is the perfect time to raise a question: from all the second order processes we learnt may arise from the polarization, which one takes place? All of them at the same time? We can answer this by carefully looking at both sides of the wave equation 2.2.2 for an SFG process. For the generated field $n = 3$, on the left-hand side we have an electric field at frequency ω_3 propagating with momentum β_3. On the right-hand side, the polarization P_3 oscillates at frequency $\omega_1 + \omega_2$ and propagates with $\beta_1 + \beta_2$. The frequencies must fulfill energy conservation for the process to be physically feasible in the first place so that $\omega_3 = \omega_1 + \omega_2$. Then, the efficiency of the process depends on the interference between the generated wave at ω_3 and the polarization. Perfect interference occurs when the two propagate with the same momentum, i.e. $\beta_3 = \beta_1 + \beta_2$. This is known as the phase-matching condition and a process is said to be phase-matched when $\Delta\beta = 0$. At phase-matching, the non-linear process is most efficient. When the equality is not satisfied, the two waves propagate at different speeds, fall out of phase and $\Delta\beta \neq 0$. In this case, the process efficiency decreases from the maximum.

From our earlier definition of $\beta = nk_0$, we can susbsitute the wavenumber $k_0 = \omega/c$ to write the phase-mismatch of an SFG process as

$$\Delta\beta(\omega_1, \omega_2, \omega_3) = \left(\frac{n_1(\omega_1)\omega_1}{c} + \frac{n_2(\omega_2)\omega_2}{c} - \frac{n_3(\omega_3)\omega_3}{c} \right). \tag{2.2.7}$$

This expression highlights the main role that the frequencies and the effective refractive indexes of the fields modes in the waveguide play to restrict the non-linear processes available. A similar expression is written for each kind of second-order non-linear process by carefully changing the signs to follow energy and momentum conservation.

2.2.1 Quasi-phase-matching and periodic poling

The refractive index and frequency dependency of the phase-mismatch severely constrains what processes are possible in a material or structure. With a few exceptions, the most straightforward way of getting a phase-matched process is by exploiting birefringent materials. This is known as birefringent phase-matching and exploits the difference in refractive indexes of the crystallographic axes of the material to phase-match different fields. However, birefringent phase-matching is still very constraining and allows only the processes permitted by the materials own refractive index combinations.

A higher degree of tunability of the phase-matched frequencies can be achieved by a careful study of the propagation of the three fields in the medium, in the absence of phase matching. As we discussed in section 2.2.2, frequency components at perfect phase-matching $\Delta\beta = 0$ always add coherently and out-of-phase components will dephase continuously. Since the excitation polarization at P_3 propagates with momentum $(\beta_1 + \beta_2)$, while the generated field at ω_3 propagates at β_3, every $\Delta\beta L = \pi$ the two waves (P_3 and E_3) have opposite phase. Therefore, they go repeatedly in and

out of phase leading to an oscillation between constructive and destructive interference. Hence, no signal is effectively generated at ω_3[8].

On the other hand, if we invert the sign of the excitation wave with the same periodicity, i.e. if we re-phase P_3 and E_3 at every $L = \pi/\Delta\beta$, then we can obtain constructive interference and generate field at ω_3. This is the mechanism behind quasi-phase-matching. This was identified as early as in 1962 by Armstrong et al. [13]. By inverting the orientation of the nonlinear susceptibility χ_2 with period Λ, one can modify the phase matching condition such that the allowed process satisfies the condition $\Delta\beta = 2\pi/\Lambda$. The phase-mismatch term is then, assuming an SFG process:

$$\Delta\beta = \left(\beta_1 + \beta_2 - \beta_3 \pm \frac{2\pi}{\Lambda}\right), \tag{2.2.8}$$

with the term $1/\Lambda$ corresponding to the added phase of the periodic change with period Λ. Armstrong proposed switching between different materials at each period to compensate for the dephasing.

For ferroelectric materials, a more elegant approach is possible. Domain inversion through the application of high-voltages allows one to periodically switch the spontaneous polarization of a non-linear medium, inverting the crystal orientation and $\chi^{(2)}$. This provides a method to modulate the phase-matching with the desired period Λ and design quasi-phase-matched processes with equation 2.2.8. This was first applied to lithium niobate by Yamada et al. in 1998 [18].

Quasi-phase-matching is another illustration of how the detailed study of a physical process (in this case the out-of-phase solutions of the non-linear polarization by Armstrong) and the results in experimental applications (limited frequencies for non-linear processes) can lead to new technologies. An effect that was initially considered a limitation, was the basis for the design of tailored non-linear processes.

2.2.2 Phase-matching function

The amplitude of the generated field depends on the properties of the material and the interacting fields. Assuming that the input fields A_1 and A_2 are not depleted through the process, we integrate equation 2.2.5c over the interaction length L to obtain the amplitude of the generated field A_3:

$$A_3(\omega_1, \omega_2, \omega_3, L) = \frac{8\pi^2 d^2 \omega_3^2}{n_1 n_2 n_3 c^3 \varepsilon_0} \int_0^L \mathrm{e}^{i\Delta\beta z} dz =$$

$$\boxed{A_3(\omega_1, \omega_2, \omega_3, L) = \frac{8\pi^2 d^2 \omega_3^2}{n_1 n_2 n_3 c^3 \varepsilon_0} \underbrace{L \,\mathrm{sinc}\left(\frac{\Delta\beta L}{2}\right) \mathrm{e}^{i\frac{\Delta\beta L}{2}}}_{\text{PM function}},} \tag{2.2.9}$$

where the underlined part is also known as the phase-matching function (PM) φ of the process.

The PM function contains information about the momentum conservation of the non-linear process and waveguide propagation properties for the fields. For each process, it represents the amplitude of the involved frequencies as represented in figure 2.2a). Energy conservation is then enforced by the CW pump with $\omega_{\text{pump}} = \omega_{\text{output}} - \omega_{\text{signal}}$. The CW pump slices the PM function and produces a 1D spectrum of the amplitude of the generated field at different frequencies like in figure 2.2b). Finally, the length of the device L defines the bandwidth of the amplitude which narrows with increasing length. The length also impacts the final conversion efficiency as discussed in the next section.

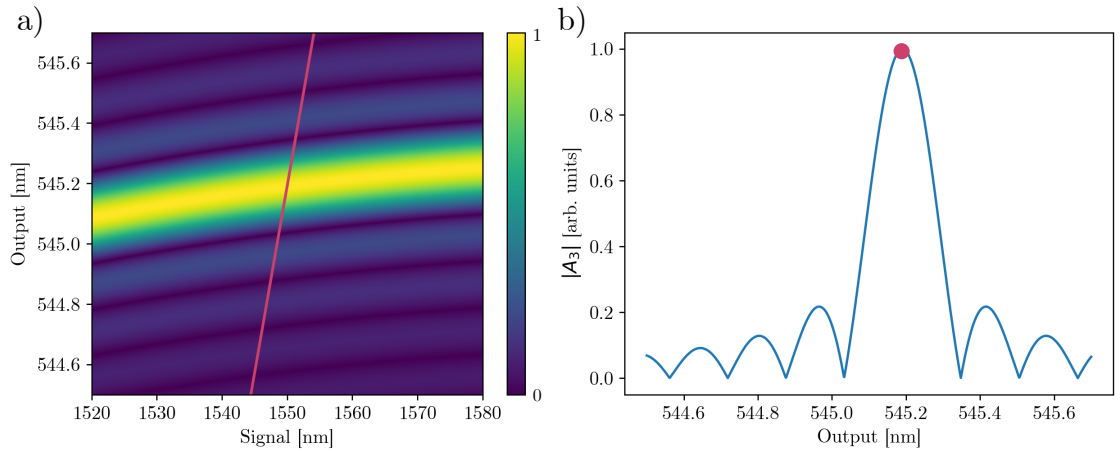

Figure 2.2: a) Example of the PM function of an SFG process in a 2mm long lithium niobate slab waveguide with a periodic poling of $\Lambda = 4.2\mu$m at a 100°C. The absolute value of the amplitude is plotted. The red line shows the 841nm CW pump. b) Absolute value of the amplitude of the phase-matched process at different output wavelengths for the CW pump in a). The dot shows the perfect phase-matched process 841+1550→545.2nm where the amplitude of the generated field is maximum due to $\Delta\beta = 0$ for the chosen wavelength combination.

2.2.3 Evolution and efficiency of the generated field

We have solved the equations of the interaction to obtain the PM function. To obtain the intensity of the generated field at any point z through the medium we can look at the process at perfect phase-matching $\Delta\beta = 0$ and under the no pump depletion approximation. The pump (E_2) is then constant and that there is no generated field at the beginning of the interaction $E_3(z = 0) = 0$.

Under these conditions, $\frac{dA_2}{dz} = 0$ and we are left with equations 2.2.5a and 2.2.5c. It's useful here to define the normalized conversion efficiency

$$\boxed{\eta_{\text{norm}} = \frac{8\pi^2\omega_1^2\omega_3^2 d^2|\theta|^2}{n_1 n_2 n_3 c^3},} \tag{2.2.10}$$

with units $\text{W}^{-1}\text{cm}^{-2}$. It describes the efficiency of the process, normalized per unit pump power and sample length. The normalized efficiency depends on the effective non-linear coefficient for the process considered, the spatial overlap, the effective refractive indices and frequencies of the interacting fields. Therefore, it is a very useful quantity to compare the conversion efficiency of processes under the same experimental conditions.

When integrating the system with equations 2.2.5a and 2.2.5c in z at perfect phase-matching $\Delta\beta = 0$, we obtain the spatial dependence of the fields amplitude:

$$\begin{cases} A_1(z) = A_1(0)\cos\left(\sqrt{\eta_{\text{norm}} I_2}\, z\right) \\ A_3(z) = -\text{i}A_1(0)\sqrt{\frac{\omega_3}{\omega_1}}\sin\left(\sqrt{\eta_{\text{norm}} I_2}\, z\right), \end{cases} \tag{2.2.11}$$

with $A_n(0)$ the amplitudes at $z = 0$. The evolution of the generated field intensity, $I_3(z) = |A_3(z)|^2$, is given by

$$\boxed{I_3(z) = I_1(0)\frac{\omega_3}{\omega_1}\sin^2\left(\sqrt{\eta_{\text{norm}} I_2} z\right).} \tag{2.2.12}$$

2.3 Pulsed non-linear processes

At this point we move away from the monochromatic description of the fields to the description of these processes using pulsed light. To include pulsed fields in the non-linear process description, we have to account for dispersion in the waveguides and what role it plays in the processes [19].

Pulses are characterised by their spectral envelope $f(\omega)$ at a central frequency ω_0, an example is given in figure 2.3. Every frequency component of the pulse contributes to the phase-matching, leading to parts of the pulse being phase-matched and the rest contributing to out-of-phase components. The generated field is now a new pulse, given by $\Delta\beta(\Omega)$ as depicted in figure 2.4.

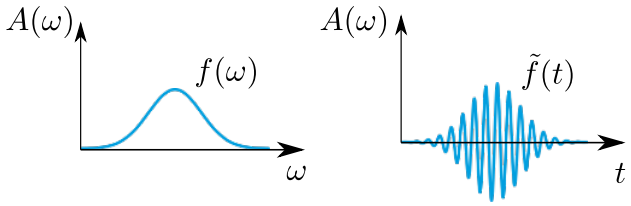

Figure 2.3: Example of a pulse spectral envelope in frequency and its complementary temporal distribution in time, with $\tilde{f}(t)$ the Fourier transform of $f(\omega)$.

Due to the materials' dispersion, pulses of different central frequencies will travel at different group velocities. If we expand $\Delta\beta$ in its Taylor series:

$$\Delta\beta(\omega_1, \omega_3) = \Delta\beta + \frac{d\Delta\beta(\omega_1, \omega_3)}{d(\omega_1)}\Delta\omega_1 + \frac{d\Delta\beta(\omega_1, \omega_3)}{d(\omega_3)}\Delta\omega_3 \ldots, \tag{2.3.1}$$

the first derivatives in ω_1 and ω_3

$$\frac{\partial\Delta\beta}{\partial\omega_1} = \left(\frac{\partial\beta_3}{\partial\omega_1} - \frac{\partial\beta_2}{\partial\omega_1} - \frac{\partial\beta_1}{\partial\omega_1}\right)\Delta\omega_1 = \left(\frac{1}{v_{g,2}} - \frac{1}{v_{g,1}}\right)\Delta\omega_1 \tag{2.3.2}$$

$$\frac{\partial\Delta\beta}{\partial\omega_3} = \left(\frac{\partial\beta_3}{\partial\omega_3} - \frac{\partial\beta_2}{\partial\omega_3} - \frac{\partial\beta_1}{\partial\omega_3}\right)\Delta\omega_3 = \left(\frac{1}{v_{g,3}} - \frac{1}{v_{g,2}}\right)\Delta\omega_3, \tag{2.3.3}$$

include the group velocities of the fields. Therefore, the slope of the PM function at perfect phase-matching

$$\tan\left(\frac{\Delta\omega_1}{\Delta\omega_3}\right) = \frac{v_{g,2}^{-1} - v_{g,1}^{-1}}{v_{g,2}^{-1} - v_{g,3}^{-1}}, \tag{2.3.4}$$

depends on the group velocities of the three fields. With the relation between the group velocities of the fields, different important group velocity matching (GVM) conditions can be defined: pump

and signal GVM allows one to match the interaction length to the waveguide length for maximum conversion efficiency and produces an horizontal PM function, symmetric GVM with the signal and output/idler at the same distance between the pump produces a 45° PM function an easily separable output and signal fields in frequency. This relations will be better understood later, when we look at the the group velocities of different wavelengths in figures 2.5 and 2.7 for two different materials.

2.3.1 Efficiency of pulsed processes

The equations describing the field evolution in 2.2.5 carry the temporal term from the wave equation that includes the group velocities. This renders the calculation of the field amplitudes very hard to obtain through integration. Therefore, an analytic expression for the efficiency of the field at phase-matching is not available.

The main difficulty lies in the pulses travelling at different speeds due to dispersion through the waveguide in the non-linear material. This changes the interaction length as pulses move away from each other. It can be shown that, for processes in which the input fields are group velocity matched, the coupled-wave equations reduce to those studied for monochromatic fields [20].

Experimentally, the conversion efficiency of a pulsed process can be measured through the converted to input power ratio, under the undepleted pump approximation. We can then describe the efficiency with a similar expression to equations 2.2.11

$$\eta_{\text{Pulsed}} = \frac{P_{converted}}{P_{input}} = \sin^2 \sqrt{\eta_{\text{norm}} P_p} L_{\text{int}}, \tag{2.3.5}$$

where P_p is the integrated optical power of the pump and L_{int} the interaction length that is now defined by the input pulses walk-off through the medium[2]. We are using the monochromatic expression to derive, empirically from experimental data, a quantitative expression to compare different processes. Although it is not derived from the coupled wave equations, the behaviour of the pulses cannot stray too far from this expression at low pump powers. By including the interaction length, we take into account the length at which the pulses interact while they surpass each other at different group velocities and the optical power of the pump accounts for its energy. With this expression, one can obtain an η_{norm} for a non-linear process and compare its performance with other processes under the same experimental conditions.

2.3.2 The transfer function

The amplitude of the generated field depends now on the envelopes of the pulses and the PM function is not enough to describe the full process. Previously, we obtained the amplitudes of the generated frequencies by enforcing energy conservation with the pump "slicing" the phase-matching function. The situation is a bit different for pulses, as now the energy conservation must be ensured by every frequency component of the envelop of the pulses. For that reason, we introduce the transfer function (TF)

$$\boxed{\text{TF} = \varphi(\omega_1, \omega_2, L)\alpha(\omega_1 + \omega_2),} \tag{2.3.6}$$

[2] In the case of processes with a single input field, L_{int} is the length of the device as the only interaction is between the input pulse and the medium and there is no walk-off.

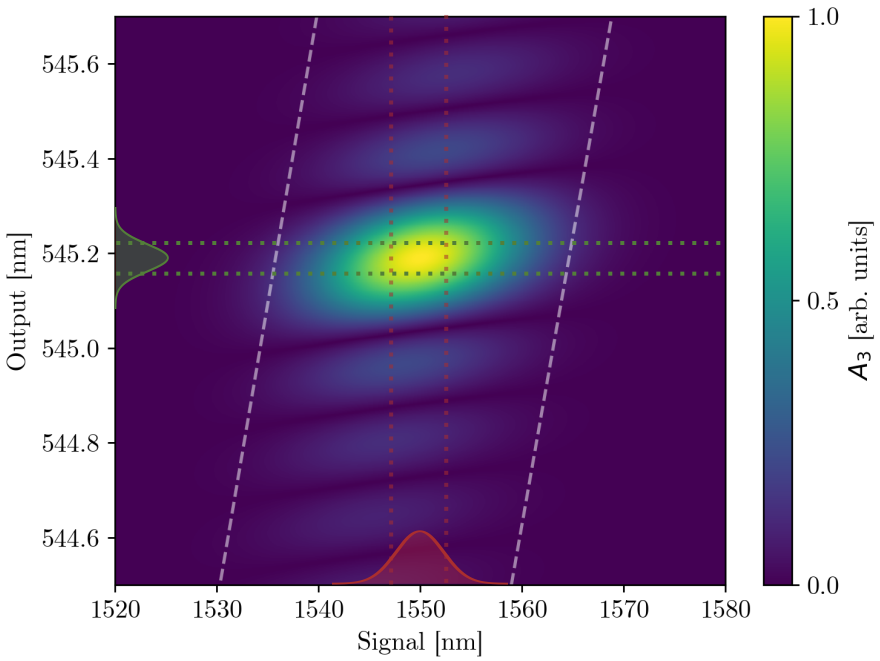

Figure 2.4: JSA resulting from applying a pulsed pump to the PM function of the SFG process discussed in figure 2.2 a). The pump full width at half maximum (FWHM) is indicated by the dashed white lines. A pulsed signal input generates a new pulsed output from all the frequencies of its envelope allowed by the JSA function. The input and output pulses FWHM are indicated in dotted lines, with red the input and green the output.

where φ is the phase-matching function of the process and $\alpha(\omega_1 + \omega_2)$ is the spectral envelope of the pump. With this we obtain a 2D picture of the spectrum of the process. In the case of SFG, it is useful to represent the transfer function of the process with the signal and output frequencies as variables. Then, the TF maps input spectra to output.

The TF includes important characteristics and properties of a pulsed process. The implications of the TF will be discussed in detail for the studied processes in the next chapter.

2.4 Non-linear waveguide platforms

There are many materials in which waveguiding structures can be produced. As we have learnt, the confined modes depend on the materials used, their refractive indexes and the structure built. One must not only consider the guiding properties of a certain waveguide but which other characteristics of the materials one wants to exploit for the application: the transparency range, dispersion, electro-optic effects and optical non-linearity among others. Due to their unique non-linear properties, in this thesis we study lithium niobate and potassium titanyl phosphate in detail. We will focus only

on the processes arising from the second order non-linear susceptibility studied in previous sections.

2.4.1 Lithium niobate

Lithium niobate (LN) is a dielectric material widely used in optical telecommunication networks thanks to its wide transparency and prominent acousto-optical, electro-optical and nonlinear optical properties. It is an artificial crystal, first fabricated by Zachariasen in 1928 [21].

Due to its crystalline structure, LN is a negative uniaxial birefringent material with ordinary and extraordinary optical axes parallel to the crystallographic c-axis. The extraordinary and ordinary refractive indexes can be obtained through Sellmeier equations (which include the effect of temperature) [22, 23].

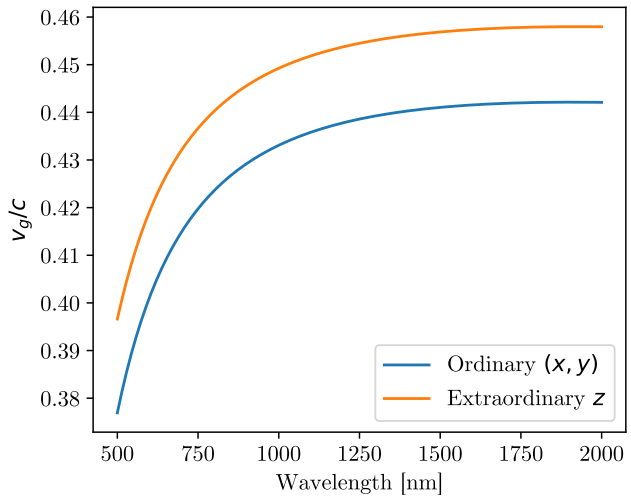

Figure 2.5: Normalised group velocities in LN for both crystallographic axes.

The normalised group velocities v_g/c, with c the speed of light, are shown in figure 2.5 for both axes. The uniaxal birefringence produces interesting behaviour for three-wave mixing processes. It is for example possible to produce group velocity matched type II SFG with the signal and pump fields in opposite polarizations.

LN lacks inversion symmetry, granting a non-zero $\chi^{(2)}$ and thus second order non-linear properties. Its non-linear coefficients are:

$$\begin{pmatrix} 0 & 0 & 0 & 0 & d_{31} & -d_{22} \\ -d_{22} & d_{22} & 0 & d_{31} & 0 & 0 \\ d_{31} & d_{31} & d_{33} & 0 & 0 & 0 \end{pmatrix},$$

with $d_{33} = 27.2 \pm 2.7$pm/V, $d_{31} = 4.35 \pm 0.44$pm/V and $d_{22} = 2.1 \pm 0.21$pm/V [24].

One major drawback of LN is its low photorefractive damage threshold. Photorefraction causes the refractive index of the material to change under strong incident electric fields. Due to the dependence on the refractive index of guiding structures and non-linear processes, this can severely

impact their performance. A possible solution, utilized in the experimental works presented in part II, is to operate at temperatures higher than 170 degrees Celsius [25].

2.4.2 Titanium diffused LN waveguides

One of the main objects of study of this thesis is the QPG, an SFG device engineered into Z-cut titanium diffused LN waveguides (Ti:LN). These structures are channel waveguides fabricated by diffusing titanium into LN, which increases the refractive index in the region, allowing confined modes to propagate.

The waveguide fabrication follows this procedure, illustrated in figure 2.6:

1. A titanium film of thickness τ is evaporated onto the surface of a 0.5mm thick LN crystal. A photoresist layer is then deposited on top of the titanium layer.

2. Using a photomask and standard photolitographic techniques illuminating with an ultraviolet lamp, photoresist stripes of width w are patterned on the titanium layer.

3. Exposed titanium is removed with chemical etching.

4. The remaining photomask is removed, resulting in titanium stripes of width w and thickness τ on top of the LN.

5. The sample is then introduced into an oven where the diffusion process takes place.

The temperature T of the diffusion process, its duration Δt and the titanium thickness τ and width w, define the resulting concentration profile of the titanium in the LN. The concentration profile can be calculated following Strake et al. [26]. The knowledge of the concentration profile and how it modifies the local refractive index is feed back into a numerical solver that calculates the effective refractive index of the guided modes of the structure.

2.4.3 Potassium titanyl phosphate

Potassium titanyl phosphate (KTP) is another important non-centrosymmetric non-linear material. It was fabricated for the first time in 1890 by Ouvrad and Troost [27]. It also has a wide transparency range in the visible and telecommunication wavelengths and, unlike LN, a high damage threshold (low photorefraction) and its dispersion properties do not change much with temperature. These last properties make KTP very useful to implement processes at room temperature.

KTP is a biaxial birefringent material with different refractive indices in x, y and z axes. A Sellmeier equation exists for all three of them [28]. These dispersion relations are key for the design of interesting processes in KTP. They allow for symmetric and asymmetric group velocity matching, with the pump on the faster axes, generating a separable bi-photon state at telecom wavelength [29]. The group velocities are shown in figure 2.7.

KTP has lower non-linear coefficients than LN, but the aforementioned characteristics make up for the differences as some interesting processes are not available in LN. The non-linear coefficients at 532nm and 1064nm are [30, 31]:

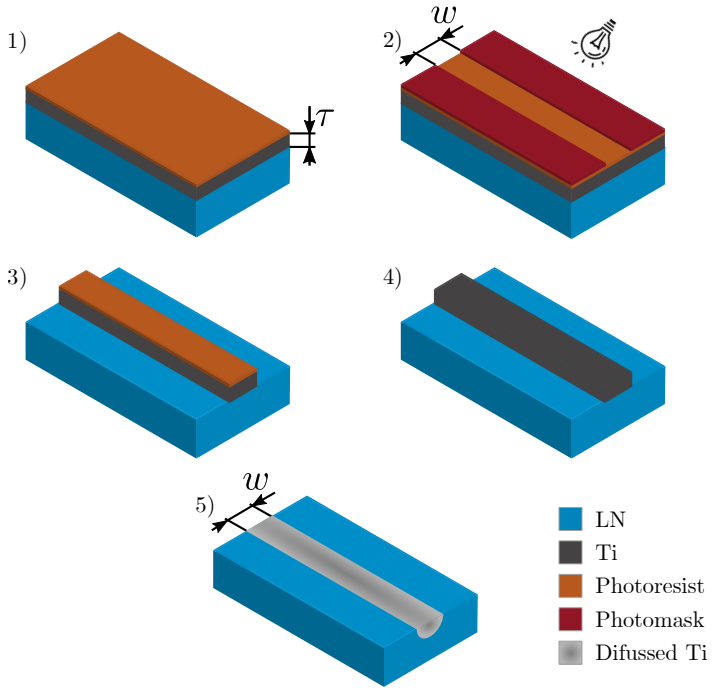

Figure 2.6: Fabrication process of Ti:LN waveguides.

	$532nm$	$1064nm$
d_{31}	1.4	2.4
d_{32}	2.65	4.4
d_{33}	10.7	16.9
d_{24}	2.65	7.9
d_{15}	1.4	6.1

[pm/V]

$$\begin{pmatrix} 0 & 0 & 0 & 0 & d_{15} & -d_0 \\ 0 & 0 & 0 & d_{24} & 0 & 0 \\ d_{31} & d_{32} & d_{33} & 0 & 0 & 0 \end{pmatrix}.$$

2.4.4 Rubidium exchanged KTP waveguides

The most common type of KTP waveguides are Rb exchanged channel waveguides. They were first fabricated by Bierlein et al. in 1987 [32]. They offer high non-linear efficiencies and the integration of electrooptic components on chip. The discussion on the fabrication of Rb exchanged KTP waveguides is out of the scope of this thesis as, contrarily to LN, commercial samples were used.

Nonetheless, the fabrication process is somehow similar. A photomask is used to pattern the waveguide structures, leaving only the desired stripes unmasked for the Rb exchange on a chemical bath. The Rb concentration can then be used to calculate the refractive index increase of the waveguide and the calculation of the effective refractive indexes. The model was developed by the company AdvR Inc.[33] and is the one used for the modelling of the waveguides in this work, with different coefficients following the discussion in [34].

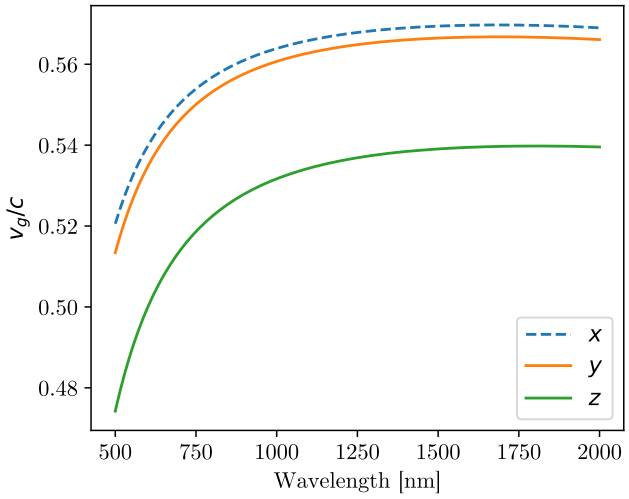

Figure 2.7: Normalised group velocities in KTP for all the cyrstallographic axis.

2.5 Waveguide inhomogeneities and where to find them

As it is often the case in experimental science, things are far from the ideal conditions assumed in the theory. In the case of waveguides and integrated structures, we assumed that the refractive index was constant in y and z and changed in x as the substrate and core materials changed. However, and this comes as no surprise to engineers and technicians working in the fine arts of waveguide fabrication, this is not the case of real waveguide structures.

The PM function defines the non-linear process and it depends on the effective refractive index of the waveguide, reflecting its properties on the final result. In chapter 1 and section 2.4 we learnt how n_{eff} changes with the structure parameters and other experimental conditions such as the temperature of the material. Hence, fabrication and experimental inhomogeneities on waveguide parameters (such as the fabrication parameters resulting in the waveguide width and depth, temperature distribution over the structure and material composition) cause the effective refractive index of the waveguide to vary along z and impact the non-linear process within. In this situation, with the effective refractive index being a function of the propagation axis $n(z)$, the phase-mismatch is not constant for the three interacting fields anymore and must be integrated in the phase-matching function to account for the phase accumulated by the fields as they travel through the inhomogeneous waveguide.

Accordingly, equation 2.2.5c must be changed to

$$\frac{dA_3}{dz} = \frac{8\pi i d\omega_3^2}{c^2} A_1 A_2 \mathrm{e}^{i\int_0^z \Delta\beta(\xi)d\xi}, \tag{2.5.1}$$

with $\Delta\beta(\xi) = \beta_1(\xi) + \beta_2(\xi) - \beta(\xi) \pm 2\pi/\Lambda$. The phase-matching function is then [34, 35]

$$\varphi \propto \frac{1}{L}\int_0^L e^{\mathrm{i}\int_0^z \Delta\beta(\xi)d\xi} dz, \tag{2.5.2}$$

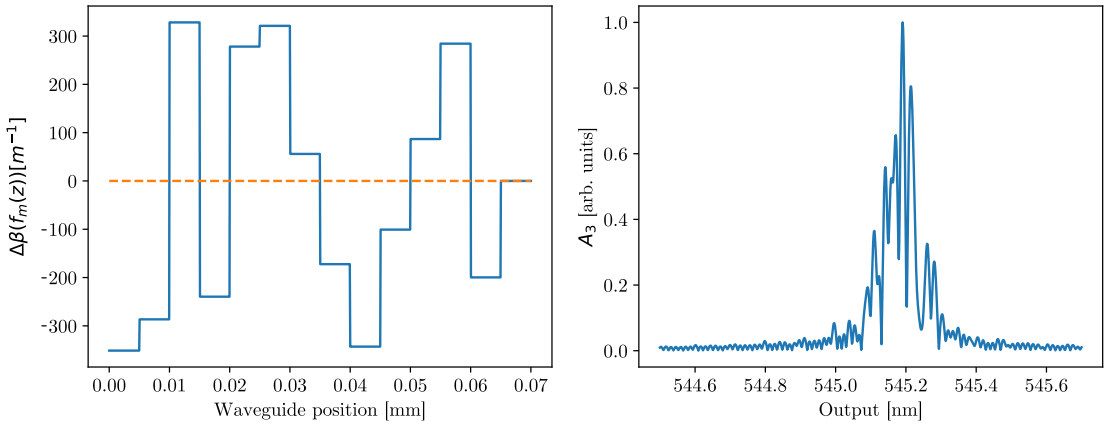

Figure 2.8: On the left, the $\Delta\beta$ variation profile of an inhomogeneous waveguide is shown. The orange dotted line would describe an ideal waveguide. On the right, the PM function resulting from the profile..

which has to be numerically solved for each $\Delta\beta$ profile.

As depicted in figure 2.8, the new phase-matching function will move away from the sinc shape and present asymmetries. This will impact the application of the non-linear process. We will discuss the implications in chapter 5.2.

Chapter 3

A quantum language

The history and development of humankind is strongly linked to that of communication and information technologies. The growth of human groups and societies has driven the development of better and more durable information storage devices as more information needed to be stored and communicated farther [36]. When information started to get too extensive and complicated for oral transmission, human language was translated into physical storage devices such as stones, wax tablets and finally different forms of paper. Communication systems evolved much slower, until the invention of the telegraph, we only had relay towers (using fire or other signals) besides transporting the physical media. That also meant that the storage device was in itself a form of communication and it had to endure and survive transport to reach a receiver. Written storage was only dethroned, after centuries[1], by the invention of computers and the digital revolution in the XX century. Communication devices saw a quicker development from the telegraph, radio waves came and then electrical and optical communication, parallel to the invention of computers, led to the invention of the internet. Computers and the internet revolutionized telecommunications, connecting humans and information all over the earth and getting humankind into the contemporary era.

Using computers, information started to be stored and processed in progressively smaller devices, allowing immense quantities of information to be kept with a small footprint. In fact, Gordon Moore predicted in 1965 in what is known as Moore's law: the number of transistors in a chip would double every 18 months [37], supporting more and more information in smaller devices. Moore's prediction presents an interesting question: with digital devices getting smaller and smaller, what is the limit? They will reach the point at which individual atoms and electrons are involved and quantum effects start to take place. This realisation paved the way for the development of quantum communication and information technologies.

The second half of the XX century saw quantum theory applied to information and computing theories. Contributions such as conjugated coding (invented by Stephan Wiesner in 1968, although unpublished until 1983 [38]; Charles H. Bennett discussed it with Wiesner which pushed Bennett's own efforts forward), the non-cloning theorem by James Park [39] and Alexander Holevo's demonstration of qubits increased information capacity over classical bits [40], led to the foundational

[1] It is actually striking to think that books have been around for millennia now and stay a cornerstone of human knowledge. However, that is probably a biology problem more than physics one. We are still stuck with our natural eyes and brains to perceive information, pray to the Omnissiah.

works of quantum computing with the first proofs by Benioff and Feynman [41, 42], quantum information theory with Ingarden's work [43] and the first quantum cryptography protocols by Bennett and Brassard [44]. All these results demonstrated the higher computational power of quantum inspired schemes, which Preskill named "quantum supremacy" in 2012 [45, 46]. There is a new communication revolution in the horizon, if we manage to handle the quantum world.

To develop and exploit quantum technologies, we need to marry a deep understanding of the theory with the engineering of the new quantum devices. As wide as the field is, the scope of this thesis is the generation of quantum light for information encoding and the processing of such information. Starting from the description of a quantum system, we will describe the quantum states in which we want to encode the information, discuss the properties that a quantum alphabet needs and how to encode and manipulate information in photon states. This is then linked to non-linear processes and how to use them to actually encode and process the information in photon states using real integrated devices. We will mainly follow the concepts as explained by Gianfranco Cariolario in [47], the reader is directed to this work to expand the descriptions given here.

3.1 Hilbert spaces and the quantum alphabet

Quantum states are the objects under study in quantum physics and our aim is to encode information within their properties. We first need to understand what states are and how they are defined.

A quantum state defines the properties of an object in the quantum mechanics framework. The description of states and their environment is conveniently given by the first postulate of quantum physics:

Postulate 1 *The state of an isolated physical system is represented, at a fixed time t, by a state vector $|\psi\rangle$ belonging to a Hilbert space $\mathcal{H}$ called the state space.*

The state vectors $|\psi\rangle$ (note that we have introduced Dirac's braket notation [48]) represent quantum states and they are described within a Hilbert space. A Hilbert space is a complete inner-product complex vector space [47]. The properties and relations defined by such a space, mathematically describe the states. The properties of interest for our discussion are:

1. **Orthogonality**: two states $|x\rangle$, $|y\rangle \subset \mathcal{H}$ are orthogonal if their inner product is

$$\langle x|y\rangle = 0 \tag{3.1.1}$$

2. **Linearity**: a Hilbert space, being a vectorial space, assures that every combination of states $|x\rangle_i$ is a state too,

$$a_1|x\rangle_1 + a_2|x\rangle_2 + ... + a_n|x\rangle_n \in \mathcal{H}. \tag{3.1.2}$$

3. **Bases**: there exists subsets of orthogonal states of $\mathcal{H}$, $\mathcal{B} = \{|b\rangle_i,\ i \in D\}$ called bases, with $D = [1, 2, ..., \mathrm{d}]$ and d the dimension of the Hilbert space, such that

$$\mathrm{span}(\mathcal{B}) = \mathcal{H}, \tag{3.1.3}$$

a basis generates $\mathcal{H}$ through linear superposition of the basis states.

The quantum states of our photons are states of a Hilbert space then. Using a basis, we can describe any state $|x\rangle$ as a linear superposition

$$|x\rangle = \sum_{i \in D} a_i |b\rangle_i, \tag{3.1.4}$$

where the coefficients a_i are the weight of each basis state in the superposition. If all the vectors of the base are normalised, then we obtain an orthonormal basis. Describing a state with a base gives us a natural alphabet, the basis vectors, to encode and read information.

3.2 Operators and projectors: reading quantum states

In quantum mechanics, states are manipulated through mathematical functions called linear operators (we will shorten to operators from now on) that can be described with linear combinations of outer products of the basis vectors of the Hilbert space. Operators are denoted with the hat symbol $\hat{A}$. An operator $\hat{A} = |c_1\rangle\langle c_2|$ transforms a state from a Hilbert space to another state such that

$$|y\rangle = \hat{A}|x\rangle = \langle c_2|x\rangle|c_1\rangle. \tag{3.2.1}$$

Operators $\hat{A}$ as defined, act on kets, $|x\rangle$. We define adjoint operators as the conjugate operator $\hat{A}^*$, that act on bras $\langle x|$, given that they belong to the conjugate Hilbert space: $\langle x| \in \mathcal{H}^*$.

We define now Hermitian operators for which

$$\hat{A} = \hat{A}^*. \tag{3.2.2}$$

Hermitian operators are integral to quantum mechanics due to their properties:

1. **Real eigenvalues**: considering that the eigenvalues of an operator describe its physical properties, they must be real.

2. **Orthonormal eigenvectors**: the eigenvectors of an operator are then a possible basis of the Hilbert space in which they operate. In fact, they are an ideal base to describe the states because allows one to exploit orthonormality relations in the different expansions of the eigenvectors, e.g. HG modes from a Gaussian operator.

3.2.1 Projectors

Projectors are an important type of Hermitian operators as they define one class of quantum measurements, our tool to read states. A projector is a specific kind of operator where $\langle c_2| = |c_1\rangle^*$, defined with

$$\hat{P} = |p\rangle\langle p| \tag{3.2.3}$$

where $|p\rangle$ is a normalized state and the idempotent property $\hat{P}^2 = P$. Applying a projector to a state produces

$$\hat{P}|x\rangle = |p\rangle\langle p|x\rangle = k|p\rangle, \tag{3.2.4}$$

where k is the overlap between $|p\rangle$ and $|x\rangle$. This describes the projection of $|x\rangle$ on $|p\rangle$ very much like a vectorial projection as depicted in figure 3.1. Hence, if we project a state onto the vectors of an orthonormal basis as defined in equation 3.1.4, we will obtain all the coefficients c_i that represent the state in that basis. In other words, with

$$|x\rangle = \sum_i^d \hat{P}_i|x\rangle = \sum_i^d |c_i\rangle\langle c_i|x\rangle, \tag{3.2.5}$$

we can completely describe the state in terms of projectors $\hat{P}I$ up to dimension d, which can in turn be used to read the composition of the state in their basis.

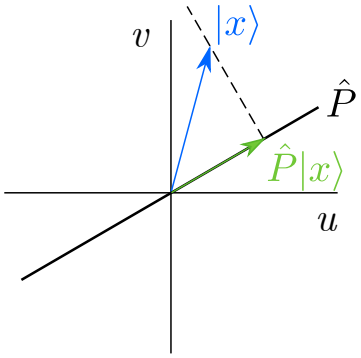

Figure 3.1: Result of applying projector $\hat{P}$ on state $|x\rangle$ on a two dimensional space.

3.2.2 Reading quantum states

The next two postulates manifest the importance of operators and projectors to understand and read quantum states.

Postulate 2 *The evolution of a closed quantum system is described by a Hamiltonian operator* $\hat{H}(t)$.

In the schrödinger (interaction) picture, the evolution is given by:

$$\mathrm{i}\hbar\frac{\partial}{\partial t}|\psi\rangle = \hat{H}(t)|\psi_0\rangle \tag{3.2.6}$$

with $|\psi_0\rangle$ the state at $t = 0$. The Hamiltonian describes the evolution of the total energy of the state through time. Now, at any point in time we might want to measure one property of the state, called an observable.

Postulate 3 *If* $\hat{A}$ *is an observable with eigenvalues* a_i*, then* $\hat{A}$ *may be described by*

$$\hat{A} = \sum_i a_i P_i \tag{3.2.7}$$

with P_i *projectors of the observable eigenvectors.*

When measuring with an observable, the result is always an eigenvalue of the observable.

Therefore, it's advantageous to use the eigenvectors of the observable (which constitute a basis set) to describe a general state, since

$$\langle\psi|\hat{A}|\psi\rangle = \sum_i |c_i|^2 a_i. \tag{3.2.8}$$

3.3 Encoding information in photon states

We have described our states with basis sets that allows us to write them as the superposition of many vectors. The basis vectors are an alphabet with which to encode information in the states. For that, we have to choose a degree of freedom (an observable of the space) to encode the information. Photons have many degrees of freedom available for information encoding. Polarization is the first one to come to mind, as it was one of the first bases used for entangled photon sources, demonstrated by Kwiat et al. in 1995 [49], and we will use it to demonstrate a simple information encoding scheme in a two-dimensional space.

The polarization space can be described with the basis vectors $|\leftrightarrow\rangle$ and $|\updownarrow\rangle$, representing horizontal and vertical polarization respectively. The photon state can then be describe with

$$|\psi\rangle = c_1|\leftrightarrow\rangle + c_2|\updownarrow\rangle, \tag{3.3.1}$$

where the coefficients must be normalized so that $\sum_i c_i^2 = 1$. A state as the one described by equation 3.3.1 is called a qubit, a quantum bit where the 0 and 1 classical values are now the two polarizations. To read this information, we just have to project the state into both polarizations.

The horizontal and vertical polarization vectors are in fact eigenvectors of the polarization observable and they have allowed us to write the state in its most natural form. Furthermore, by describing operators and observable in matrix form, observable are diagonal matrices and projecting them is as simple as the matrix multiplication

$$\begin{pmatrix} c_1 & 0 \\ 0 & c_2 \end{pmatrix} \begin{pmatrix} P_1 \\ P_2 \end{pmatrix} \tag{3.3.2}$$

3.3.1 Temporal modes

Virtually any physical quantity of a photon is available for information encoding, it is up to the application which one is more suitable. For example, polarization is limited to two dimensions which limits applications and the amount of information that it can carry, transverse spatial modes have no dimensional limitation but are not compatible with spatially single-mode guided optics.

Energy is a third option. Information can be encoded in the time-frequency spectrum of photons. This method supports an infinite dimensional Hilbert space while maintaining a single spatial mode. This makes time-frequency encoding compatible with off-the-shelf spatially single-mode telecommunication optics components, a huge advantage for telecommunication applications. To describe states in the time-frequency domain, we need bases that allows us to describe the time-frequency components of any photon state. One such a basis are temporal modes [50].

The states can then be written as a superposition of a continuum of single-photon states at frequencies ω:

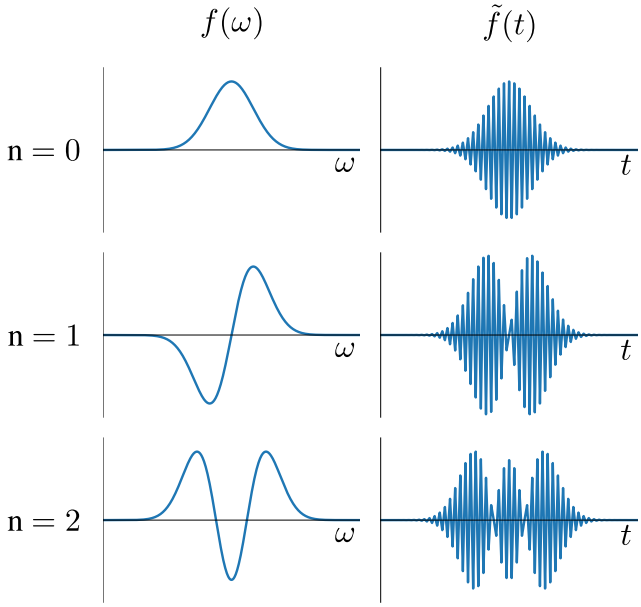

Figure 3.2: The spectral distributions in frequency (left) and time (right) of the three first modes n of a HG temporal modes basis.

$$|A_f\rangle = \int \frac{d\omega}{2\pi} f(\omega)\hat{a}^\dagger(\omega)|0\rangle, \tag{3.3.3}$$

where $f(\omega)$ is a complex function describing the spectral distribution of the wave-packet, $\hat{a}^\dagger$ is the standard creation operator at frequency ω and $|0\rangle$ is the quantum vacuum state[2]. Basically, $f(\omega)$ describes the probability of a photon being created at a certain frequency. The state can be translated into the time domain through a Fourier transform

$$|A_f\rangle = \int dt \tilde{f}(t)\hat{A}^\dagger(t)|0\rangle, \tag{3.3.4}$$

which now represents photons being created at different times t. Due to this relation between frequency and time modes, we generalise and call them temporal modes[3].

It is useful to define a broadband operator $\hat{A_f}^\dagger$,

$$\hat{A_f}^\dagger = \int dt \tilde{f}(t)\hat{A}^\dagger(t) = \int \frac{d\omega}{2\pi} f(\omega)\hat{a}^\dagger(\omega), \tag{3.3.5}$$

that generates the state $|A_f\rangle = \hat{A_f}^\dagger|0\rangle$.

States in general can have any $f(\omega)$ but, if we want to build the basis for our Hilbert space, we must find sets of functions that are orthogonal. As discussed, the natural basis are the eigenvectors

[2] A state containing no photons.

[3] Sometimes they can also be known as time-frequency or pulsed modes.

of the observable under investigation, the energy. For a Gaussian-like state, we can use Hermite-Gaussian (HG) functions up to the n^{th} order to obtain the temporal mode basis of an n-dimensional space. The first three HG temporal modes are depicted in figure 3.2. Now we can write any single-photon state by expanding equation 3.1.4 with

$$|\psi\rangle = \sum_{n=0}^{\infty} c_n \hat{A_n}^{\dagger} |0\rangle. \tag{3.3.6}$$

Here, each broadband operator $\hat{A_n}^{\dagger}$ generates the single-photon state at each basis temporal mode n up to dimension d. Note that this can span an infinite-dimensional Hilbert space. How do we exploit such a framework? We need devices to generate states encoded in this TM and to process and read them In the next sections, we review non-linear processes for these applications.

3.4 Quantum non-linear optics: parametric down conversion

Parametric down conversion[4] (PDC) can be considered a special case of DFG process that can only be explained from quantum mechanics as there are two inputs containing the quantum vacuum state $|0\rangle$. The process is illustrated in figure 3.3. In the process a pump photon decays into two photons (signal and idler) that sum to the original frequency, $\omega_p = \omega_s + \omega_i$. This state containing two photons is often called a bi-photon state.

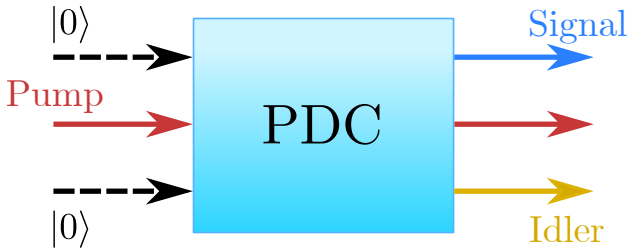

Figure 3.3: Schematic description of PDC process with an undepleted pump field.

The process was first proposed by Louisell, Yariv and Siegman in 1961 [51] (with a follow-up in 1963 [52]) when studying optical parametric amplifiers under quantum mechanics. The field quantization of the parametric amplifier resulted in two output modes generating photons whose amplitude and phase depend on the original pump and showed correlation.

PDC was first demonstrated experimentally during the hype of experimental non-linear results in the late 60s. Harris et al. and Magde et al. produced PDC in two different non-linear media [53, 54]. Since then, PDC increasingly gained attention as a reliable source of bi-photon states and its capability to generate entanglement (non-classical correlations) between the two generated photons (particularly type II PDC).

The PDC states are described, in the interaction picture and ignoring time ordering effects, by

[4] Also known as spontaneous parametric down conversion.

$$|\psi\rangle^{\mathrm{PDC}} = \exp\left[\frac{1}{\mathrm{i}\hbar}\int_T d\tau \hat{H}^{(\mathrm{PDC})}(\tau)\right]|\psi_0\rangle^{\mathrm{PDC}}, \tag{3.4.1}$$

with T the time of interaction of the fields, $|\psi_0\rangle^{\mathrm{PDC}}$ the state at the interaction starting time and $\hat{H}^{(\mathrm{PDC})}$ the Hamiltonian of the PDC process. In general, the Hamiltonian does not commute with itself at different times, leading to a complicated time integra. Therefore, we limit our study to the low gain regime where time ordering effects can be neglected. The Hamiltonian describes the interaction of the three fields with the non-linear medium within the waveguide and reads [55]

$$\hat{H}^{(\mathrm{PDC})}(t) = \varepsilon_0 \int dz \chi^{(2)} \hat{\mathbb{E}}_p^{(+)}(z,t)\hat{\mathbb{E}}_s^{(-)}(z,t)\hat{\mathbb{E}}_i^{(-)}(z,t) + \mathrm{h.c.}, \tag{3.4.2}$$

where

$$\begin{aligned}\hat{\mathbb{E}}_{\mathrm{n}}^{(+)}(z,t) = \hat{\mathbb{E}}_{\mathrm{n}}^{(-)\dagger}(z,t) = \\ = \int d\omega_{\mathrm{n}} f_{\mathrm{n}}(\omega_{\mathrm{n}})\hat{a}(\omega_{\mathrm{n}})e^{\mathrm{i}(\beta_{\mathrm{n}} z - \omega_{\mathrm{n}} t)}\end{aligned} \tag{3.4.3}$$

are the electric field operators [56]. $f(\omega_{\mathrm{n}})$ can be taken outside the integral under the slowly varying approximation. Furthermore, as the pump is considerably stronger than the generated fields, we can substitute $\hat{\mathbb{E}}_p^{(+)}(z,t)$ with the classical field [57]

$$\mathbb{E}_{\mathrm{p}}(z,t) = \alpha(\omega_{\mathrm{p}})e^{\mathrm{i}(\beta z - \omega_{\mathrm{p}} t)}. \tag{3.4.4}$$

Gathering all this and performing straightforward operations, the resulting Hamiltonian is given by

$$\hat{H}^{(\mathrm{PDC})}(t) = A\int dz d\omega_{\mathrm{p}} d\omega_{\mathrm{s}} d\omega_{\mathrm{i}} \hat{a}_{\mathrm{s}}^{\dagger}(\omega_{\mathrm{s}})\hat{a}_{\mathrm{i}}^{\dagger}(\omega_{\mathrm{i}})\alpha(\omega_{\mathrm{p}})e^{\mathrm{i}(\Delta\beta z - [\omega_{\mathrm{s}}+\omega_{\mathrm{i}}-\omega_{\mathrm{p}}]t)}. \tag{3.4.5}$$

One can recognize the exponential term $e^{\mathrm{i}\Delta\beta z}$ whose integral resulted in 2.2.9. Finally, by performing the integral over z for the waveguide length L and substituting in equation 3.4.1, we obtain the PDC state in the low gain regime

$$\boxed{|\psi\rangle^{\mathrm{PDC}} = \int d\omega_{\mathrm{s}} d\omega_{\mathrm{i}} \hat{a}_{\mathrm{s}}^{\dagger}(\omega_{\mathrm{s}})\hat{a}_{\mathrm{i}}^{\dagger}(\omega_{\mathrm{i}})\alpha(\omega_{\mathrm{s}}+\omega_{\mathrm{i}})\varphi(\omega_{\mathrm{s}},\omega_{\mathrm{i}})|\omega_{\mathrm{s}}\rangle|\omega_{\mathrm{i}}\rangle.} \tag{3.4.6}$$

Retracing to our definition of the TF in equation 2.3.6, with the product of the pump envelope $\alpha(\omega_{\mathrm{s}}+\omega_{\mathrm{i}})$ and the PM function of the process $\varphi(\omega_{\mathrm{s}},\omega_{\mathrm{i}})$, we can see that PDC state can be described in the same fashion. In the PDC case, the TF is better called the joint spectral function (JSA) as it describes the joint properties of the output bi-photon state instead of the input/output relation of SFG. Photons are created at the frequencies and with the probability dictated by the JSA function, which ensure energy and momentum conservation. The JSA function of the PDC state describes the frequency (and time through a Fourier transform) correlations between the two generated photons as it can be seen in the PDC JSA function depicted in figure 3.4.

3.4.1 Finding PDC temporal modes

Since the JSA describes the energy of the state, it can be used as an observable of the biphoton state. Then, there exists a basis set (constituted by the eigenvectors of the JSA) that naturally decomposes it. However, things are not that easy: we are considering a state composed of two distinguishable photons. Therefore, we actually need to find two separate bases, one for each photon to fully describe the JSA. Luckily for us, the Schmidt decomposition of a two dimensional function returns the eigenvectors of both dimensions, yielding

$$|\psi\rangle_{\mathrm{PDC}} = \sum_{\mathrm{k}} \sqrt{\lambda_{\mathrm{k}}} \hat{A}^{\dagger}_{\mathrm{k}} \hat{B}^{\dagger}_{\mathrm{k}} |0\rangle, \tag{3.4.7}$$

if we only consider the two-photon components and disregard higher order photon contributions. Here $\sqrt{\lambda_{\mathrm{k}}}$ are the weights of each bi-photon mode k, normalised to $\sum_{\mathrm{k}} \lambda_{\mathrm{k}} = 1$, and $[\hat{A}^{\dagger}_{\mathrm{k}}, \hat{B}^{\dagger}_{\mathrm{k}}]$ are two sets of orthonormal eigenvectors, one for each photon [58]. Note that we have used the broadband mode notation. This describes any PDC state in a series of temporal modes, as depicted in figure 3.4. The Schmidt number $K = \sum_k 1/\lambda_k^2$ describes the effective number of modes that contribute to the description of the state and the state rank is defined by the number of non-zero modes in the decompositionm, i.e. the number of modes k in the sum in equation 3.4.7.

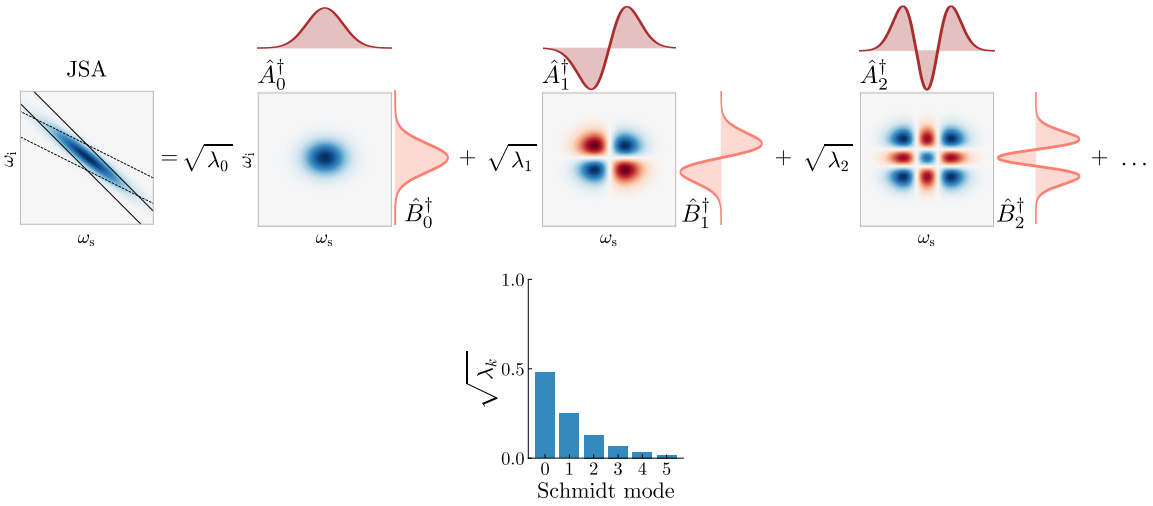

Figure 3.4: JSA function of a PDC process as a function of the signal and idler frequencies. This PDC state has $K \approx 20$ and infinite rank. The solid and dashed lines mark the FWHM of the pump field and PM function respectively. The JSA function is decomposed into pairs of modes $\hat{A}^{\dagger}$, $\hat{B}^{\dagger}$ through the Schmidt decomposition. The first three modes are shown with their coefficients. On the bottom, the distribution of the Schmidt coefficients is shown up to the fifth coefficient.

The temporal mode distribution of the state will then be determined by the properties of the JSA. These properties are given by the phase-matching conditions (including the group velocities for pulses and the dispersion properties) and the spectral envelope of the pump field. Given control over these parameters, we can engineer the TM content of the PDC JSA function.

3.5 The quantum pulse gate

We have found a source for our temporal mode-encoded photons in the PDC process. How can we read the TM composition of these states? From previous sections, we know that we can use projectors to measure an observable. We have used the eigenvectors of the Hamiltonian to unearth the temporal modes in the bi-photon state, now we need to implement experimentally these eigenvectors as projectors to measure the temporal mode distribution coefficients $\sqrt{\lambda_k}$.

The quantum pulse gate (QPG) is a mode selective process developed in the last decade to sort temporal mode-encoded states of light [50, 59–61]. It is analogous to a beam splitter acting on two TMs $|A^\zeta\rangle$ and $|B\rangle$ instead of the polarisation or spatial modes. The sketch in figure 3.5 illustrates the operation. The QPG is defined by an operator $\hat{Q}^\zeta$ that acts on an arbitrary input state

$$|\psi\rangle_{\text{out}} = \hat{Q}^\zeta |\psi\rangle_{\text{in}}, \tag{3.5.1}$$

with

$$\begin{aligned}\hat{Q}^\zeta =& \mathbb{1} - |A^\zeta\rangle\langle A^\zeta| - |B\rangle\langle B| \\ &+ \cos\theta \left(|A^\zeta\rangle\langle A^\zeta| + |B\rangle\langle B|\right) \\ &+ \sin\theta \left(|B\rangle\langle A^\zeta| - |A^\zeta\rangle\langle B|\right).\end{aligned} \tag{3.5.2}$$

Here, $|A^\zeta\rangle$ is the single input mode, $|B\rangle$ the output mode and θ the efficiency of the conversion process from $|A^\zeta\rangle$ to $|B\rangle$.

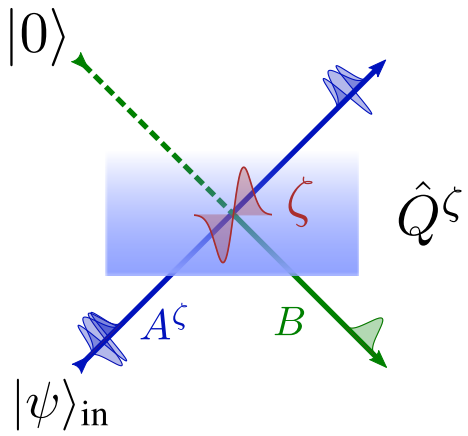

Figure 3.5: Schematic describing the analogous QPG/Beam-splitter operation. The QPG operates on two modes: the input mode defined by the temporal mode ζ and the output mode $|B\rangle$. In this example, the input state $|\psi\rangle_{\text{in}}$ contains a superposition of three TMs that enter mode A^ζ. Then, only the modes that overlap the TM defined by ζ are converted to mode B and the rest continue in A^ζ.

For an input state $|\psi\rangle$, a detected photon from the output mode $|B\rangle$ is a projection of $|\psi\rangle$in onto mode $|A^\zeta\rangle$, where $|A^\zeta\rangle\langle A^\zeta|$ is a projector of a measurement basis defined by the user by programming the spectral envelope of ζ. The parts of the input state that have a zero projection on

the selected mode are transmitted through $|A^\zeta\rangle$ unperturbed. The process ensures perfect single-mode operation in $|A^\zeta\rangle$ to select the proper modes out of the input state. The operator has a single eigenvalue defined by the desired mode.

Such a process can be used to project the PDC states described earlier into their basis vectors, therefore reading the TM composition of the state. The PDC photons are sent to a QPG device, where the mode $|A^\zeta\rangle$ is sequentially set to the different TMs basis states to obtain the distribution of the state from a measurement of the output mode with photon counting techniques. The output mean photon number in the output mode is

$$\langle N^\zeta\rangle = N_{\text{in}}\sin^2\theta|\gamma^\zeta|^2, \tag{3.5.3}$$

where N_{in} is the number of photons in the input and γ^ζ the overlap between the input mode $\langle A^\zeta|$ and the input state $|\psi\rangle_{\text{in}}$. The measured photon number in the output is then proportional to the projection of the input state on ζ. The operation of the QPG is depicted in figure 3.6.

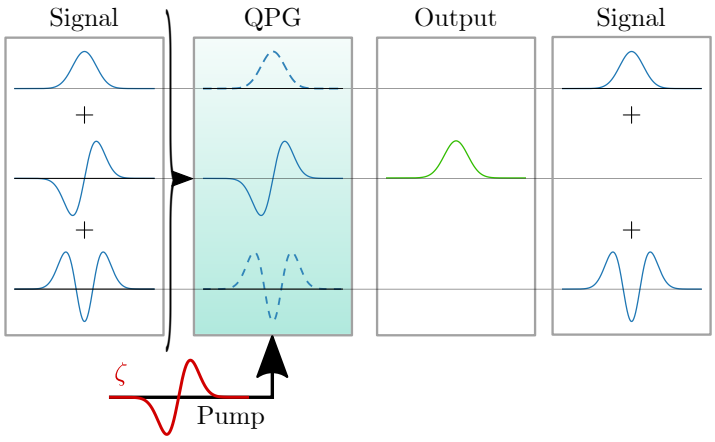

Figure 3.6: Schematic description of a QPG operating in the temporal mode ζ of the pump field. The signal input is described by a superposition of three TMs. The QPG "reads" those input modes that match with the pump, , converting them to the output mode $|B\rangle$. The rest of the signal (in dashed lines on the QPG) propagates through the QPG unconverted.

3.5.1 QPG non-linear device realisation

The QPG is defined by its single-mode operation. To implement such a process in a real device, we have to find a conversion process that features a single-mode JSA. Such a process can be found in a type II GVM SFG in Ti:LN waveguides [50, 59]. Group velocity matching (GVM) between pump and signal ensures a flat JSA as depicted in figure 3.7, which, after the filtering of the PM sinc function sidelobes, contains a single temporal mode for input and output. This is due to the dependence of the phase-matching angle on the group velocities of the fields as discussed in section 2.3: at GVM, the PM function angle is 0°.

By shaping the pump into the different modes of the TM basis, one can read out the input state TM composition at the output of the QPG. The conversion efficiency for pump mode ζ describes the efficiency of the QPG device used, $\eta_{\text{QPG}} = \sin^2\theta$.

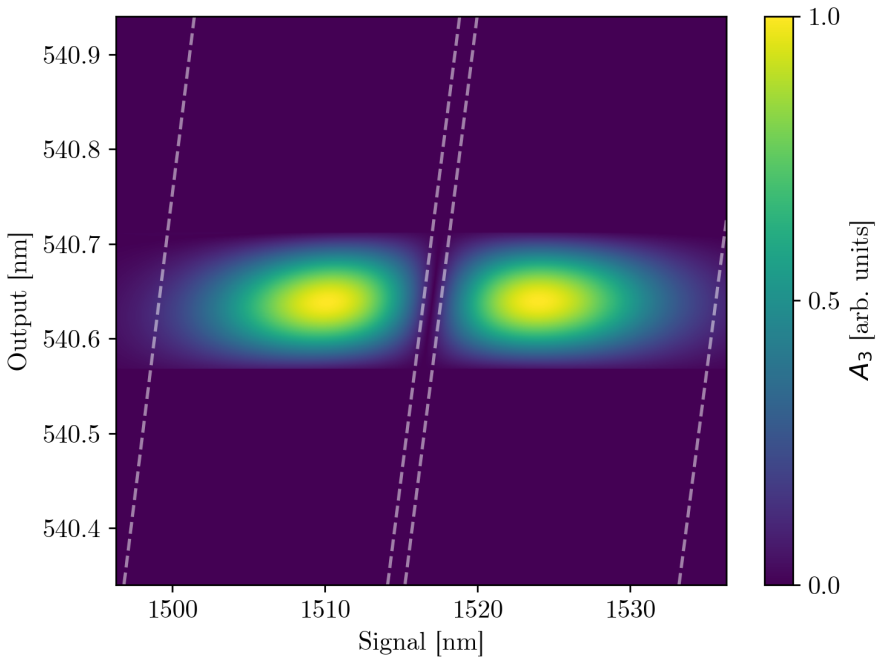

Figure 3.7: TF of a QPG device with the pump on the first order HG mode. The process is the same as in 2.4 but at 200°C which shifts the group velocities such that pump and signal are at GVM. The FWHM of the pump field is marked with dashed lines. The output has been filtered matching the width of the PM function to obtain a single-mode TF. It can be seen how the angle of the pump on the TF causes parts of the mode to overlap in the output axis, thus the spectral correlations.

Lithium niobate offers an interesting choice for the group velocity matched frequencies. From the group velocities depicted in figure 2.5, we can see that have a pump in the near infrared (∼850nm) and an input signal in the telecom range (∼1550nm). This allows for a QPG process that can read information encoded in temporal modes in photons in the telecom, where off-the-shelf telecommunication optical components can be used. Furthermore, the shape of the JSA also works as a bandwidth compressor between the input and output with no loss of information. This is possible when the PM function bandwidth is narrower than the input signal bandwidth. Then, the converted output is compressed down more efficiently than through spectral filtering [62].

3.5.2 The mode selectivity

The performance of the QPG as a mode sorter can be measured from its capability to discriminate between the modes of the input. An ideal QPG converts exactly the overlap between the input state and ζ without any contributions from different modes (crosstalk). Ideal operation is not possible

with the SFG implementation due to the spectral correlations caused by the pump at 45°[5], as can be seen in figure 3.7.

The temporal mode selectivity of the QPG can be quantified with the modal information in the JSA. We define the selectivity [63]:

$$\mathrm{S}_j \coloneqq \frac{|\sqrt{\lambda_\mathrm{j}}|}{\sum_{\mathrm{n}=0}^{\infty}|\sqrt{\lambda_n}|}|\sqrt{\lambda_\mathrm{j}}|, \tag{3.5.4}$$

where j is the index of the desired mode and n sums over all of the JSA modes. The first factor $|\sqrt{\lambda_\mathrm{j}}|/\sum_{\mathrm{n}=0}^{\infty}|\sqrt{\lambda_n}|$ describes the crosstalk between different modes, the second factor $|\sqrt{\lambda_\mathrm{j}}|$ is the conversion efficiency for that mode. This definition quantifies the overlap between the desired mode and all the other possible modes in the process. The ideal process would have S=1 and as correlations are introduced in the TF, the process deviates from ideal reducing the selectivity S<1. The effect of this correlations scales with the bandwidth of the PM function, increasing the selectivity as the bandwidth narrows. Hence, the longer the QPG device the better the selectivity.

Another quantity of experimental interest can be defined from the selectivity, the modal extinction ratio

$$\varepsilon = -10\log_{10}(\sqrt{S}). \tag{3.5.5}$$

It can be directly measured experimentally as the ratio of the converted output for a fixed signal and two pump modes: one equal to the signal and one in another orthogonal mode. The extinction ratio allows one to measure the selectivity of the process avoiding a measurement of the JSA, which would require the experimentally challenging measurement of the spectral phase.

[5]The angle depicted is not 45° due to the different scaling of the signal and output axes.

Part II

Design and application of Quantum non-linear devices

> Invention, it must be humbly admitted,
> does not consist in creating out of void
> but out of chaos.
>
> *Mary Wollstonecraft Shelley*

In the previous sections we introduced all the necessary principles of waveguides, non-linear processes and quantum physics to understand the results of this thesis. We shall now review the state of the art of quantum communication photonic devices and investigate how quantum non-linear devices are currently designed and exploited. In particular, we are interested in processes encoding information in photon states and devices capable of reading, processing and using that information. After such a review, we will find ourselves at the edge of photonic technology development, where the experimental results of this thesis reside. The work presented here aims at overcoming the current limitations and advancing quantum non-linear technologies. For that, we will present solutions for the limitations and new design paradigms to engineer and exploit quantum light.

Chapter 4

Quantum networks: state of the art

The foundations of quantum communication science discussed in part I quickly expanded into specialised fields aiming to build the basic building blocks of quantum information technologies. Using these building blocks, the quantum dream is to develop quantum devices to improve over classical communication systems, exploiting intrinsically quantum effects like entanglement and energy quantisation. Ideally, we want to build new, safer, quicker, more efficient and powerful communication channels around quantum phenomena. These could be pictured as quantum communication networks transmitting and processing quantum information between nodes of the network. Each node would have different integrated components to perform quantum tasks: measurements, encoding, processing, encrypting, storing... To this end, we have seen the birth of quantum memories, repeaters, processors, interfaces, measurements, communication protocols and algorithms that allow to work with quantum information and beat classical limits, like binary encoding and linear computational power scaling [45, 64, 65]. Ultimately, for these networks to be convenient, the components must work together and have as small a footprint as possible, building the processes into integrated platforms very much like current electronics. The efforts to build these integrated devices are now at the frontier of science and they advance, hand in hand, through a combination of fundamental theoretical work and experimental efforts.

Quantum network components are in development in many different frameworks and platforms each with its advantages and drawbacks (mainly divided in superconducting, solid-state and photonic approaches) which implies that, at least in the beginning, we will rely on very different components working with each other. Hence, when designing new components and systems, a broad view of the whole field helps not miss previous works that can be used and set realistic goals for the properties of the devices that we will design and exploit in this work.

The results of this thesis revolve around the discrete variable photonic approach, defined by the use of qubits as opposed to continuous variable approaches. The qubit is the root of our systems, we need devices that transmit and manipulate them, maintaining their properties. This can be detailed with the DiVincenzo criteria [66]. In 2000, DiVincenzo provided seven requirements for the implementation of quantum computation which can be used as guidelines for the general design goals of any quantum device.

In order to design the proper quantum devices, we need to know their requirements and these

are intrinsically linked to each device and platform and how qubits interact with them: the frequencies accepted, the power thresholds, the spectral properties, polarization... all particular to each problem. My work focusses on the generation of photon qubit states, the interface of different nodes and devices of the quantum network and quantum measurements. Thus, to aim the efforts true, it is important to know what properties different platforms have so that we can generate processes that interface information travelling through them. To this end, in this chapter we review the state of the art of different quantum technologies. This will set the context for the results of this thesis, where we will design new schemes to interface devices and process quantum information in temporal modes of light compatible with already existing technologies. Furthermore, the challenges faced for the chip integration of these devices are explained and put into context.

4.1 Quantum light sources

The performance of each piece of a quantum network is critical but, arguably, without a high quality source of photons we would have nothing to work with. Quantum light sources generate photonic qubit states on different degrees of freedom for their exploitation in the quantum network. Photons are chosen as quantum information carriers as they fulfill the main five main DaVincenzo criteria: they can describe qubit states, they can be generated in well-defined states, have long decoherence times, can be manipulated via unitary operations (although usually not deterministically) and be characterised with specific well-defined measurements.

The ideal photon source emits pure indistinguishable single-photons at 100% efficiency on a clocked trigger event. This triggering condition defines a deterministic source. Purity measures the mixedness of the generated photon state: a pure quantum state is a coherent superposition of states while a mixed state is a statistical mixture of pure states. A low purity state is one with a high number of incoherent modes. These two properties, purity and efficiency, define the quality of a source. The efficiency of the source describes how often we actually expect a photon at a trigger event; 10% efficiency means that we'll find a photon in ten out of ten events.

Certainly, the ideal photon source is physically impossible and limited by the source system: optical absorption, losses, diffraction, spatial mode mismatch, noise emission (photons at undesired times/frequencies), spectral correlations... Nonetheless, single-photon sources are designed with the ideal source in mind and reducing every source of error as much as possible to obtain pure, efficient emission. The quantum properties of the system, in particular the purity of the generated single-photon state, are important for the performance of the device.

The second order correlation function $g^{(2)}(t)$ is a common tool in the characterization of single-photon states [67–69]. It measures the correlation in time of two electromagnetic fields. In the density matrix description of the state, the function describes the time evolution of the diagonal elements. For photons, this is a measure of the flow of photons in time and can be used to identify the purity of single photon states. It is defined with

$$g^{(2)}(t) = \frac{\langle(\hat{a}^\dagger(t)\hat{a}(t)\hat{a}(t+\tau)^\dagger\hat{a}(t+\tau)\rangle}{\langle\hat{a}^\dagger(t)\hat{a}(t)\rangle\langle\hat{a}^\dagger(t+\tau)\hat{a}(t+\tau)\rangle} \tag{4.1.1}$$

with a the photon destruction operator and τ a infinitesimally small increment of time. For deterministic sources, when the presence of a single-photon state is known, the correlation function is used to measure the purity of the single-photon state. In this situation, a pure single-photon has a value of heralded $g^{(2)}(0) = 0$ and it increases towards 1 as the mixedness of the state increases.

For undeterministic sources, the unheralded correlation function can be used. In that scenario, the function measures the bunching of photons in time and their spectral purity, and a pure single-photon state is identified with a value of $g^{(2)}(0) = 2$, decreasing to 1 as photons bunch together reducing the purity.

There are two approaches to quantum light sources: single emitters (usually semiconductor based) that provide deterministic single-photon emission naturally and nondeterministic sources usually based on PDC processes. Let us review the properties of some of the latest results for these sources.

4.1.1 Single emitters

Single emitters are generally built upon atomic ensembles in semiconductor material systems such as quantum dots and other electrically driven solid-state quantum emitters. Quantum dots (QD) typically emit in the visible and near infrared bands and have demonstrated high purity and efficiency, and narrow bandwidth emission (sub-GHz). The latest result from Tomm et al. [70] shows a quantum dot with 57% efficiency at 930nm with a spectral bandwidth of 0.30GHz. Per contra, they are not naturally spatially single-mode and, due to the semiconductor platform, they work at cryogenic temperatures which makes integration within the quantum network cumbersome. Other platforms like wide bandgape epitaxial QDs or defect state based single emitters, are promising towards room temperature operation but their fabrication is still technologically challenging and have only been demonstrated at temperatures around 10K. For a full review on solid-state single-photon sources, the reader is referred to [71].

The narrow bandwidth of the emission is a good match to directly interface with some quantum memories without any interfacing. On the other hand, temporal characterisation of such narrow emission is hard in the emitted frequencies so interfacing with the proper characterisation instruments requires frequency conversion. Furthermore, the spatial mode distribution is a problem for single-mode optics, needing either filtering or to use free space transmission.

4.1.2 PDC sources

We introduced PDC in section 3.4, a non-linear process that produces pairs of photons. As discussed, it is a spontaneous process and the generation of a photon pair is probabilistic. To generate a single photon state, the detection of one of the two photons heralds the existence of the other. In this way, one can probabilistically generate single-photon states. The probabilistic nature of heralded schemes can be overcome with multiplexing techniques. Multiplexed sources is not the focus of this thesis, the reader can consult [72] for an excellent review of multiplexed PDC sources and further insight into quantum light sources. Alternatively, instead of using PDC and multiplexing to have a deterministic source, the two photons can be exploited to generate states entangled in different degrees of freedom. Either way, to effectively use a PDC source within a quantum network, we need to match its operation parameters (such as central frequency or spectral bandwidth) to the other components. Moreover, by tailoring the JSA function of the process, one can engineer the two photon state properties. For instance, high purity single-photon states as well as interesting high-dimensional photon states. Currently, these have been achieved through spectral filtering which reduces the efficiency of the source.

LN and KTP are two of the most common platforms for PDC processes because they can generate photons in the telecom IR band which are directly compatible with telecom optical components.

However, their typical bandwidths of the generated PDC photons are in the 100GHz range which is too broad to connect with most quantum memories.

Current PDC sources (KTP bulk or waveguide) have achieved purities as high as 98% [73], 90% [74] and 80% [29]. Engineering of the process has allowed uncorrelated pure states with unheralded $g^{(2)} = 1.92$ [74] and $g^{(2)} = 1.86$ [29]. Other works have had great success using bulk BBO obtaining efficiencies of 97% and purity of 99% [75].

4.2 Quantum memories

The need for quantum memories might be the more logical from the classical communication analogy. Ideal quantum memories store qubits for a certain time before they are re-emitted or read out preserving their quantum properties: entanglement, purity, correlations... Quantum memories not only allow for the storage of quantum information but are a key building block for other quantum network components.

Even if perfect single-photon sources were available, many quantum information schemes are not deterministic. Quantum memories can counter this by storing single-photon states until the process is ready for further interaction. In that sense, they can be used to build quantum repeaters for long-distance communication, be used to multiplex an underterministic source or aid in communication protocols. Quantum memory applications are out of the scope of this thesis and the reader can consult the references [76, 77] for in-depth reviews of the state of the art of quantum memories and applications. Here, we will focus on reviewing the properties of the main platforms and the implications they have in the design of quantum networks.

There are many approaches to quantum memories: rare-earth ion dope solids, diamond color centres, quandum dots, crystalline solids, Raman memories, alkali metal vapours and molecules.

Platform	**Bandwidth**	**Central frequency [nm]**
Rare-earth	10^2MHz	Visible to Telecom
NV centers	10^2MHz	637, 700, 800
QDs	∼1GHZ	NIR
Rb memories	6MHz	780
Alkali gas	1kHz	NIR
Atomic ensemble	MHz to GHz	NIR
Cs memories	few GHz	NIR
Diamond memories	10^2THz	UV to IR

Table 4.1: The storage properties of several quantum memory systems. Central frequencies specified in a range (like NIR) are usually widely tunable within that range.

In short, they all store the qubit in some kind of atomic transition or energy exchange and this is what defines their performance: what bandwidth and central frequency can be stored, for how long and up to which fidelity[1]. The general characteristics of stored photons in several quantum memory platforms are summarised in table 4.1.

It is immediately clear from table 4.1 that there are many approaches to quantum memories with very different properties although strongly restricted. In general, most accept very narrow bandwidths in the GHZ range or narrower with the exception of diamond memories. Comparing with the bandwidths of single-photon sources discussed earlier, one can see the easy interplay of most quantum memories with quantum dot sources where PDC sources will need bandwidth compression. Most memories are limited to NIR photons with a few exceptions. Every platform has advantages and disadvantages and the choice depends on the application and the resources available. Hence, it is very important to tailor the properties of our photon sources to match the requirements of the quantum memory that better matches the final aim of the application. Another option, when we want to use a particular source and a particular memory that are not compatible, is to use frequency conversion processes to convert the frequencies and manipulate the bandwidths.

4.3 Quantum information processing

At this point, we have discussed both photon sources and quantum memories to store qubits. In order to complete a quantum network under the DiVincenzo criteria we are missing more flexible devices[2] to process the information and to interface all the components. Non-linear frequency conversion processes are very useful, as they can adapt the spectral properties of one state to the ones of a target device. However, these processes must maintain the quantum properties of the original fields. In this scenario, quantum frequency conversion (QFC) is introduced. They convert photon frequencies and modify their spectral properties through the TF in a way that can be engineered and interacts coherently with the quantum properties [78].

One of the main uses for QFC is converting photons from one frequency to another, or compressing/expanding their bandwidth to facilitate interfacing between different devices. For instance, with QFC we can interface photons from a light source in the telecom to a quantum memory in the NIR or transform the NIR emitted single-photons of a quantum dot to the telecom range for better transmission and detection. Furthermore, the bandwidths can be compressed to fit the requirements of different components with a TF with an output bandwidth narrower than the input signal [62].

Regarding the information processing, we need so called unitary gates[3] which are sets of quantum measurements, projectors and operators described by unitary Hermitian matrices. For instance, in section 3.5 we described the QPG, a device that can be used to determine whether or not a given state is in a user controlled temporal mode. Moreover, the QPG combines the processing of the information with QFC, an ideal device to reduce the number of components of the quantum network. We can use the characteristics described in chapter 2 to compare different second order non-linear QFC processes integrated in waveguides and their performance as interfaces and/or TM sorters in table 4.3.

These results give a good overview of the possibilities of QFC processes. The frequencies are not mentioned because the processes can generally be tuned and engineered for a wide range of input

[1] In this context, the fidelity measures the overlap between the original state and the state after the storage.
[2] Given in certain cases quantum memories can be used to this end.
[3] With a purpose analogous to classical logic gates in computing.

Length [mm]	Output Bandwidth [nm]	Selectivity [dB]	Bandwidth compression	Internal conversion efficiency	η_{norm} [$W^{-1}cm^{-2}$]	Ref.
22	0.14	7	6.98	87%	-	[79]
27	0.13	-	7.47	61.5%	2.32	[62]
17	0.1	7.7	9.71	5%	-	[80]
17	0.03	22.9	-	18%	3.32	[81]
27	0.08	-	-	-	-	[82]
15	-	-	-	80%	-	[83]
47	-	-	-	86%	-	[84]
60	-	8.4	-	80%	-	[85]
71	0.03	21.5*	16	18%**	1.07	[86]

Table 4.2: Selection of different results in QFC from literature. Selectivity is given as the extinction ratio in dB. The bandwidth compression has been calculated with an input of 963GHz. Normalized conversion efficiency η_{norm} has been estimated for the processes where the pulse properties were known. The last entry contains results presented later in this thesis and in [86].
*Estimated from experimental results, see discussion in chapter 5. **At maximum available power, see discussion in chapter 5.

and output frequencies, unless a specific GVM condition is needed. From the highlighted works, we can see that conversion efficiencies have already reached the maximum of ∼80% predicted in [87]. Output bandwidths on the other hand are far behind those needed for quantum memories. Most QFC processes have a ∼0.1nm bandwidth which, for the shorter wavelengths is in the tens of GHz range. Narrower bandwidths have been achieved by tightly filtering the TF like in [81]. However, this severely impacts the conversion efficiency of the process and no longer performs better than spectral filtering as a bandwidth compressor.

The reviewed processes have already proved many quantum-inspired measurements and information processing applications. In metrology [81, 88], interfacing quantum memories [62], manipulation of temporal modes [80, 85] and new photon detection schemes [83, 84] have been demonstrated. Improving the devices performance would have a positive impact in their application.

4.4 The challenges for realistic quantum devices

The previous overview of current approaches to different devices and processes for quantum network components sets the playing field for the research carried out in this thesis. The results reviewed provide proof of principle of the basic pieces of the quantum network but further optimisation is required before a full-scale quantum network could be implemented.

One clear choke point is the interfacing of different components. The frequency and bandwidth requirements of memories and sources are currently very different. QFC offer a solution, but bandwidths are not narrow enough for quantum memories yet. Additionally, current QPG performance (its mode selectivity and bandwidth compression) limits the results in applied quantum technologies as it has not reached expected values. It can be shown that both issues are tightly linked to a third problem the integration of these devices.

Many of the processes reviewed are already realised in optical waveguides. From our discussion

in chapter 2, it is clear that the length L of the devices is a critical parameter. Longer non-linear waveguides then, increase the conversion efficiency with $\sin^2(L)$ and narrows the bandwidth of the PM function with $1/L$. In the case of a QPG devices, this increases the selectivity and the bandwidth compression too, an effect that we will discuss in detail in section 5. However, the length of the devices has not increased in the last years. It is apparent that we are reaching a waveguide fabrication technological limit. For example, waveguides in LN are rarely longer than 30mm and, even when longer waveguides have been used, the results show no clear improvement due to length increase. Recent studies [34, 89, 90] show that longer devices are more critically affected by the waveguide inhomogeneities explained in section 2.5. In chapter 5, we will present a detailed analysis of these effects on QFC and on the QPG in particular. The results include an improved QPG device, and a toolbox for tailored QFC design and process characterisation of the processes. With these results, we can address interfacing problems between the quantum devices discussed and clear the path towards realistic quantum network components.

Additionally, QFC processes are designed to be applied to quantum technologies. The QPG single-mode selective process, implementing state projections in single photons is one prone to many implementations. In chapter 6, we present two results in quantum metrology and one in quantum state tomography exploiting the QPG and the TM framework. The experiments show quantum performance with great success and unparalleled results.

Regarding the quantum light sources, we have seen many different platforms that already exhibit good performance. Now is the time to start exploiting the sources for real applications in the quantum network. We want to encode information in the photons and we already know there are many degrees of freedom to do so. A controllable source over one or more of these degrees of freedom producing well defined qubit states is a clear goal. Moreover, expanding the two-dimensional Hilbert space of a qubit to a d-dimensional one in a qudit can have a tremendous impact in quantum information and communication technologies.

A higher dimensional space would provide greater information capacity, improve the security of QKD protocols and the noise resilience [91–93]. Transverse spatial modes of photon states open such a high-dimensional space [94] but lack compatibility with spatially single-mode optical systems, limiting its use in practical applications. In section 3.3.1, we introduced TMs which span a potentially infinite-dimensional Hilbert space in the energy degree of freedom of photons and that are compatible with single-mode optics. In chapter 7, we will present a controllable source of maximally entangled photons in up to 6 dimensions.

Chapter 5

QFC: design and characterization

The strength of QFC lies in its versatility. The processes can be engineered and tailored towards specific applications in photon frequency conversion, quantum measurements, information processing... Each application has different requirements like the phase-matched frequencies or the frequency correlations in the JSA, that have to be tackled with the design of the QFC device. This includes the selection of non-linear material, the engineering of the process with its properties and the design of the waveguide structures.

Unfortunately, while integrating the devices in optical waveguide structures improves their performance, it also complicates the task. The material and fabrication process have to be thoroughly controlled to avoid fabrication inhomogeneities as described in figure 2.8 in section 4.4. Current fabrication technologies set certain limits for what the processes can achieve in the end: phase-matching bandwidth, conversion efficiency, selectivity and TF properties all depend on the quality of the fabricated device.

In the this chapter, we will review the current limits of LN based devices. We will show that the main limitation is the length of the devices, which caps the performance. With a detailed comparison of simulations and measured results, we will asses the sources of discrepancy and how to correct them. This will lead to the fabrication of a longer QPG device that improves its performance in every benchmark analysed (namely: PM function bandwidth, bandwidth compression, conversion efficiency and selectivity). Additionally, in the last section, we will present QFC general design guidelines to interface different quantum devices, using quantum dots as an example.

5.1 Study of inhomogeneities on QPG devices

We can asses the state of current technology by simulating the processes used in the QPG devices reviewed in section 4.3. In particular, we simulate their PM function and estimate their PM function bandwidth, conversion efficiency and selectivity when possible using the parameters provided in each publication. The results of these simulations and the experimental results are compared in figure 5.1 a).

From figure 5.1 a), it is clear that the current devices are far from the predicted behaviour. Bandwidths are far wider than predicted and the extinction ratio much lower than expected. The only exception is [81], where the resulting TF was tightly filtered to reduce the FWHM and increase the extinction ratio to expected values. This severely reduces the conversion efficiency of the process,

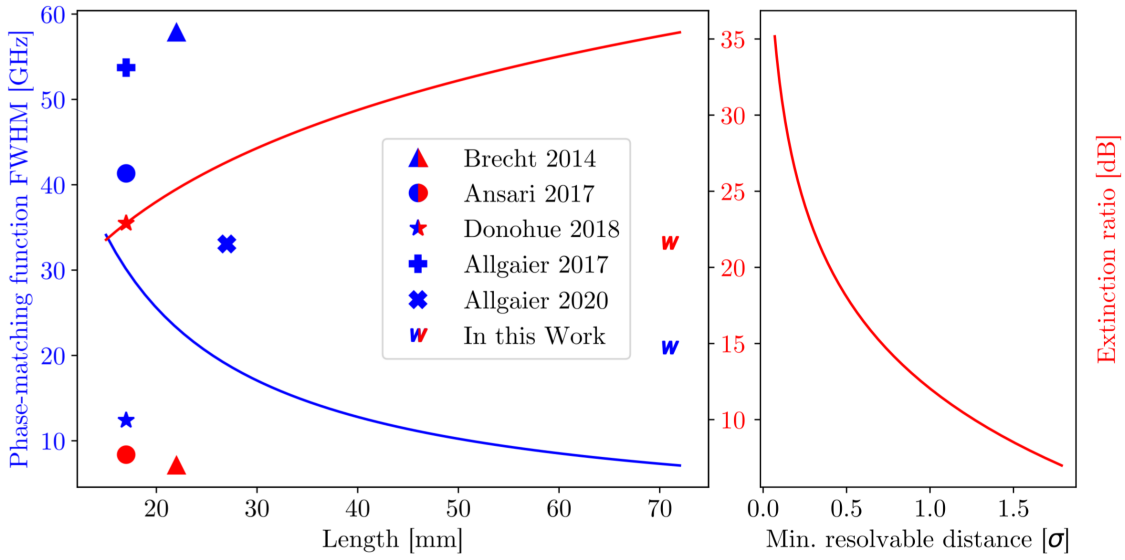

Figure 5.1: a) Expected PM function FWHM (blue) and extinction ratio (red) for the length of the QPG device. The reviewed articles and the results presented in this thesis are shown for comparison. b) Minimum resolvable distance in pulse σ width of two signal pulses when using the QPG for a quantum metrology measurement as in [81, 88, 95]; see the main text and section 6.2 for details. Figure from [86].

which is of utmost importance for final single-photon state manipulation. Ultimately, the bandwidth limitation impacts the final extinction ratio and bandwidth compression.

The widening of the bandwidth is often the result of a varying PM condition along the waveguide as described in section 2.5. As discussed in [89], this is a result of waveguide inhomogeneities, e.g. imperfect waveguide fabrication or non-ideal operating conditions. Moreover, these inhomogeneities become more relevant the longer the sample. To quantify this behaviour, reference [89] introduced the concept of critical length of a device, i.e. the maximum length of a device, such that the overall process efficiency is still greater than 50%. Therefore, this critical length sets a limit at which inhomogeneities in the waveguide severely reduce the performance of the device. To overcome it, the fabrication process has to produce waveguide as homogeneously as possible.

Hence, increasing the length of the devices necessarily needs an improved fabrication process which is very challenging. However, the benefits from increasing the length are worth the effort. Narrowing the PM function bandwidth down to a few GHz allows the interfacing of many memories discussed in section 4.2 (like QDs, atomic ensembles Cs memories) through bandwidth compression. Longer devices would also notably increase the extinction ratio of QPG devices which enhances many QPG applications, like when using the QPG to estimated the distance between two very close pulses in a quantum metrology technique as seen in figure 5.1 b). The minimum resolvable distance between the pulses decreases with the extinction ratio, improving the resolution of the technique. This quantum metrology technique will be introduced in detail in section 6.2.

5.1.1 Revised LN fabrication process

Inhomogeneities can be caused by any effect deviating the waveguide from ideal parameters: errors and inconsistent waveguide width and depth through the length of the device, impurities in the titanium or gradients during the diffusion process, but also uneven temperature distribution of the device when in use. These cause the $\Delta\beta$ variation along the waveguide and lead to reduced performance (conversion efficiency, selectivity, bandwidth compression).

To increase the length of the QPG device, we first focused on characterising samples with different fabrication parameters to identify the major sources of error. With this information, it was possible to improve the waveguide fabrication process. This included minimising any source of error from the parameters and components in every step of the process as described in figure 2.6 and in the poling process. A new photolithography mask with more uniform poling patterns and waveguide structures was produced in order to minimise poling errors due to uneven current densities during electric field poling. The use of a pristine titanium batch was ensured for each

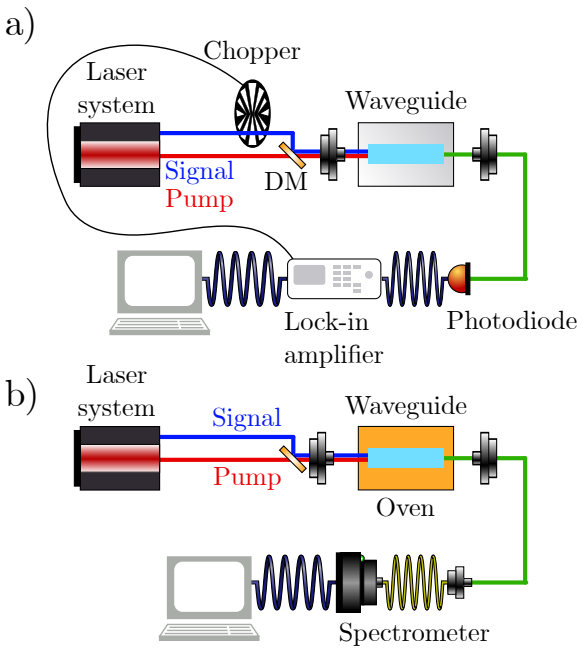

Figure 5.2: a) Experimental setup to measure the PM function of the sample at room temperature. The signal is a tunable Tunics CW laser. The pump source is a Ti:sap CW laser. Both are coupled into the sample and the ∼550nm output intensity is measured with a photodiode. An lock-in amplifier is used in combination with a chopper to remove DC noise from the signal. The converted light is measured with a photodiode and the data is stored in a computer for its analysis. b) Experimental setup to measure the PM of the sample at 200°C. For the 2D PM function measurement, the signal comes from a tunable CW laser and the pump is a 200fs pulse from a pulsed Ti:sap. For the 1D PM function measurement, the signal is pulsed and comes from an OPO system pumped with the pulsed Ti:sap. The fields are coupled into the waveguide and the generated field is measured on a fiber-coupled spectrometer. Figure from [86]

titanium strip deposition and the uv-lamp was carefully adjusted for more homogeneous illumination of the photolithography mask. Several QPG devices were produced, with varying poling charge, to test its effect on the poling patterns. The best results were found for the sample that had been poled with double the electrical charge required for domain inversion. After these modifications, we manufactured ∼70mm long QPG devices and characterised them. We analyze the results of this characterization in the next section.

5.2 Improved QPG device

To quantify the improvements in the device performance from the enhanced fabrication process, we characterized a 71mm long QPG device. The device non-linear process is first characterised at room temperature to first asses if the process works as intended. Next, the non-linear response is measured at the final experimental temperature, around 200°C . The QPG is operated at such high temperature to avoid the effects of photorefraction from the high-intensity pump field. The experimental setups used to characterise the sample are described in figure 5.2.

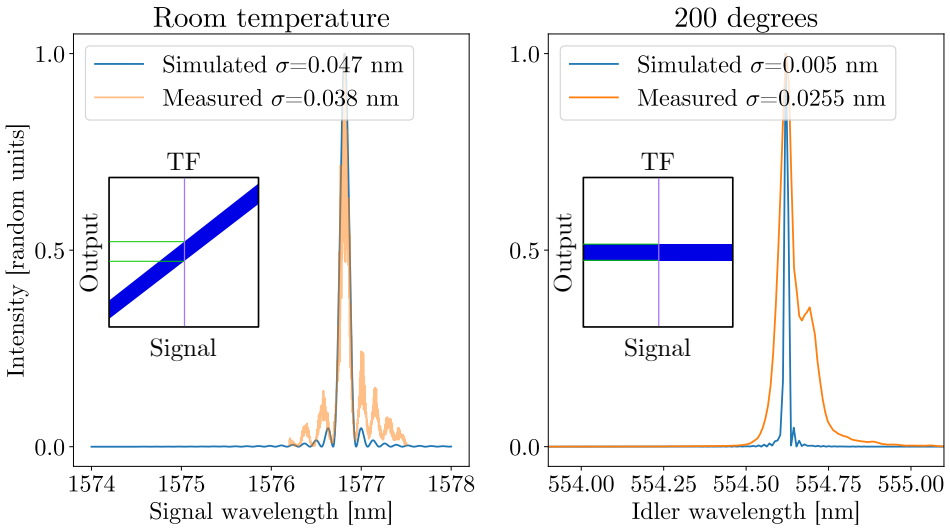

Figure 5.3: Simulated and measured PM function of the sample at room temperature (∼21°C) and at 200°C . At 200°C the simulation was performed with the spectrometer's resolution of 30pm. The $1/e$ bandwidth (σ) of each spectra is annotated in the legend in wavelength and frequency units. The insets show a simplified sketch of the TF of the process at the different temperatures. At 200°C , signal and pump are in GVM (as discussed in section 2.3) and the TF angle is flat, narrowing the output bandwidth. Figure adapted from [86].

For the non-linear characterization at room temperature, the signal and pump fields are coupled into the waveguide. The signal wavelength is scanned from 1574 to 1578nm with a fixed pump at 875nm. The intensity of the generated SFG field is then recorded at each signal wavelength. The result is shown on the left plot in 5.3. The measured PM function exhibits a bandwidth of σ =0.47nm, very close to the expected one. The measured spectrum is slightly narrower than

the theoretical one due to the presence of the interference fringes caused by the measurement technique [96]. The overall symmetry and side lobes don't fit. This indicates the presence of some lesser inhomogeneities in the waveguide. Altogether, this is an outstanding result for such a long waveguide, as the expected critical length for the process, characterised in [89], is below 20mm.

With the sample performing close to expected at room temperature, the PM function is then characterised at 200°C on the experimental setup depicted in figure 5.2b). In this setup, the sample is heated up to 200°C inside a copper oven. The oven is kept at constant temperature with a heating cartridge controlled on a feedback loop by a temperature controller (Oxford instruments Mercury iTC). First, to measure the 2D PM function, phase-matched frequencies from a CW signal and a pulsed 200fs pump are scanned to generate the data in figure 5.4. To measure the 1D slice of the PM function at the desired operation wavelengths depicted on the right in figure 5.3, ultrafast pulses are used for both signal and pump fields, with a duration of 200fs. In both cases, the output field of the process is directly measured on a spectrometer (Andor Newton EMCCD, 2400 lines per mm grating, resolution ≈0.03nm). The spectrometer resolution is not enough to resolve the features of the expected PM function, which would require a resolution below 5pm.

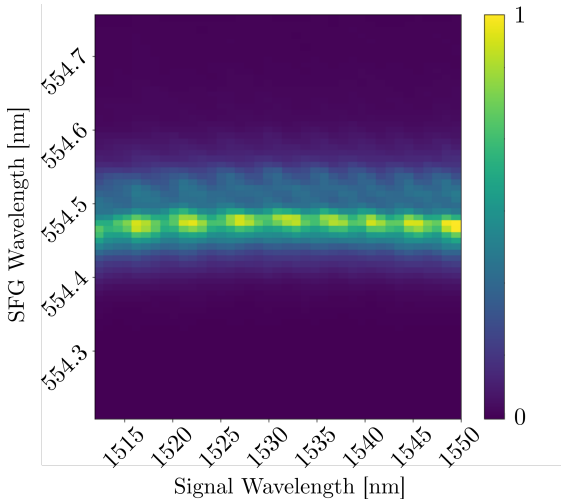

Figure 5.4: 2D PM function of the QPG process measured at 200°C . The intensity beating seen is an artifact of the experimental measurement. Figure from [86]

The 1D PM function at 200°C shows a narrow, slightly asymmetric spectrum, close to the expected one. The 1/e bandwidth of the measured SFG field, corrected for the resolution of the spectrometer, is σ =0.0215nm while the expected value is σ =0.005nm. The side lobes present at room temperature have disappeared and the main peak displays an asymmetry that will impact the performance of the QPG. We see that, compared to room temperature operation, the PM has broadened. Nevertheless, the bandwidth is still much narrower than any previous results thanks to the increased length and quality of the waveguide. The PM function bandwidth achieved with the improved QPG enhances the performance of the QPG in the discussed benchmarks: bandwidth compression, extinction ratio and conversion efficiency.

Thanks to the narrower PM function, the bandwidth compression ratio increases to 16, almost

doubling the best result[1] reviewed in table 4.3. Furthermore, from the width of the PM function we estimate an extinction ratio of 21.5dB, as highlighted in figure 5.1 in comparison with other QPG devices. When using the QPG to estimate the separation of incoherent signals in the time-frequency domain (as discussed later in section 6.2), this extinction ratio allows to estimate signals as close as 0.5σ. Finally, if the asymmetry in the PM function at 200°C is addressed, the expected extinction ratio would be 35dB.

The internal conversion efficiency is measured by recording the depletion of the signal power through the device for different pump powers. With the maximum available power, 4mW CW equivalent power, the conversion efficiency is 18%. The normalised conversion efficiency, calculated from equation 2.2.11, is $1.15\text{W}^{-1}\text{cm}^{-2}$. With respect to previous results [62], we measure much higher internal conversion efficiency, even with lower η_{norm}. Therefore, the reduction of η_{norm} due to fabrication imperfection is more than compensated by a fourfold increase in the interaction length. The enhancement is evident when one calculates the conversion efficiencies from equation 2.2.11 for the η_{norm} of the reviewed experiments in table 4.3, the length increase allows to reach unit efficiency at much lower pump powers than previous shorter samples. This can be seen in figure 5.5.

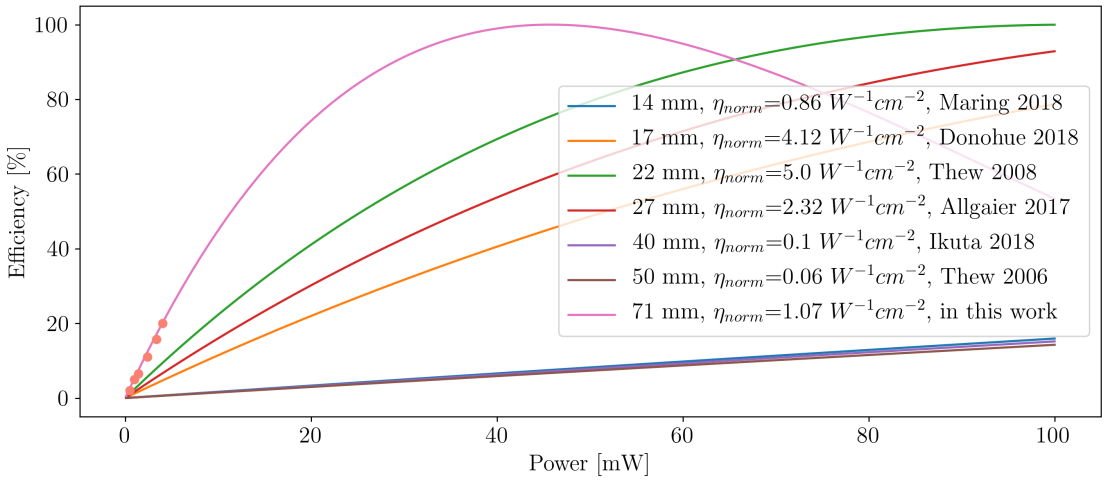

Figure 5.5: Comparison between the conversion efficiencies calculated from the η_{norm} in [62, 81] and in this chapter with equation 2.2.11. The pink dots mark the values measured experimentally. Figure from [86]

5.2.1 Analysis of the waveguide inhomogeneities

The PM function at room temperature showed a nearly ideal main peak. However, we observe some imperfections in the PM function at 200°C , namely slightly wider bandwidth and a secondary peak. A natural question is whether the spectrum at 200°C is consistent with the one at room temperature. To this aim, one can estimate the inhomogeneities at room temperature and see if they fit at high

[1] To the knowledge of the author.

temperature. To do this, it is necessary to retrieve the $\Delta\beta$ variation along the waveguide at room temperature and use it to simulate what should happen at 200°C .

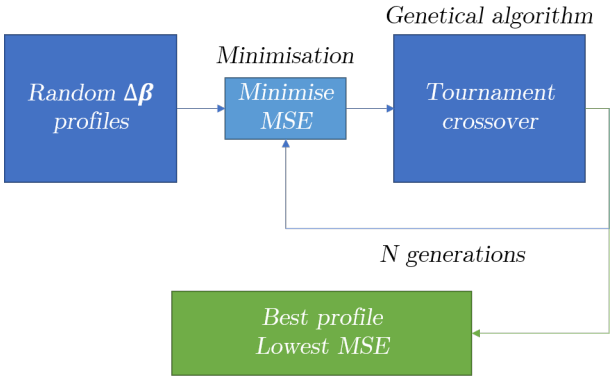

Figure 5.6: Flowchart of the optimisation algorithm. Figure from [86]

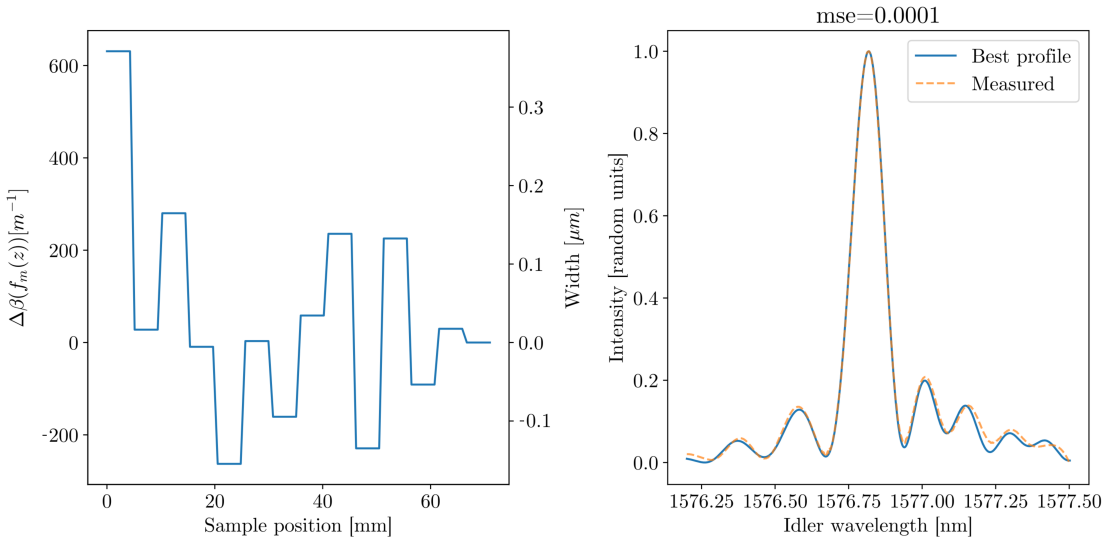

Figure 5.7: The resulting $\Delta\beta(f_m(z))$ profile after running the genetic algorithm is on the left. The y axis on the right are the equivalent waveguide width deviation for the profile. The best profile's PM function is plotted against the measured one at room temperature on the right. The MSE is 0.0001. Figure from [86]

Although it is possible to measure the profile of waveguide inhomogeneities, the required experimental setups are generally very complicated [97]. This method requires its own dedicated experimental setup and a Frequency Resolved Optical Gating (FROG) system to reconstruct the $\Delta\beta$ profile of the structure.

A different approach is to obtain the $\Delta\beta$ profile directly from the PM function measurement. To do this, we describe the phase-mismatch profile as a function of the propagation axis z, dividing the waveguide into m sections with constant $\Delta\beta$ given by $f_m(z)$: $\Delta\beta(f_m(z))$. Then, by tuning the $\Delta\beta$ value of each section of the profile, we can find the profile that generates the best fit to the measured PM function.

To find the best $f_m(z)$ for each section we use a genetic algorithm combined with a minimisation routine. We look for the profile that results in a PM function that minimises the mean square error (MSE) between the simulated and the measured room temperature PM spectra. The algorithm uses the MSE between the PM functions produced by randomly generated $\Delta\beta(f_m(z))$ profiles and the measured PM as a fitting function. Each profile's MSE is first minimised using the Broyden-Fletcher-Goldfarb-Shanno algorithm and then some low MSE profiles are selected with a tournament selection rule [98]. The selected profiles are crossed over, generating new profiles by adding together a section of each selected profile. This process is repeated for a number of generations to reduce the MSE of the best profile. A flowchart describing the algorithm is shown in figure 5.6.

We divide the waveguide in 14 sections chosen so that each section of the profile is smaller than the critical length for this process. This might cause oversampling of the problem and produce a non-unique solution. Nonetheless, the profile still reproduces the PM function and is nevertheless instructive. We run our algorithm for a 100 generations with a population size of 100 profiles. The tournament has 4 participants. This took around 10 hours of computing time on 16 Gb of RAM.

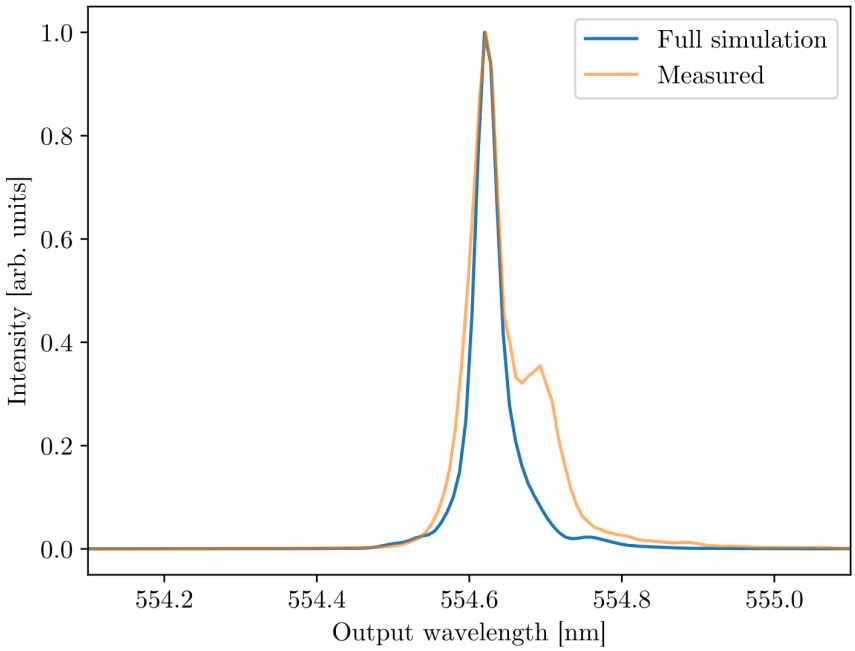

Figure 5.8: The simulated PM function fits the main feature of the measured one. Figure from [86]

The best profile and resulting PM spectrum can be seen in figure 5.7.

The algorithm produces a very good match with the measured PM with a resulting MSE of 0.0001. This profile is characterised by the presence of significant inhomogeneities, despite the measured spectrum being very close to the ideal one. These results show that this is a useful tool to estimate inhomogeneities in waveguides and gain a better knowledge of the fabrication process. The algorithm gave a similar result for a different poled waveguide within the same sample with a resulting MSE of 0.0001 too.

Now that the profile at room temperature is known, we can simulate the PM function at 200 degrees combining the width profile and the change of $\Delta\beta$ at 200°C , considering a constant temperature over the whole waveguide. The result is shown in figure 5.8.

This full simulation of width and temperature matches the main peak on the measured PM function. The simulated bandwidth is very close to the measured one. The widening of the PM function is now explained by fabrication inhomogeneities and temperature effects. The peak on the right side is left unexplained, meaning that the model is still incomplete. It might be caused by temperature inhomogeneities on the sample and we study it on the next section.

Overall, considering the bandwidth of the PM spectrum at 200°C , this QPG device has a bandwidth compression of 16, doubling on previous results. The internal conversion efficiency of 20% at 4mW pump power outperforms the current state of the art thanks to a fourfold increase in the sample length. Finally, the device is estimated to reach extinction ratios around 21.5dB by just filtering the asymmetry on the right side. Furthermore, if the asymmetry is addressed, a measurement with higher resolving power could reveal an ideal PM function with 35dB extinction ratio or serve to further improve the fabrication process.

5.2.2 Temperature inhomogeneities

The $\Delta\beta(z)$ profile resulting from the analysis in the previous section doesn't fully explain the measured PM function in figure 5.8. Another possible source of inhomogeneities is the temperature distribution over the sample on the oven. In order to determine whether or not the sample heating was in fact the missing piece, we decided to measure the temperature profile and include it in the modeling.

The temperature distribution over the waveguide is measured with an IR camera. The picture and the temperature distribution the sample length can be seen in figure 5.9. The temperature is not homogeneously distributed through the device. To ascertain if this inhomogeneous temperature profile is the cause of the asymmetry in figure 5.8, we combine the $\Delta\beta(z)$ profile obtained from the minimisation routine in figure 5.7 and the resulting profile from the temperature distribution. The resulting $\Delta\beta$ profile is shown in figure 5.10a). With this profile we obtain a new PM function to describe the experimental result, displayed in 5.10b).

The new simulated PM function exhibits the same features of the measured one, with the side peak. The bandwidth is slightly increased and central frequency has been shifted probably due to the calibration of the IR image processing. The small differences could also be caused by the interplay of the temperature distribution sampling and the non-unique profile produced by the oversampled simulation in the previous section. Taking the temperature profile from the IR picture was not straightforward, as there are no hints to where does the sample really start so background temperature might have been taken into account or a small section of the sample was left out. The IR camera was calibrated taking the temperature of the copper oven as a reference with the emissivity of oxidized copper but the exact value might be off.

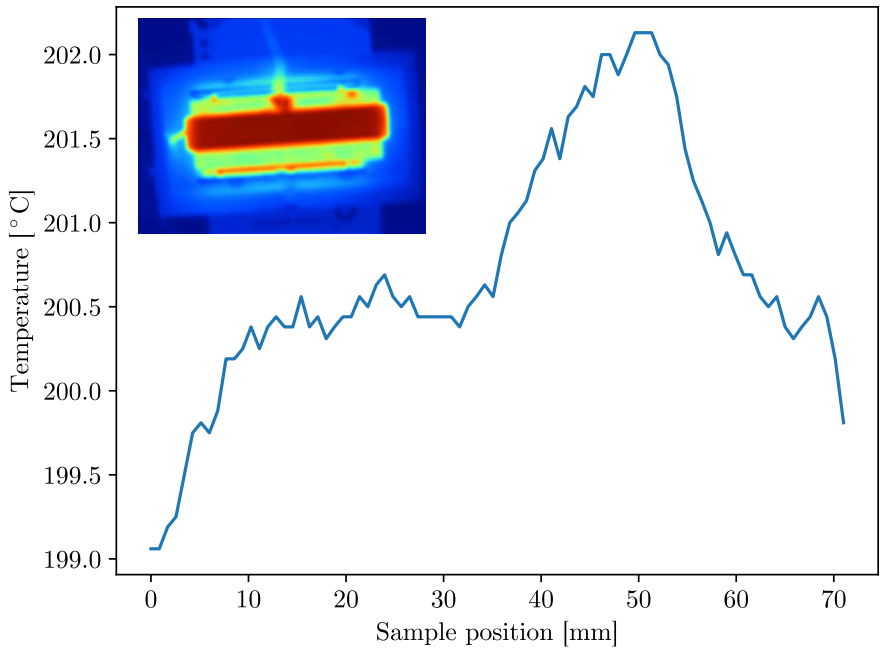

Figure 5.9: Temperature distribution over the QPG sample characterised in section 5.2. The inset shows the original IR picture.

We can conclude that the inhomogeneous temperature distribution is a major component of the source of the side-peak problem. A better heating system is needed with a more homogeneous distribution of heat. One option is to substitute the cartridge heater for a 'surface' heater. These devices are usually some form of material slab with a conductor coil inside covering most of the surface. This way the heat produced from heating up the conductor is more homogeneously distributed. The isolation of the sample and oven also play an important role. The better the isolation, the least heat is lost to the environment, reducing the amount of power needed to heat up the oven to the desired temperature and stabilising the feedback heating loop thanks to a reduction in the temperature drifts. Currently, the QPG and oven sit inside a Teflon box covered in turn by an exterior box of fireproof material that has a high heat conductivity. The exterior box could be substituted by Teflon as well and covered in some highly isolating material, like a ceramic compound.

Alternatively, one can take advantage of the impact an inhomogeneous temperature distribution has on the process. Instead of improving the heating system to ensure a homogeneous temperature distribution, one can purposely apply an inhomogeneous temperature distribution that balances the width inhomogenities and results in a final constant $\Delta\beta(z)$ profile. This can be done by using a segmented oven in which the temperature of each part of the oven can be controlled individually as discussed in [99] and [34].

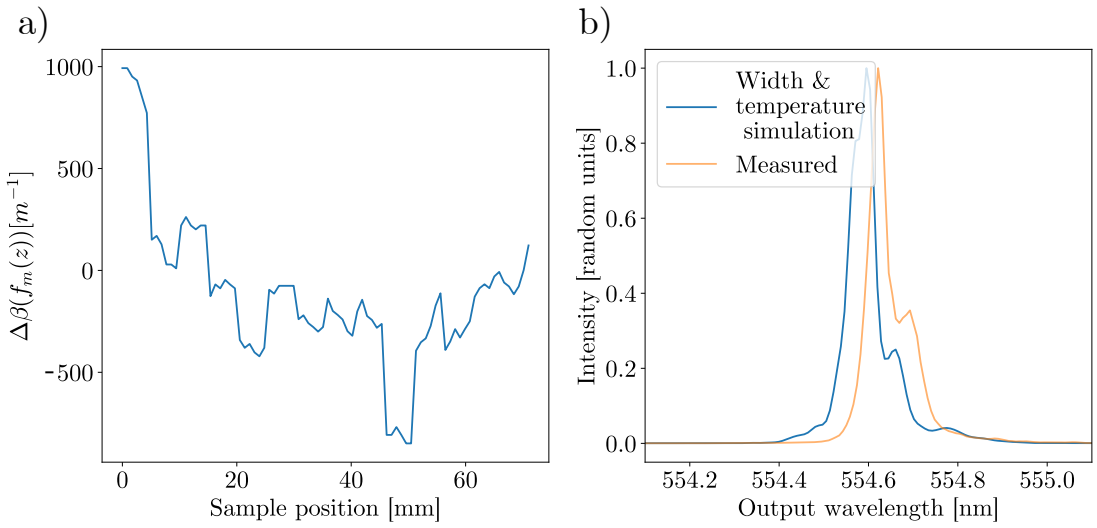

Figure 5.10: a) $\Delta\beta(z)$ profile resulting from combining the width profile resulting from the optimization routine in section 5.2.1 and the temperature profile measured with the IR camera. b) Resulting PM function from a simulation with the profile in a).

5.3 QFC design

Interfacing different devices and components of quantum networks requires frequency conversion between the working central frequencies and spectral bandwidths of both interfaced devices. Furthermore, particular spectral correlations might be needed for the final state or preserved from the original state. This means that the QFC process must be designed not only with the required frequencies in mind but with a TF engineered in a particular shape. Hence, the QFC process has to be balanced as a trade-off between the constraints set by the chosen platform for the device (phase-matched processes, polarization, waveguides, GVM...) and the performance of the conversion process. From section equation 2.3.6, the TF is the product of the PM function of the process and the spectral envelope of the pump. These two contain the design restrictions that must be juggled.

The PM function and its angle limit the available processes and frequencies available for conversion, and the possible resulting TF. It is ultimately limited by the materials and waveguide structures available. The pump field sets the final TF and defines the transfer function between the input and output fields. The laser sources (pulsed or CW) accessible and spectral shaping techniques allow further engineering of the final TF. In the end, these constraints must be balanced to convert the desired pair of frequencies, with the needed spectral correlations while keeping the conversion efficiency as high as possible.

For instance, the QPG can be used to interface an IR state with a device working in the visible. The transfer function of the QPG grants the user bandwidth compression to interface a device with narrower spectral bandwidth. However, the flat uncorrelated transfer function will carry no spectral information from the original state over to the up-converted field. This is a problem if we were trying

to measure these properties in the up-converted regime. On the other hand, the pulsed operation of the QPG provides higher conversion efficiency than a CW operated device. In conclusion, one could design a QPG to interface, for example, an IR photon source with a diamond quantum memory (even a Cs memory with enough bandwidth compression) but not to carry spectral correlations of a engineered photon source in the IR to the visible.

5.3.1 Interfacing a quantum dot with a streak camera

There are a wide variety of processes that will need interfacing in real world quantum networks, as we reviewed in section 4. In this work, we focused on interfacing a QD (produced in the group of Prof. Dr. Manfred Bayer in Dortmund) with a streak camera. Streak cameras measure intensity variations with time and are often used to characterise the temporal envelope of pulses. They are an important tool for characterising quantum dot emission. Unfortunately, they often have very low quantum efficiencies or are blind at the emission bands of the sources. Therefore, the two require a dedicated interface. We designed and produced an SFG device to frequency up-convert the QD single photons from the IR to allow detection by the streak camera in the visible range.

The aim is to convert the QD emitted photons at 1150nm up to the visible (~ 680), where the streak camera not only can detect them but has highest quantum efficiency (Hamamatsu C5680-25, $\sim$8%). It is key then to have the highest possible conversion efficiency to not waste photons while designing a process that maintains the spectral properties of the original signal. This is paramount to the proper characterization of the quantum dot emission, if the temporal width of the converted field is not known in relation to the original signal, then the measurement on the streak camera will contain no information about the original quantum dot field.

To maintain the temporal width of the quantum dot emission, the angle of the JSA must be known and ideally 45°, as it means a 1:1 ratio between the input and output temporal (and spectral width). In this case, the CW pump presents an advantage. As long as the PM function is wider than the signal input, any CW pump will result in a TF at 45° and maintain the temporal width.

With all the constraints in mind, an SFG Type II process in 7µm Ti:LN waveguides with poling period 7µm is designed to convert the quantum dot emission at 1150nm to 686nm with a pump at 1700nm. This was the only possible process for this frequencies combination in Ti:LN waveguides. The PM and TFs of the process are shown in figure 5.11.

Access to a pulsed pump would increase the efficiency due to the higher peak intensities. However, in that case, the width of the pump pulses must be taken into account when designing the process so that the angle of the JSA is known. For example, a pump as broad as the PM function would lead to an uncorrelated JSA. In that case, the output will always have the same spectral bandwidth, no matter the original signal bandwidth. Other materials and platforms might allow different more efficient processes thanks to their higher non-linear coefficients. For instance, type II SFG in LN is the lowest coefficient and type 0 its highest, but no type 0 processes in LN match the central frequencies needed to interface the QFC process under investigation. Finding a different material with an available process with higher coefficient would increase the efficiency.

5.3.2 Design guidelines

The design of QFC devices is then constrained by the technologies available and the target properties. Therefore, there is no straightforward design procedure. For the process designed in the previous section, the highest priority properties were phase-matching the quantum dot emission with

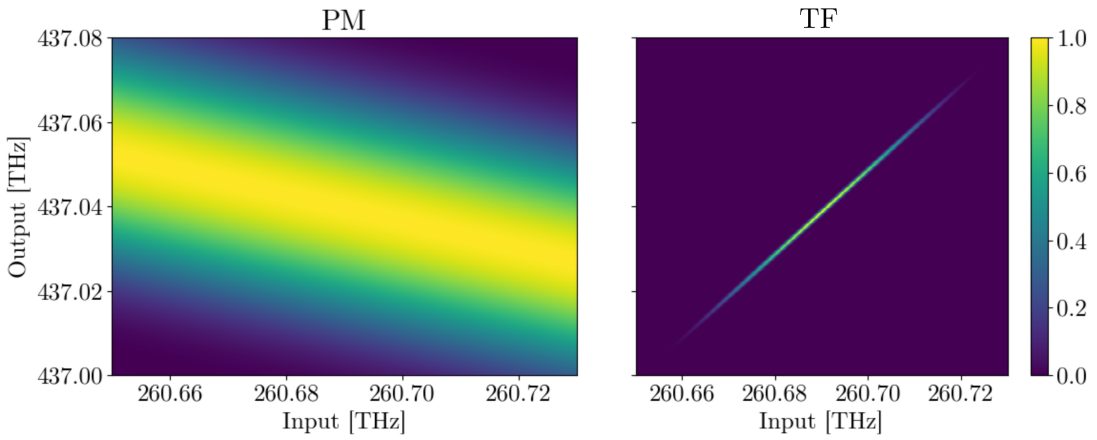

Figure 5.11: PM and TFs of the SFG type II process to interface quantum dot emission at 1150nm with an streak camera at 686nm.

the streak camera highest efficiency frequency range and the correlated TF. Conversion efficiency was sacrificed by the use of a CW laser and the type II process to achieve a correlated TF at the correct phase-matched frequencies. Hence, as a general rule, one must identify the key properties needed out of the QFC and design the process from there. Summarizing the previous discussion, we can outline two general guidelines regarding the interface priorities on spectral properties and conversion efficiency:

- **Spectral properties:** A PM function bandwidth wider than the pump bandwidth allows us to design TF that preserve the spectral properties of the input. In that case, the best option is the use of a CW pump to ensure a 45° TF angle. On the contrary, if the application calls for a manipulation of the spectral properties then the bandwidth ratio between the pump field and PM function angle has to be engineered to such need. This includes using pulses with tailored bandwidth for the pump field and choosing the correct material for the group velocities of the fields to engineer the correct angle. For example, bandwidth compression can be implemented with a 0° PM function and wide pump, like the GVM SFG process of the QPG, which needs very particular GVM properties from the material.
- **Conversion efficiency:** If truly only the frequencies must be converted, and everything else can be ignored, then one should choose the material and process with the highest non-linear coefficient available. Furthermore, the use of GVM pulses would give the highest efficiencies, as in that case the fields travel together and the interaction length matches the length of the device. However, this is rarely the case. In most scenarios, the final process is designed as a trade-off between the spectral properties and the maximum conversion efficiency possible. The use of pulses whenever possible will help increase it.

This guidelines are not absolute and, in the end, every property of the desired QFC process have to be considered. The key is to identify the most important conversion (like central frequencies, bandwidths or spectral correlations) that the device must perform, and engineer the rest around it.

Chapter 6

The QPG at work

The TM selective operation of the QPG opens the door to many applications in quantum information. Basically, with a QPG one can read the TM composition of a photon state and process the information contained in it. This can range from the "simple" tomography and reconstruction of a quantum state [80] to photonic quantum gates for quantum computing [100].

In this chapter, we discuss two applications in three experiments with the QPG and we present experimental results that prove the viability of these applications. We start with a description of the experimental setup used to exploit the QPG and then the three experiments follow. First, the QPG is used to estimate temporal separation between two incoherent signals beyond the classical limit applying concepts derived from quantum metrology. We will show the method and experimental results that expand the technique to estimate more than the pulses separation. The effect of different degrees of coherence between the analyzed signals is also experimentally investigated. Second, we implement a novel compressive sensing method to reconstruct unknown photon states with the QPG. The principles behind the method are introduced and the experimental results are presented.

6.1 QPG experimental setup

To successfully implement the QPG we need the following key components: pulsed pump and signal fields, spectral shaping of the pump to control the projecting mode ζ of the QPG and signal to simulate interesting input states, spectral filtering of the output up-converted field from the QPG process and a photon detector. A setup containing these, is able to carry out many different experiments exploiting projection operations with very little change, proof of the versatility of the QPG.

The experimental setup used in every demonstration in this chapter is illustrated in figure 6.1. The signal (around 1550nm) and pump (around 860nm)[1] pulses come from a tunable ultrafast laser source consisting of an optical parametric oscillator (Coherent Chameleon OPO) pumped with an ultrafast Ti:Sap laser with 80MHz repetition rate (Coherent Ti:Sap). The ultrafast pulses have a FWHM of 200fs in time. The system allows to tune the central frequency of both fields in the IR and near-IR ranges.

The signal pulses are spectrally shaped into different input TMs for the QPG using a commercial

[1] The exact wavelengths depend on each specific experiment.

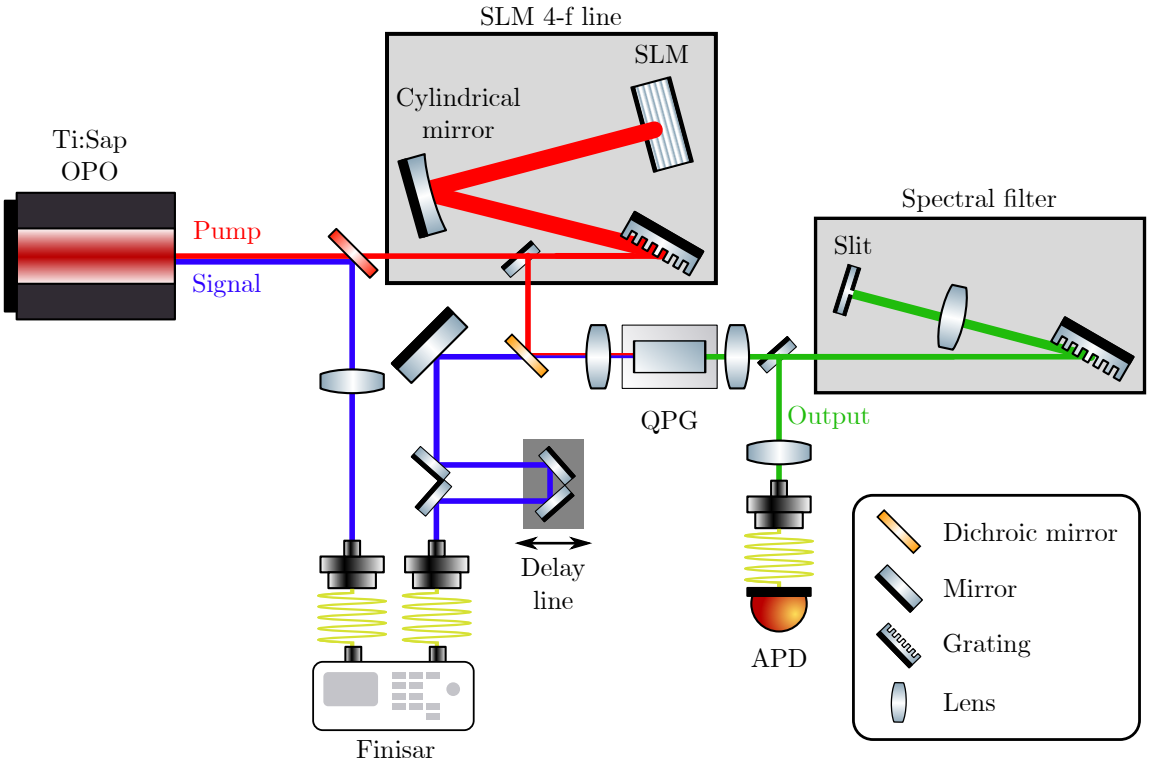

Figure 6.1: QPG experimental setup. See the main text for a detailed description of components and working flow.

spectral shaper (Finisar Waveshaper) with a shaping resolution of ~ 0.1nm. The signal propagates then through a delay line that allows one to match the arrival time of the pulses with the pump pulses at the QPG. The pump pulses spectral shaping is carried out with an in-house build spectral shaping setup using a spatial light modulator (Hamamatsu LCOS-SLM). The working principle of the SLM and the setup are explained in the following section. The setup has a shaping resolution of ~ 0.03nm. After shaping, the pump is coupled together with the signal into the QPG waveguide for the process. A 7mm focal length lens is used to match the spatial distribution of the 2mm Gaussian width fields to the $\sim$4µm mode size of the QPG waveguides. At the output, another 7mm lens is used to collimate the up-converted QPG light. This lens has an anti-reflective coating for the QPG output range to reduce losses.

The QPG is placed on a copper oven heat to 200°C using a heating cartridge. The temperature is measured with a PTC1000 temperature sensor. A temperature controller (Oxford instruments) is used in a feedback loop to maintaining the temperature of the oven stable down to variations of 0.01°C . To further stabilize the temperature, the QPG and oven are placed inside a Teflon cage with openings for the laser fields to be in-coupled and out-coupled through the lenses.

The up-converted output light in the green visible range is sent to a custom spectral filter built with the same geometry as the SLM setup. This filter consists of a grating with 2400 lines/mm, a lense with 50cm focal length and a slit with tunable width in front of a silver mirror. Closing

the slit allows us to filter the side lobes of the QPG PM function to clean the TF. The spectral resolution of the filter is ~ 0.04nm. The filtered output is finally coupled to an avalanche photon detector (APD; ID Quantique) which, in combination with a time tagger (Swabian instruments), is used to measure the average photon number in the output QPG mode.

6.1.1 Spatial light modulators for spectral shaping

Amplitude and phase modulation of a pulsed field can be achieved with a spatial light modulator (SLM). This modulation, often called spectral shaping, can be used to shape the pump envelope of the a non-linear process, tailoring the TF. In this work, a liquid crystal complementary metal oxide semiconductor (LC-CMOS) SLM is used. The liquid crystal contains elliptic molecules arranged in a 2D matrix forming the screen of the SLM. The metal oxide semiconductor interfaces the liquid crystal molecules with individual pixels in the circuitry of the device that can apply a different voltage to each individual molecule. The molecules respond by rotating their optical axis, thus components of the field travel through different optical paths within the molecules and their phase is modified. The sketch in figure 6.2 describes the main components of an LC-CMOS SLM. This operation is known as phase-only SLM. The SLM can be programmed with masks defined by a matrix that matches the pixel dimensions of the screen and contains the phase desired for each of them. The amplitude of the fields can then be manipulated through the modulation of the phase-mask programmed on the SLM by setting up a phase-grating.

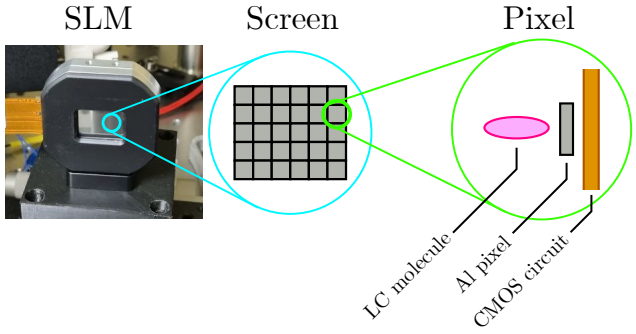

Figure 6.2: Sketch of a reflective LC-CMOS SLM. The screen is composed of many pixel units. Each pixel is composed of the LC molecules addressed by aluminum pixels whose voltage is controlled by the CMOS circuit. The voltage set to each pixel rotates the molecules, changing the phase of light travelling through the molecules and reflecting back on the aluminium surface.

Such an SLM can be directly used for spatial mode shaping within a simple imaging system. In order to perform spectral shaping to tailor the JSA function, we need access to the spectral components of the pulse. This can be accomplished through the inclusion of the SLM in the Fourier plane of a so called a 4-f line setup. A 4-f line is built with two identical gratings and two identical lenses, placed such that the distance between all four elements is equal to the focal distance of the lenses, giving it its name. An example of a 4-f line is represented in figure 6.3.

An input Gaussian pulse (in space and time-frequency domains) is diffracted by the first grating, diffracting each spectral component of the pulse at slightly different angles. Then, the first lens images the spectral components onto the Fourier plane, exactly at a distance f from the lens. In

the Fourier plane, the lens performs a Fourier transform of the spectral components [101], mapping the spatial coordinate of each component into the frequency domain and granting access to its properties. By placing an SLM at the Fourier plane, it is possible to modify the spectral phase of the individual frequency components of the pulse. The second lens and grating reverse the spectral decomposition process, returning all the frequency components back to the original spatial mode. This technique was first proposed by Danailov et al. in 1989 [102]. An extensive review of this and many other pulse shaping techniques is found in Monmayrant et al. [103].

The performance of the 4-f line is determined by the characteristics of the components with the 4-f design parameter

$$\alpha = \frac{\lambda_0^2 \mathrm{f}}{2\pi c d \cos(\theta_d)}, \tag{6.1.1}$$

where λ_0 is the central wavelength of the input pulse, f is the focal distance of the lenses, d is the grating spacing parameter and $\cos(\theta_d)$ is the diffracted angle on the gratings. With α we can calculate the spectral shaping resolution of the setup

$$\delta\omega = \Delta x_0 / \alpha, \tag{6.1.2}$$

with Δx_0 the size of the spectral components on the Fourier plane, given by standard Gaussian beam propagation:

$$\Delta x_0 = 2\ln(2) \frac{\cos(\theta_i)}{\cos(\theta_d)} \frac{\mathrm{f}\lambda_0}{\pi \Delta x_{\mathrm{in}}}, \tag{6.1.3}$$

where θ_i is the incidence angle on the gratings and Δx_{in} is the input beam Gaussian width.

In order to achieve amplitude and phase modulation, we generate grating masks for the SLM using the phase-only modulation of the SLM to simulate an optical grating. The amplitude of the grating over the mask manipulates the diffracted light spectral amplitude. The phase relation

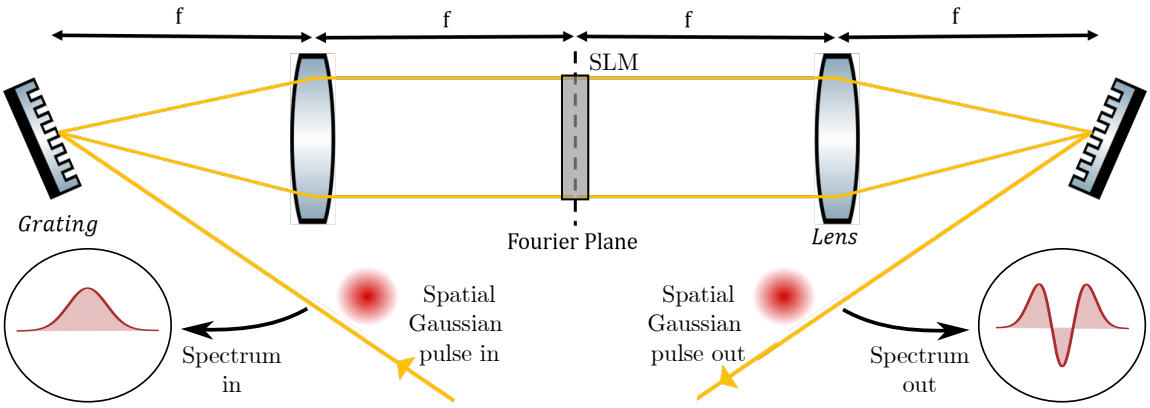

Figure 6.3: Scheme of a 4-f line setup. The position of the two gratings and lenses matches the focal distance of the lenses. The spatial distribution of the input and output pulses is identical, the setup only modifies the spectral distribution of the pulse as depicted in the insets for the input and output spectrum.

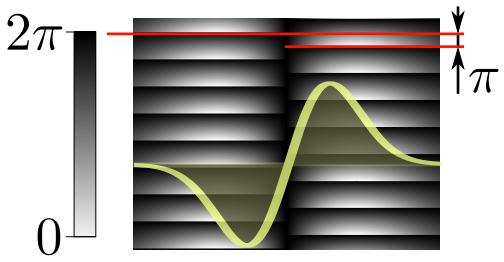

Figure 6.4: Example of an SLM mask to shape a second order HG mode in amplitude and phase. The gray-scale of the mask translate into different phases on the SLM pixels. The expected resulting spectral amplitude of the diffracted light is overimposed on the mask. The red lines guide the eye to the π phase-offset between the two sides of the mask that manipulates the spectral phase between the spectral components diffracted by the mask.

between different parts of the grating allows to introduce phase differences between the spectral components. To illustrate this, a mask to shape a second order HG function is shown in figure 6.4.

The 4-f line setup used for the QPG experiments is shown in figure 6.1. The input pump beam spatial mode is expanded to a Gaussian width of ∼1cm using a telescope (not in the figure). Due to the reflective nature of the SLM used, in the experimental setup in figure a folded 4-f line geometry is adopted. Instead of a lens, a cylindrical mirror with 23cm focal length is used. The shaped spectrum is reflected from the SLM back to the cylindrical mirror and grating (2300 lines/mm) to reverse the spectral decomposition.

6.2 Quantum metrology

The estimation of the separation and other parameters (like relative intensity or centroid) of two close incoherent signals is an ubiquitous problem in scientific and industrial fields. It finds applications in global positioning system devices [104, 105], measuring excitations in biological samples [106] and condensed matter physics [107] to name a few. Contrary to coherent signals, interferometric methods cannot be used when there is little or no coherence between the two signals. Traditionally, spatial intensity measurements of the signals are used to estimate the separation $\mathfrak{s}$ and other parameters. However, this method is limited by the diffraction resolution of the system, described by Abbe's limit and the Rayleigh curse [108, 109]. Information science provides a modern framework to analyze the problem. To exploit it, we need to introduce the concept of Fisher information.

The work presented in this section is the result of a collaboration between us and the groups of Prof. Dr. Luis Sanchez-Soto, Prof. Dr. Jaroslav Řeháček and Prof. Dr. Zdeněk Hradil. The theory was developed by these collaborators and we performed the experiments. The final analysis and results presented here are the product of the discussion between all the collaborators.

6.2.1 Fisher information and parameter estimation

In 1922, Ronald A. Fisher revolutionized the statistics by revisiting the Bayes theorem and quantifying the amount of information gained from conditional probabilities, the Fisher information (FI)

[110, 111]. In short, contrary to the dominant least squares method to estimate statistical quantities, Fisher carefully analyzed maximum likelihood estimation methods, introducing estimator functions. The variance of this estimators is the inverse of the FI which quantifies how much the function changes with the variation of the target parameter. Therefore, the minimum variance gives the best estimation of the parameter which is achieved when the maximum FI is available. These functions can be measurements $\hat{\mathfrak{z}}$ of a parameter $\mathfrak{z}$ in a system. The quality of this measurements is then given by the its variance $\mathrm{var}(\hat{\mathfrak{z}})$, quantified by the FI $\mathcal{F}$ per measurement, with $\mathrm{var}(\hat{\mathfrak{z}}) > 1/\mathcal{F}$ [112].

Let's revisit the intensity measurement limit, in the case of the estimation of the spatial separation of two incoherent signals. The FI is contained in each photon detected in the intensity measurement $\mathrm{I}(x, \mathfrak{s}_x)$, where x is the spatial axis and $\mathfrak{s}_x$ the spatial separation. Analogously, for two signals separated in the time-frequency domain the intensity distribution is given by the incoherent mixture of both fields, as depicted in figure 6.5. The intensity is then

$$\mathrm{I}(\omega, \mathfrak{s}_\omega) = \left|\alpha_{\mathrm{G}}(\omega - \frac{\mathfrak{s}_\omega}{2})\right|^2 + \left|\alpha_{\mathrm{G}}(\omega + \frac{\mathfrak{s}_\omega}{2})\right|^2, \tag{6.2.1}$$

where α_{G} are the Gaussian spectral envelopes with bandwidth σ of each individual signal. This could be measured with a spectrometer. Then, the Fisher information available to estimate $\mathfrak{s}_\omega$ with N measured photons is given by

$$\mathcal{F} = \mathrm{N} \int_{-\infty}^{\infty} d\omega \frac{1}{\mathrm{I}(\omega, \mathfrak{s}_\omega)} \left(\frac{\partial \mathrm{I}(\omega, \mathfrak{s}_\omega)}{\partial \mathfrak{s}_\omega}\right)^2. \tag{6.2.2}$$

The variance of the estimator is described with $\mathrm{var}(\hat{\mathfrak{s}}_\omega) > 1/\mathcal{F}$. An ideal estimator would have $\mathrm{var}(\hat{\mathfrak{s}}_\omega) = 0$ and always give exactly the value of $\mathfrak{s}_\omega$. From the Fisher information of an intensity measurement, if $\mathfrak{s}_\omega \gg \sigma$ then the variance is limited to $\mathrm{var}(\hat{\mathfrak{s}}_\omega) = 4\sigma^2/N$. As $\mathfrak{s}_\omega \sim \sigma$ the Fisher information starts to decrease and the variance increases, diverging to infinity when $\mathfrak{s}_\omega \to 0$. This makes it impossible to estimate the separation between two signals closer than their width. This

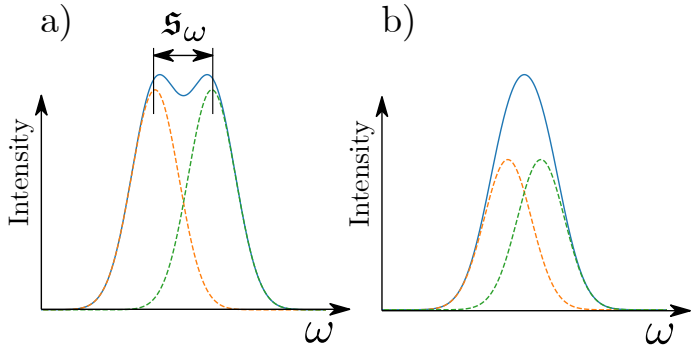

Figure 6.5: The green and orange lines are the two Gaussian signals with a frequency separation $\mathfrak{s}_\omega$ and bandwidth σ. The blue lines are the result of a intensity measurement of the signals. In a), $\mathfrak{s}_\omega > \sigma$ and the intensity measurement allows one to distinguish both signals. As $\mathfrak{s}_\omega$ approaches σ and beyond, it becomes harder to make out both signals from the intensity measurements as it is the case in b).

limit can be formalized with the Cramér-Rao lower bound (CRLB) [113, 114]. This is a fundamental limit for the classical estimation problem and it's also dubbed Rayleigh's curse as it is the resolution limit described by the Rayleigh's own diffraction limit criteria [2].

In 1969, W. Helstrom studied the problem under the quantum perspective , using the quantum counterpart of the FI [115]. The main different between classical and quantum FI is that, where classical FI has a unique local estimation function (a well defined set of measurements), in the quantum case the FI is given by all the possible quantum measurements [116]. With that, it can be shown that the quantum CRLB (Q-CRLB) maintains a constant value $\mathrm{var}(\hat{\mathfrak{s}}_\omega) = 4\sigma^2/N$ for any $\mathfrak{s}_\omega$ [117] below the classical CRLB.

6.2.2 Quantum parameter estimation with the QPG

The quantum Fisher information (QFI) provides lowest possible variance for the estimator. It can be accessed through phase-sensitive measurements. For the scenario considered here, of incoherent overlapping pulses, it can be shown that the partial derivatives of the spectral envelopes provide the optimal measurement basis for the quantum estimator. This is discussed in detail and derived in [118]. In particular, since we are considering Gaussian envelopes, these happen to be the HG basis. The QPG can project the signals into these modes and extract the information for the estimator. The two first order HG mode are sensitive to changes of $\mathfrak{s}_\omega$. By projecting the signal onto these two modes we obtain the ratio

$$\frac{P_{\mathrm{HG1}}}{P_{\mathrm{HG0}}} \approx \frac{\sigma_{\mathrm{PM}}^2}{4\sigma_{\mathrm{sig}}^2} + \frac{\hat{\mathfrak{s}}_t^2}{16\sigma_t^2} + \frac{\hat{\mathfrak{s}}_\omega^2}{16\sigma_{\mathrm{sig}}^2}. \tag{6.2.3}$$

Here, P_{HG0} and P_{HG1} are the QPG output intensities of the signal on the zeroth and first HG modes, σ_{sig} is the bandwidth of the signal, $\hat{\mathfrak{s}}_t$ and $\hat{\mathfrak{s}}_\omega$ are the estimators in time and frequency, and σ_t the time bandwidth of the signal. Assuming that the two signals are only separated in one degree of freedom (t or ω), equation 6.2.3[2] allows one to calculate the estimator with quantum resolution. This method was successfully implemented by Donohue et al. in 2018 [81]. They estimated the separation in frequency and time of two incoherent signals below the CRLB and saturating the Q-CRLB.

6.2.3 Multiparameter estimation

The first quantum estimation approach in [81] was limited to the estimation of a single parameter: the separation between the two incoherent signals. However, the method can be expanded to multiparameter estimation if the correct measurement basis to extract the QFI is used. We follow the methods outlined in [118, 119] to perform multiparameter estimation of the signal with the QPG. The discussion that follows can be expanded with the original publication of the results in [88].

Taking advantage of the temporal mode framework of the QPG, we focus on the time domain. Specifically, we want to simultaneously estimate the temporal separation τ, temporal centroid τ_0 and intensity difference $1-\mathfrak{q}$ between two incoherent time pulses when their temporal separation is very small. The estimated quantity can then be collectively named $\theta = (\tau, \tau_0, \mathfrak{q})$ and the estimator $\hat{\theta}$. The pulses and the estimated quantities are described in figure 6.6a). The incoherent mixture is then given by

[2]For a detailed derivation of equation 6.2.3, the reader is refereed to the appendix in [81]

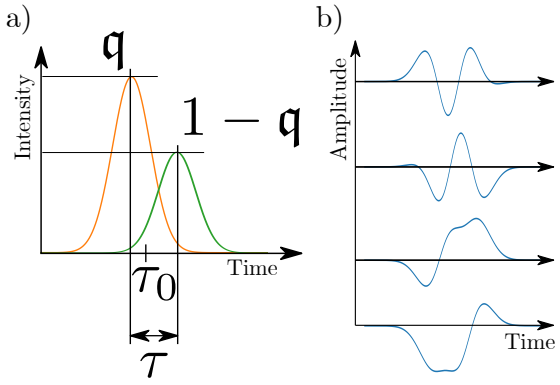

Figure 6.6: a) Two incoherent time pulses and the quantities to be estimated through phase-sensitive measurements. b) Optimal measurement basis for the estimation of the three parameters τ, τ_0 and $\mathfrak{q}$.

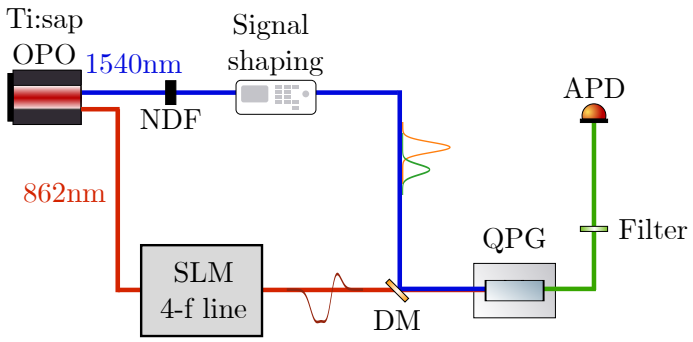

Figure 6.7: Simplified version of the experimental setup in figure 6.1 with details for the demonstration of multiparameter estimation at the quantum limit. The signal at 1540nm it is shaped into one of two incoherent signals for negative and positive time delays (orange and green) with programmed parameters $-\tau/2, \tau_0$ and $\mathfrak{q}$ and sent to the QPG. The pump for the QPG process is centered at 862 nm. The pump is shaped into the measurement basis modes using the SLM 4-f line setup and sent to the QPG. After the QPG, remaining pump and signal fields are tapped off and the converted signal at 553nm is filtered. The filtered light is measured the APD and time taggers. Figure legend: neutral density filter (NDF), dichroic mirror (DM), avalanch photon detector (APD).

$$\mathrm{I}(t) = \mathfrak{q}\,|\alpha(t-\tau_0-\tau/2)|^2 + (1-\mathfrak{q})\,|\alpha(t-\tau_0+\tau/2)|^2\,. \tag{6.2.4}$$

In the multiparameter case, one needs to consider not only the variance of each parameter but also the interplay between different parameters. This is described by the covariance matrix. Similarly, the quantum Fisher information is given by a matrix $\mathcal{Q}(\theta)$ sensitive to changes in all three parameters. Therefore, the estimator limit is given by the covariance with

$$\mathrm{cov}(\hat{\theta}) \geq \mathcal{Q}^{-1}(\theta). \tag{6.2.5}$$

Given the presence of more than one estimator, this new multiparameter bound is only saturable if the measurements for every parameter are compatible (non-destructive) [120].

To saturate the bound and achieve the ultimate estimation resolution, we find the optimal measurements following [118]. These are the derivatives of the signals, which for Gaussian functions are HG modes. Four modes are sufficient for the optimal estimation of three parameters. These four modes are depicted in figure 6.6b). They are superpositions of the first four HG modes.

The experimental setup details for this experiment are described in figure 6.7. To generate two incoherent signals, the negative and positive time shifted pulses are shaped and measured separately, summing their results in post-processing to produce the incoherent mixture. This also avoids any spurious coherence from the pulses. The time centroid τ_0 is set at 0 without loss of generality and different intensity balances $\mathfrak{q}$ are measured. Each signal is measured sequentially with the four basis modes and each setting is measured 100 times for statistical significance with a measurement time of 2ms. Due to the long measurement times, the experimental apparatus was very sensitive to temporal drifts caused by laboratory environmental changes over time (e.g. temperature and air currents). To mitigate this, after a certain number of measurements the signal and pump delay is realigned to maximize QPG output. This is done by shaping the pump and signal fields into the orthogonal modes HG_0 and HG_1. Then, the QPG extinction ratio at the output is maximized by scanning the first order linear phase term[3] of the fields with their respective spectral shaping setups. This allows us to center pump and signal pulses in time again and maintain the QPG performance at its maximum.

Projections on these modes matched the expected values down to very small separations where the technique is limited by the shaping of the signal fields. In figure 6.8, the variances of the three estimators are plotted against the separation with the CRLB and Q-CRLB for comparison. We saturated the Q-CRLB in every case, demonstrating the ultimate quantum resolution.

The variances of the three estimators are shown in figure 6.9. These show the simultaneous estimation of time separation $\hat{\tau}$, intensity imbalance $\hat{\mathfrak{q}}$ and time centroid $\hat{\tau}_0$.

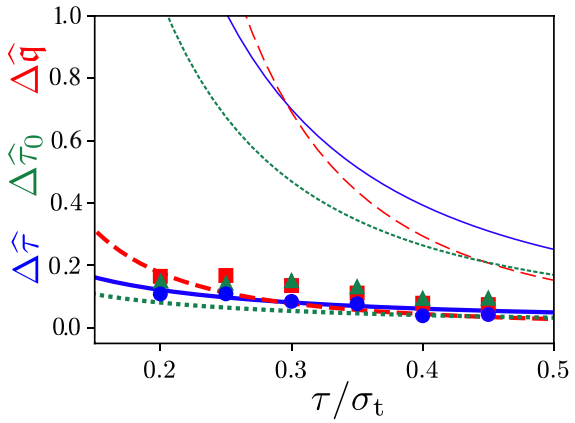

Figure 6.8: Variances of the measured estimators. The ticker lines follow the Q-CRLB and the thinner lines the classical CRLB. The colours correspond to the different parameters as indicated in the y axis. Figure from [88]

[3]The first order linear phase term of a pulse corresponds to a time delay.

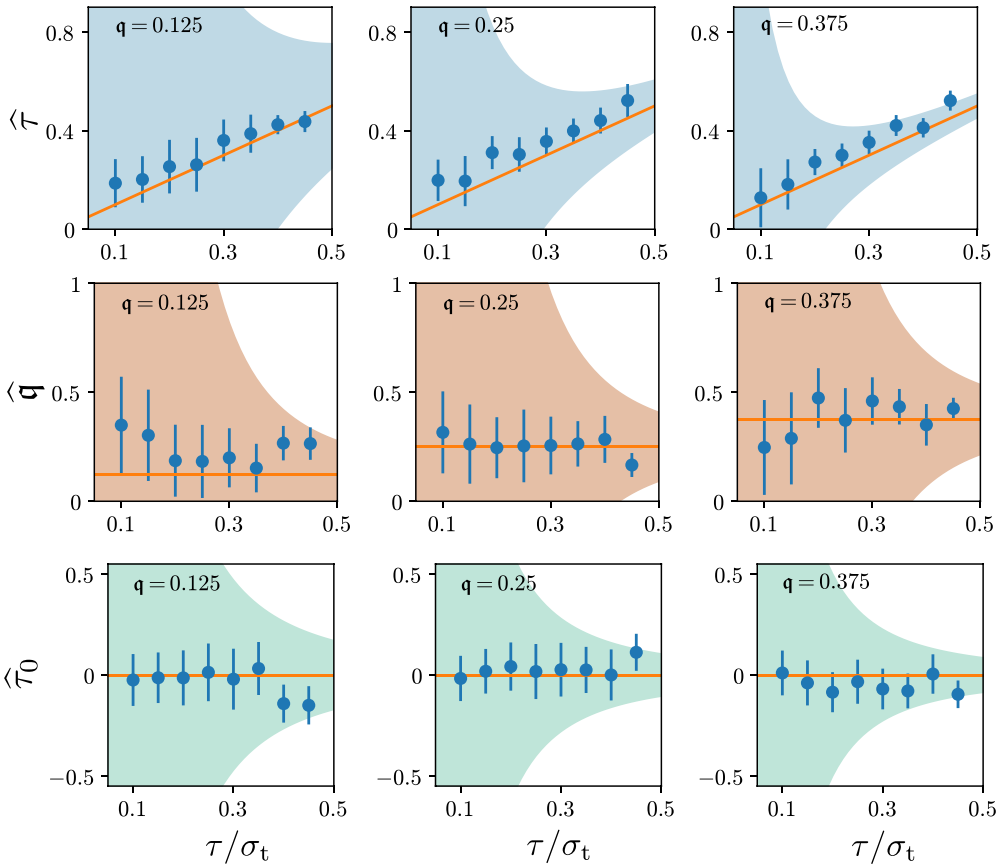

Figure 6.9: Experimental results for the simoultaneous estimation of τ, τ_0 and $\mathfrak{q}$. The solid lines are the programmed values of the parameters for each separation. The points mark the mean value of the estimator measurement with their standard deviation in vertical bars. The shadowed areas mark the limit marked by the classical CRLB with the number of photons measured experimentally. Figure from [88].

6.2.4 Coherence effects

So far, we have considered only the problem of discriminating incoherent pulses. An interesting question that arises is, how does the coherence of the signals impact the estimation techniques? This question has recently caused a heated scientific debate [121–128] where some argue that the presence of coherence in the signals leads to a resurgence of the Rayleigh's curse while others argue the opposite. Furthermore, other studies argue for an advantage to be gained from coherent signals, increasing the amount of information available for parameter estimation.

In the results presented here, and published and discussed in [95], we argue that coherent signal superpositions can be decomposed into symmetric ψ_s and asymmetric ψ_a coherent modes, as illustrated in 6.10, of in- and anti-phase time-shifted components $\psi_\pm(t) = \psi(t \pm \tau/2)$. The coherent modes define two measurement channels. Although this can effectively carry more information

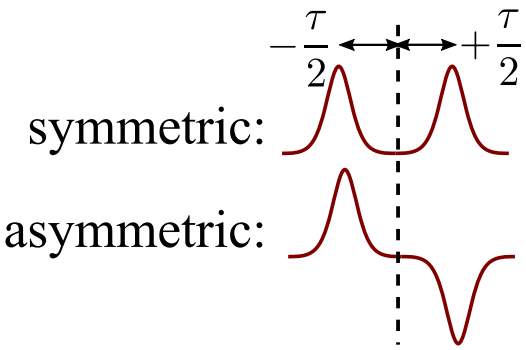

Figure 6.10: Amplitude of the symmetric and asymmetric coherent mixtures.

than the incoherent case, this does not necessarily result a metrological advantage. We present experimental results to support our conclusions.

The amplitude of the signal mixture of two coherent fields with a time separation τ is the described with

$$\mathrm{A}(t) = \frac{1}{\sqrt{2}}[\psi_-(t-\tau/2) + \psi_+(t+\tau/2)], \tag{6.2.6}$$

As we have discussed, the optimal measurement basis are the HG modes for Gaussian pulses. Then, measuring in these modes we obtain the following QPG projections on the coherent modes

$$p_\mathrm{s} \equiv |\langle \mathrm{HG_n}|\psi_\mathrm{s}\rangle|^2 = \begin{cases} p_\mathrm{n}(\tau) & \mathrm{n} = 0,2,4,\ldots \\ 0 & \mathrm{n} = 1,3,5,\ldots \end{cases}, \tag{6.2.7}$$

$$p_\mathrm{a} \equiv |\langle \mathrm{HG_n}|\psi_\mathrm{a}\rangle|^2 = \begin{cases} 0 & \mathrm{n} = 0,2,4,\ldots \\ p_\mathrm{n}(\tau) & \mathrm{n} = 1,3,5,\ldots \end{cases}. \tag{6.2.8}$$

Here, $p(\tau)_\mathrm{n}$ is the QPG conversion probability of the projection of the signal on $\mathrm{HG_n}$. We are focusing on estimating a single parameter, the time separation τ. Note that we can reproduce the fully incoherent case by adding both signal modes ψ_s and ψ_a since they happen in odd and even HG modes independently and together reproduce measurements on every HG mode. In this case, summing all the $p(\tau)_\mathrm{n}$ we obtain the Fisher information from equation 6.2.2 and reproduce the classical CRLB and analogously for the Q-CRLB.

In the fully coherent case, we measure both the symmetric and asymmetric signal mode and thus the Fisher information is

$$\mathcal{F}_\mathrm{s}(\tau) = \frac{1}{8\sigma_t^2} - \left(\frac{1}{8\sigma_t^2} - \frac{\tau^2}{32\sigma_t^4}\right)\exp\left(-\frac{\tau^2}{8\sigma_t^2}\right), \tag{6.2.9}$$

$$\mathcal{F}_\mathrm{a}(\tau) = \frac{1}{8\sigma_t^2} + \left(\frac{1}{8\sigma_t^2} - \frac{\tau^2}{32\sigma_t^4}\right)\exp\left(-\frac{\tau^2}{8\sigma_t^2}\right). \tag{6.2.10}$$

Measuring both separately, we obtain $\mathcal{F}_{\text{coh}}(\tau) = 1/4\sigma_t^2$, the quantum bound again. However, for small separations $\tau \to 0$

$$\mathcal{F}_{\text{s}}(\tau) \simeq 0 \quad \text{and} \quad \mathcal{F}_{\text{a}}(\tau) \simeq \frac{1}{4\sigma_t^2} \tag{6.2.11}$$

the intensity of in-phase symmetric components interfere constructively while the anti-phase asymmetric components interfere destructively due to the opposing phase. The intensity then goes to zero as they approach and contains all the information about the separation, this leaves the remaining intensity in the symmetric channel open to estimate other quantities.

Altogether, the information of the mixture has been sorted in the symmetric and asymmetric channels, like an information beam-splitter. The time separation information is contained in the vanishing intensity from the destructive interference of the asymmetric mode channel and all the remaining intensity is directed to the symmetric channel where other parameters can be accessed through new estimation measurements. For comparison, in the incoherent case, half the intensity is sent to both channels and both can be used for parameter estimation down to the quantum limit.

The controversy starts when partial coherence is in play. We describe this as a superposition of symmetric and asymmetric modes. The degree of coherence is quantified with γ, where $\gamma = 0$ is the fully coherent case and $\gamma = 1/2$ the fully incoherent. The Fisher information is then

$$\mathcal{F}_{\text{s}}^{\gamma}(\tau) = (1-\gamma)\mathcal{F}_{\text{s}}(\tau) + \gamma\mathcal{F}_{\text{a}}(\tau), \tag{6.2.12}$$

$$\mathcal{F}_{\text{a}}^{\gamma}(\tau) = \gamma\mathcal{F}_{\text{s}}(\tau) + (1-\gamma)\mathcal{F}_{\text{a}}(\tau). \tag{6.2.13}$$

Consequently,

$$\mathcal{F}^{\gamma}(\tau) = \mathcal{F}_{\text{s}}^{\gamma}(\tau) + \mathcal{F}_{\text{a}}^{\gamma}(\tau) = \mathcal{F}_{\text{incoh}} = \frac{1}{4\sigma_t^2} \tag{6.2.14}$$

Therefore, no matter the degree of coherence present in the system, phase-sensitive measurement (in particular HG modes for Gaussian signals) are the optimal parameter estimation technique and the Q-CRLB is always the ultimate limit. There is also nothing to gain from coherence, only that information is divided in the signal mode phase channels.

We experimentally demonstrate this result by estimating the time distance of the signal mixture with different degrees of coherence and examining the estimator values and their variances. The experimental setup is the same as in figure 6.7. In this case, instead of independently shaping the incoherent fields, we shape the signal into the symmetric and asymmetric modes at different τ. The projections of the mixture on the measurement basis are measured and the estimator $\hat{\tau}$ values are obtained for each programmed separation and at different degrees of coherence γ.

The results are shown in figure 6.11. The estimators beat the CRLB and approach the Q-CRLB for every measurement configuration and degree of coherence investigated. The results remarkably follow our theoretical discussion earlier. No metrological advantage (or disadvantage) comes from the presence of coherence in the signal mixture. Coherence can be exploited as an information sorter, distributing the information into different coherent channels.

6.3 Randomized compressive tomography

High-dimensional Hilbert spaces, such as the one generated with the PDC source discussed in section 7, come with new challenges for their final use. A trustworthy method to characterise the

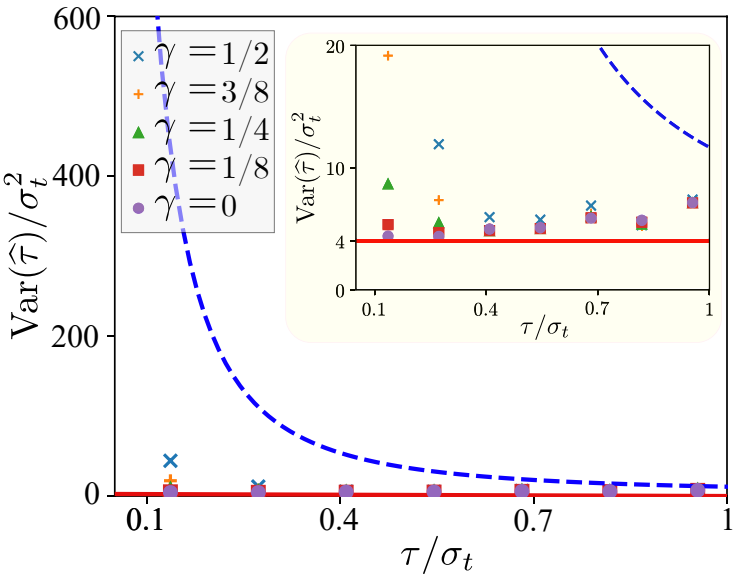

Figure 6.11: Variance of the estimator $\hat{\tau}$ as a function of the programmed time separation τ. The measurements were done with different degrees of coherence. The blue dashed line marks the CRLB and the solid red line the Q-CRLB. The inset is a zoom in on the y axis to better observe the behaviour. Figure adapted from [95].

states is key to achieve quantum performance. Quantum state tomography techniques allow one to reconstruct states [129, 130], measuring their properties (e.g. spectral amplitude and phase of a TM encoded state). However, these techniques usually requires a great number of measurements, on the order of $d(d+1)$ [129] where d is the dimension of the space. The number of measurements combined with the photon-starving environments of quantum systems make this techniques unideal for real world applications where the least number of states should be lost in characterisation.

For example, state tomography can be performed with the QPG by projecting the state into a set of mutually unbiased bases. This was experimentally demonstrated by Ansari et al. [80], using the QPG to perform tomography measurements with fidelity up to 99% in 7-dimensional states. The state tomography at 7 dimensions required 3136 measurements. If we want to scale our photon states to high-dimensional spaces to benefit from their advantages, this technique becomes unfeasible very quickly, scaling exponentially with the dimension.

We introduce a new state tomography technique inspired by compressive sensing and single-pixel cameras which is able to reconstruct unknown states with less measurements than standard tomography: randomized compressive tomography (RCT). The method and unprecedented experimental results in this section were published in [131].

The work presented in this section is the result of a collaboration between us and the groups of Prof. Dr. Luis Sanchez-Soto and Prof. Dr. Hyunseok Jeong. The theory was developed by these collaborators and we performed the experiments. The final analysis and results presented here are the product of the discussion between all the collaborators.

6.3.1 State description

We detail the steps required to reconstruct a pure quantum state in the time-frequency domain, e.g. the state of one of the photons from the PDC source in section 7. The state can be expressed with the broadband operators as a superposition of frequency components[4],

$$|\psi\rangle = \int d\omega A^\dagger |0\rangle. \tag{6.3.1}$$

It is useful now to use the density matrix $\rho = |\psi\rangle\langle\psi|$ to simplify the notation for the problem. In many real applications, photon sources won't produce completely pure states and we have to account for possible mixedness. A mixed state can be described with

$$\rho_{\text{mix}} = \sum_{\text{nn'}} \lambda_{\text{nn'}} |\psi_{\text{n}}\rangle\langle\psi_{\text{n'}}|, \tag{6.3.2}$$

with the rank of the mixed stated defined by the number of different n and n' states present. A pure state then has rank 1.

As we are interested in the information in both time and frequency domains of ρ, it is useful to describe them together with the so-called "chronocyclic Wigner function"[5] [132–134], an adaptation of the original Wigner function for the time-frequency domain. It is defined

$$\mathcal{W}(t,\omega) = 2\int dt' e^{2i\omega t'} \langle t - t'|\rho|t + t'\rangle \tag{6.3.3}$$

$$= 2\int d\omega' e^{-2i\omega' t} \langle \omega - \omega'|\rho|\omega + \omega'\rangle, \tag{6.3.4}$$

in time and frequency. From now on, we will simply call it the Wigner function. Depending on the time-frequency encoding under study, the Wigner function changes. We will investigate it for TMs and frequency bins.

For HG_n modes of order n, the Wigner function takes the form

$$\mathcal{W}(t,\omega) = 2(-1)^\text{n} e^{-(t^2+\omega^2)^2} L_\text{n}(2t^2 + 2\omega^2). \tag{6.3.5}$$

Here L_n are the Laguerre polynomials of order n. In summary, the Wigner function for HG modes reduces to Laguerre-Gaussian functions.

TMs are not the only useful description of photon time-frequency components. Another important time-frequency encoding basis are frequency bins [135, 136] like the ones found in frequency combs [137]. Therefore, it is interesting to consider them. Frequency bins are narrow-band pulses completely described in the frequency domain. We cannot use broadband modes to describe them, their amplitude $f(\omega)$ is given by

$$f_{\text{nn'}}(\omega', \omega'') = \sum_{\text{nn'}=0}^{\text{d}} f_{\text{nn'}} \delta(\omega' - \omega_\text{n})\delta(\omega'' - \omega_\text{n}), \tag{6.3.6}$$

where δ are delta functions of the frequency, and the frequency bins are defined by a set of dimension d, $\{\omega_\text{n}\}_{\text{n}=0}^{d}$. From a pulse description, it is handy to describe the frequency bins around the central

[4] The approach can be analogously applied to time components through Fourier transforms

[5] The term comes from the juxtaposition of time and frequency variables in the function.

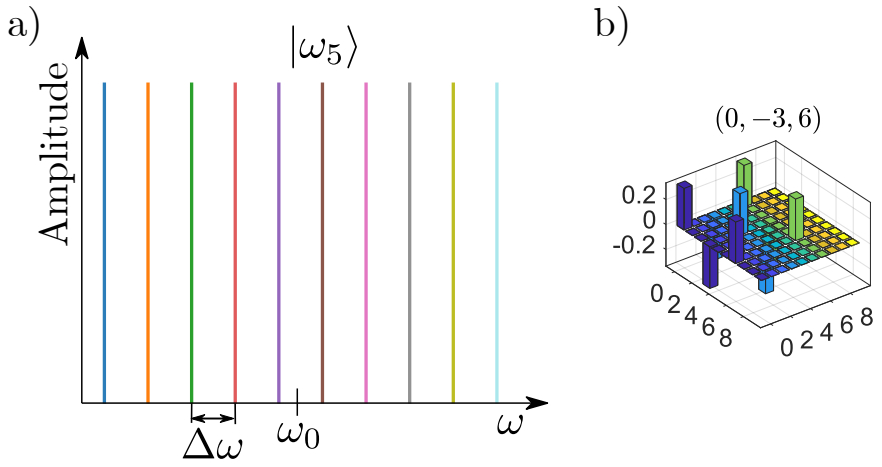

Figure 6.12: a) Bins of a 10-dimensional space. b) Density matrix of the bin state defined by the superposition of bins $|\psi\rangle = 1/\sqrt{3}(|\omega_0\rangle - |\omega_3\rangle + |\omega_6\rangle)$.

frequency ω_0 of the pulse and with a fixed frequency spacing $\Delta\omega$, $\omega_{\rm n} = \omega_0 + \Delta\omega[{\rm n} - ({\rm d}-1)/2]$. An example of a 10-dimensional frequency bin space is depicted in figure 6.12a).

The frequency bin states are then $\rho = \sum_{\rm nn'} |\omega_{\rm n}\rangle f_{\rm nn'} \langle\omega_{\rm n'}|$ and the Wigner function is

$$\mathcal{W}(t,\omega) = \sum_{\rm nn'=0}^{\rm d-1} f_{\rm nn'} e^{i(\omega_{\rm n}-\omega_{\rm n'})t} \delta(\omega - (\omega_{\rm n} + \omega_{\rm n'})/2). \tag{6.3.7}$$

In this case, the Wigner function oscillates in time while it is a delta in frequency as a result of the idealized description of the frequency bin state with zero-width frequency bands. However, all the spectral information is contained in $f_{\rm nn'}$ which can still be represented using the density matrix.

6.3.2 RCT method

The problem then is to reconstruct an unkown state of rank-r and dimension d, described by ρ. Although for a scan tomography technique $\sim {\rm d}^2$ measurements are needed, in principle, there exists a set of measurements $M \ll \mathcal{O}(d^2)$ that unambiguously describes a low-rank state. Such a measurement set is called informationally complete (IC). De facto, there must exist a set of basis of dimension d that fully reconstructs the state in the minimum possible number of basis states.

We introduce the RCT scheme to find such an IC set of basis without any ad hoc assumption about the orignal state. The scheme characterises an unknown low rank time-frequency state $\rho_{\rm d}$ of finite dimension d and rank much smaller than the dimension, ${\rm r} \ll {\rm d}$, in less measurements than MUB scan tomography.

The scheme works in a bottom-up process in which the state is projected onto independent bases states $\mathcal{B}_k = \{|b_{k,0}\rangle, |b_{k,1}\rangle, \ldots, |b_{k,{\rm n}}\rangle, \ldots, |b_{k,{\rm d}-1}\rangle\}$ of dimension d. Similar to compressed sensing schemes [138], single shot measurements projecting the target on bases that do not completely describe the state accumulate information about its composition and build a volume of possible

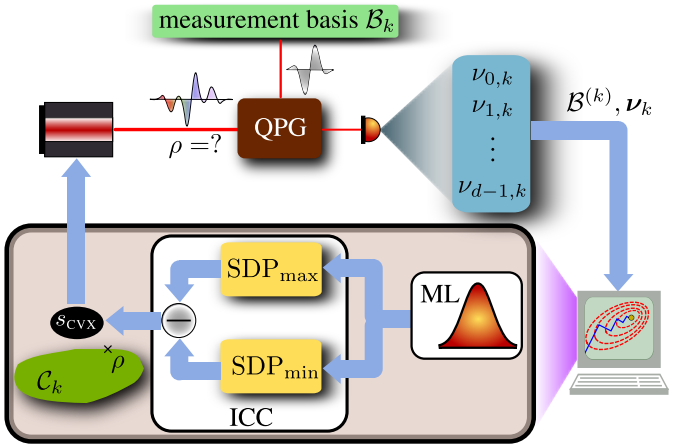

Figure 6.13: Scheme of the iterative RCT method. The QPG setup is the one described in figure 6.1. Reprinted with permission from [131] ©The Optical Society.

bases that after a number of measurements K, reduce to one unique solution that fully reconstructs the original state.

The process is done in two steps that are repeated until a solution is found as illustrated in figure 6.13. In the first step, the state is sequentially projected on the modes of basis $\mathcal{B}_k$ on the QPG by shaping the pump of the QPG into each basis mode. The counts for each mode in the output of the QPG gives us the relative frequencies $\nu_{k,n}$ (with n the basis mode order). The frequencies are mapped into an operator $\hat{p} = \langle b_{k,\text{n}}|\rho_\text{d}|b_{k,\text{n}}\rangle$ obtained through a maximum-likelihood (ML) method that maximizes the likelihood function describing the QPG projections over the searched d-dimensional state space [139–142].

The second step of RCT is the informational completeness certification (ICC). It determines whether there is more than one state that fits the ML probabilities $\hat{p}$. If that is the case, there is a convex set ($\mathcal{C}_k$) of states with a nonzero volume s_{CVX}[6]. Through the accumulation of spectral information from different basis projections, the solution volume decreases until it is zero and the basis that reconstructs the original state is unique [143]. At step k =K$_{\text{IC}}$, the volume is zero and we have found the unique basis.

6.3.3 Experimental realization

To perform the experiment, the QPG signal input is shaped into different HG modes and frequency bin states as input states to be reconstructed. Then, RCT is performed by sequentially shaping the pump into randomly rotated bases states of dimension d and analysing the relative frequencies. An example of the rotation of the basis and the QPG measurement of the relative frequencies is described in figure 6.14. This is repeated until the volume s_{CVX} reaches 0 and we retrieve a unique reconstruction of the input state. The experimental setup is analogous to that in figure 6.7. In this case, the signal pulses are centered around 1541nm and the pump pulses at 857nm. The signal is

[6]The ICC and s_{CVX} calculation involves semidefinite programming techniques which are out of the scope of this thesis. An explanation is given in appendix A in [131].

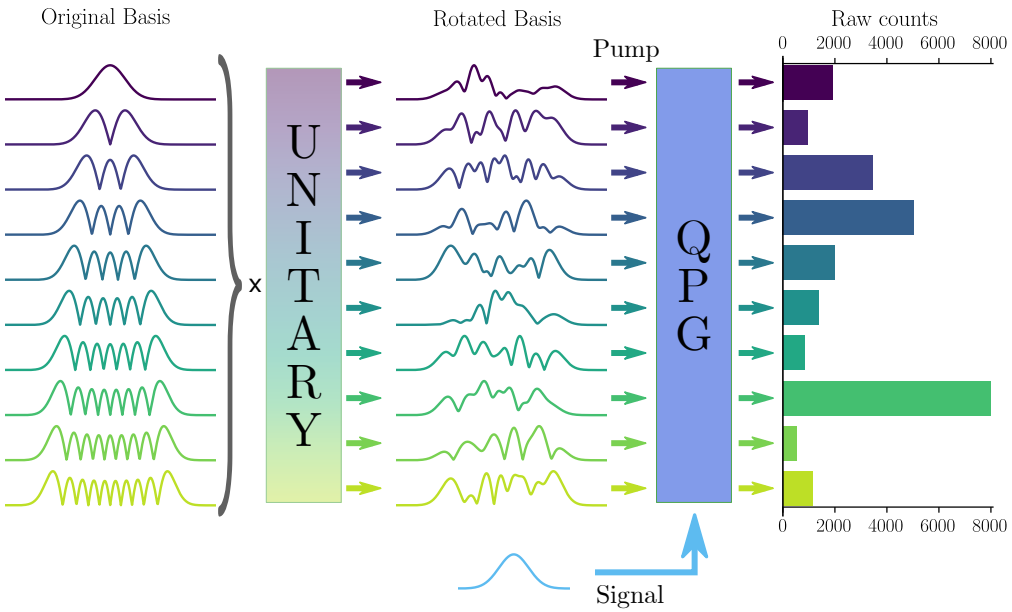

Figure 6.14: QPG projection of an state on a set of rotated basis for the RCT scheme. The original HG basis are rotated through a randomly generated unitary operation, the pump is then sequentially shaped into the rotated basis modes and the input mode projected into each of them. The raw photon counts in the output mode of the QPG are the relative frequencies. The counts shown are from a real experimental measurement. Reprinted with permission from [131] ©The Optical Society.

attenuated down to the few-photon level (~ 12). For each input state studied, 100 to 200 bases of M rotated basis modes are created, where M is equal to the dimension of the space d. The output mode of the QPG for each basis mode is measured for 20ms on the avalanch photon detector. In the following, we present the experimental results for HG modes and frequency bin states.

Hermite-Gaussian modes

The scheme is first implemented on a 10-dimensional HG modes space. Random rotations through unitary transformations of the HG modes basis are generated for each RCT run. Pure HG modes HG_0 to HG_3 and mixed states of up to rank 4 are used as input states and measured. The evolution of the solution volume and the fidelity of the reconstructed states with the RCT steps K are shown in figure 6.15a) and b). Examples of some pure and mixed reconstructed Wigner functions are shown through 6.15c) to f).

The solution volume is reduced to zero in as quick as 4 RCT steps, meaning that a unique solution is found in $K \times d$ =40 measurements. The fidelities reach values around 80% in around 10 steps RCT steps, meaning 100 measurements for the 10 dimensions. A scan tomography method would need 90 measurements with usually around 100 repetitions for statistical significance, for a total of 9000 measurements, to reproduce similar results. With RCT we demonstrate a one order

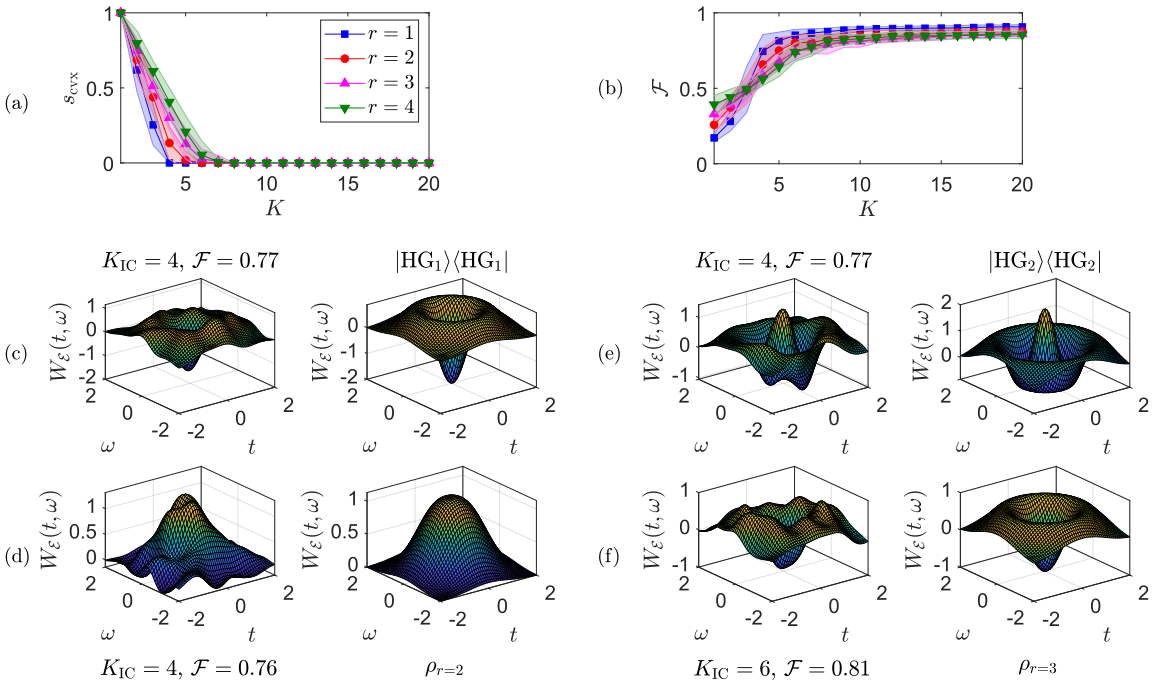

Figure 6.15: a) Evolution of the solution volume s_{CVX} with each RCT step K for HG pure and mixed states. b) Evolution of the fidelity of the reconstructed Wigner functions with K and for the same pure and mixed states as a). c)-f) Reconstructed Wigner function of two pure HG modes and two mixed states of rank 2 and 3.

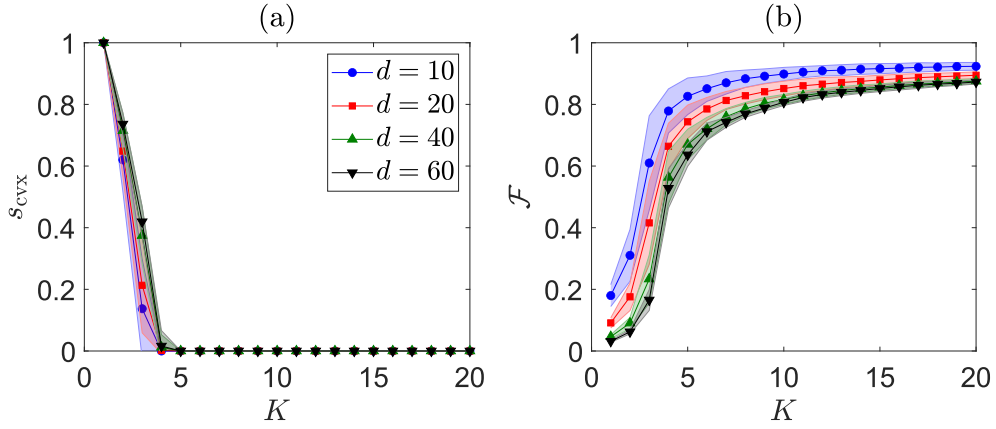

Figure 6.16: Solution volume and reconstructed Wigner function evolution of HG_0 for measurement basis dimension up to 60. Reprinted with permission from [131] ©The Optical Society.

of magnitude advantage in the number of measurements needed to reconstruct the original state.

To prove the scalability of the method, we performed RCT with HG basis up to 60 dimensions on an input HG_0. The results are shown in figure 6.16. The method works up to d=60 without any noticeable impact on K or the maximum fidelity. The 60 dimensions are only limited by the pump shaping resolution.

Frequency bins

We now test the RCT scheme with frequency bin states to further prove that it is system independent. The ideal bin description is approximated with narrow frequency square functions. The input state is shape into superposition of different frequency bins from a 10-dimensional space. For the pure state we choose the following superpositions of the the 0^{th}, 3^{rd} and 6^{th} bins

$$|\psi\rangle = \frac{1}{\sqrt{3}} \begin{cases} (|\omega_0\rangle + |\omega_3\rangle + |\omega_6\rangle) \\ (|\omega_0\rangle - |\omega_3\rangle + |\omega_6\rangle) \\ (|\omega_0\rangle + |\omega_3\rangle - |\omega_6\rangle) \\ (|\omega_6\rangle + |\omega_3\rangle - |\omega_0\rangle) \end{cases} . \tag{6.3.8}$$

Mixed states can be generated with statistical mixtures of the four pure states with random coefficients.

In this scenario, the pump is shaped into rotations of the basis defined by the 10 individual frequency bins. The results are shown in figure 6.17. The behaviour is consistent with that of the HG modes, confirming that RCT is also system independent. K_{IC} are on average larger than in figure 6.15 due to more significant experimental noise being present in the shaping of frequency bin states. This also reflects in slightly lower fidelities achieved in the reconstructed Wigner functions. It must be highlighted that this is not a sign of RCT reduced performance and the self-consistent ICC process works even for full-rank states only requiring larger K_{IC} and the experimental noise from the frequency bin shaping is the only factor reducing the fidelity[7]. The noise is caused by the small frequency features of the bins in the wide signal spectrum. They are much more affected by fluctuations of the laser spectrum.

With these experimental results, we demonstrate that RCT is an ideal state tomography method for low rank states. We reconstructed both, HG and frequency bin modes with high fidelities in an order of magnitude less measurements than a traditional scan tomorgaphy.

[7] Systematic errors were introduce in the model to prove this in appendix B in [131].

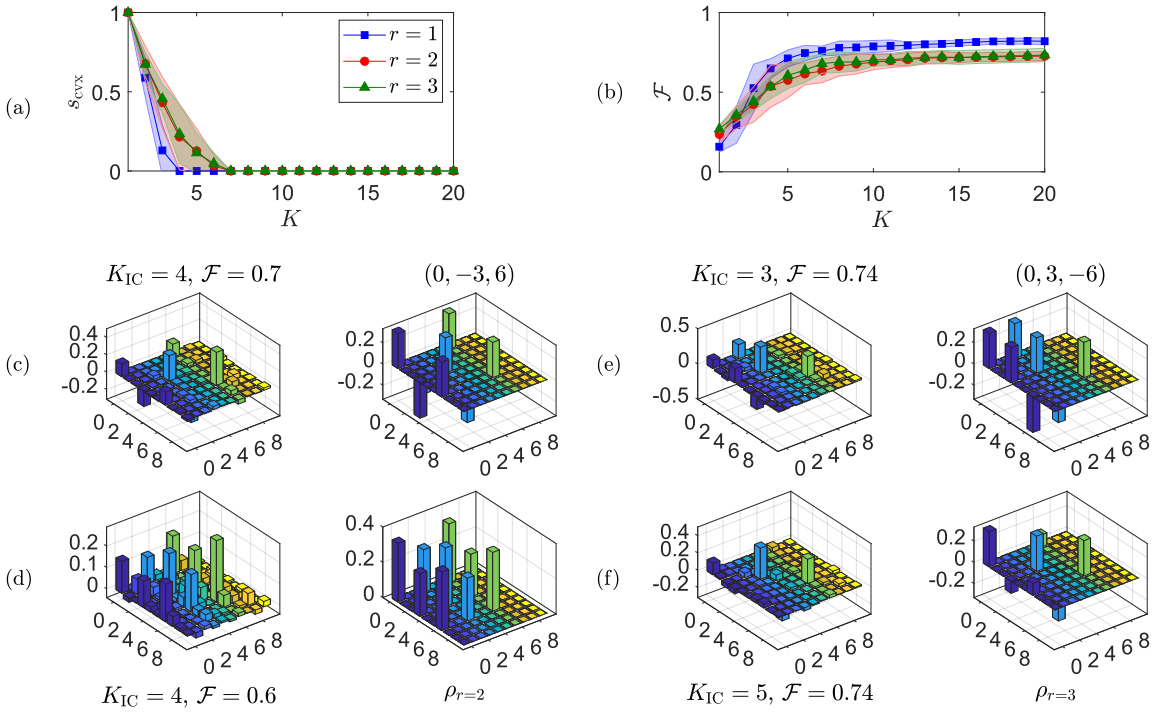

Figure 6.17: a) Evolution of the solution volume s_{CVX} with each RCT step K for frequency bin pure and mixed states. b) Evolution of the fidelity of the reconstructed Wigner functions with K and for the same pure and mixed states as a). c)-f) Reconstructed Wigner function of two pure HG modes and two mixed states of rank 2 and 3.

Chapter 7

Orchestrating high-dimensional PDC states

Encoding photons in a high dimensional space provides greater information capacity and improves the security of quantum communication protocols [91–93]. As discussed in section 3.3.1, TMs span a high-dimensional space while being compatible with single-mode optics. This presents a major advantage, as TM-encoded photon states are compatible with standard telecom fibres.

The temporal mode distribution of a PDC bi-photon state is dictated by the JSA function. By manipulating both components of the JSA function (the PM function and the pump field) one can access and modify the TM composition of the photon states. To this end, non-linear process engineering and spectral shaping of the pump can be used. With these techniques, there have been results producing high-dimensional TM states [144, 145]. These experiments were able to control the number of modes but only in unbalanced distributions, meaning that the Schmidt coefficient of every mode isn't the same. This is not ideal since a known, controlled number of modes increases the security of a QKD protocol, giving the eavesdropper less information [93]. A balanced distribution of TMs is optimal as it leads to maximally entangled states [146] that would improve the security further [147]. Although there have been successful attempts at producing balanced maximally entangled TM distributions, they rely heavily on filtering and post-processing of the states [148, 149].

In this chapter, we demonstrate a controllable source of maximally entangled TM bi-photon states. We will discuss the details of the PDC source used and how to exploit its PM function to generate from single-mode uncorrelated bi-photon states to six-dimensional maximally entangled states. We introduce the technique for the the spectral manipulation of the pump field, a key component. The experimental results of the PDC source are then presented and the current limitations discussed.

7.1 Tailoring the JSA

The PDC source used is a periodically poled KTP sample (from the company AdvR) with the following parameters: 8 mm length, waveguide dimensions of 4µm × 6µm and poling period 117µm. The poling is chosen for a type II PDC process converting light from the near-infrared to telecom

wavelengths for future quantum communication applications. A type II process allows one to easily separate signal and idler photons with their orthogonal polarization. The precise wavelengths of pump (765.5nm), signal and idler (1532nm) are calculated to be in symmetrical group-velocity matching[1] (sGVM) in KTP [150], producing a PM function at 45°. In that case, when the pump is has a Gaussian envelope with a bandwidth that equals the bandwidth of the phasematching function, the JSA function produces a single-mode uncorrelated state, as seen in figure 7.1a). This was already experimentally demonstrated with measured signal and idler purities of 82.1 and 86.7 by Harder et al. in [29] using this source.

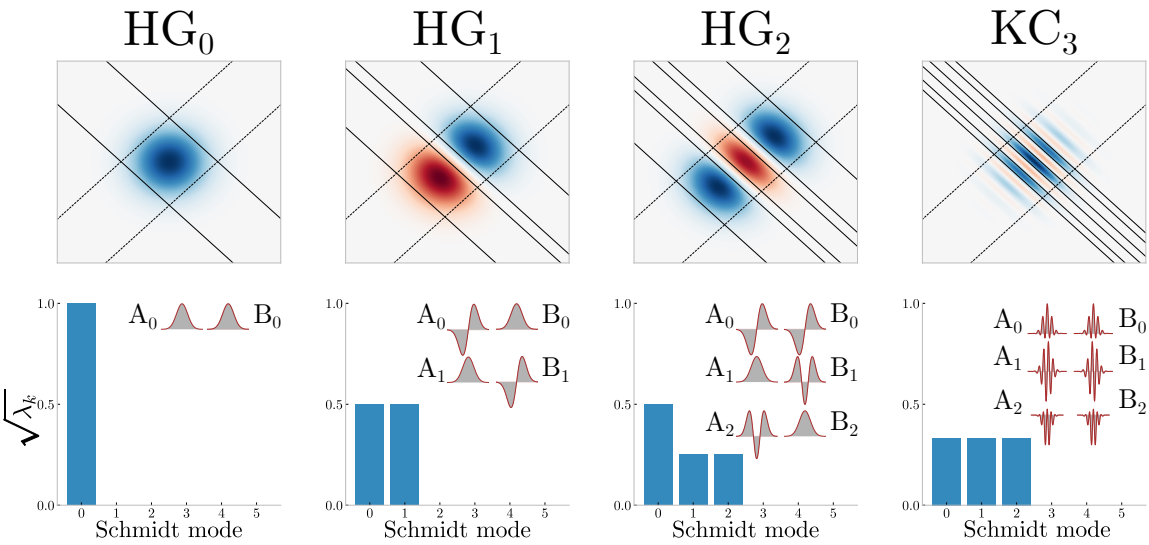

Figure 7.1: Simulations of the sGVM PDC source JSA functions. The pump is varied between the first three HG modes and the third order KC mode. In the top row, the axes represent the frequencies of signal and idler and the different colours (red and blue) describe regions of opposite spectral phase. The pump envelope and PM function 0.4σ width are represented by solid and dashed lines respectively. The corresponding Schmidt mode k distribution of Schmidt coefficients $\sqrt{\lambda_k}$ are plotted below for each JSA function. The insets represent the TMs A_k and B_k of the decomposition.

Moving away from a simple Gaussian pump envelope function allows one to tailor the number of modes in the Schmidt decomposition, as depicted in figure 7.1. First, we use the first and second order HG functions. When decomposing the resulting JSA functions from these HG modes, we observe two phenomena. First, the number of Schmidt modes is $K = N + 1$, where N is the order of the HG function. We can now control the number of modes in the distribution by choosing which HG function to use as pump envelope function. Second, already in the case of the HG_2 mode, it is shown that the distribution of the Schmidt modes is unbalanced, with rank lower than the number of modes. This is also the case for higher HG modes. Therefore, we cannot exploit HG modes to obtain maximally entangled states.

In 2012, G. Patera et al. [151] found a set of functions which can be tailored so that the N^{th}

[1]The group velocity of the pump is in between those of the signal and idler.

order of the functions has exactly N modes of rank N when decomposed into sets of orthonormal bases. This makes them the ideal basis for a high-dimensional maximally entangled PDC bi-photon state. We shall refer to these as N^{th} order kernel cosine (KC) functions. The function is defined by

$$KC_n = \sum_{i=0}^{n} \frac{1}{\sigma\sqrt{2\pi}} e^{-\left(\frac{\omega-\omega_0}{2\sigma}\right)^2} \cos\left(\frac{2n\pi}{\sigma}\omega(i+1)\right), \tag{7.1.1}$$

with σ the sigma bandwidth of the Gaussian amplitude and ω_0 the central frequency.

If we use a pump shaped with these functions, we can obtain JSA functions that decompose into N balanced Schmidt modes by choosing the N_{th} order KC mode. In this case, we can have any number of maximally entangled TMs in our bi-photon state. An example of KC_3 with 3 modes is shown in figure 7.1.

7.1.1 Measuring the modal composition

Obtaining the modal composition of the bi-photon state presents an experimental challenge. Measuring the JSA function includes a measurement of the spectral phase of the function. Although spectral techniques for such measurement exist [152–154] they are experimentally cumbersome and their resolution would limit the accuracy of the Schmidt decomposition, corrupting the final result. Alternatively, one can measure the joint spectral intensity (JSI) function. It can be measured with a time of flight spectrometer (TOF), by using a dispersive fiber to spread the spectra in time and map delay times to frequencies [155]. With the JSI function, we can make sure that the pump shaping is working properly. However, lacking the phase information, a second measurement is needed to obtain the TM distribution.

This measurement can be the unheralded second order correlation function. It has been shown to directly relate to the effective number of modes in the Schmidt decomposition of low gain regime PDC processes [67, 68]. To experimentally measure the unheralded $g^{(2)}(0)$ of a PDC photon, one can use the Hanbury-Brown-Twiss configuration (see figure 7.2c), the second order correlation function then reads

$$g^{(2)}(0) = \frac{\langle (n_1 n_2) \rangle}{\langle n_1 \rangle \langle n_2 \rangle} \tag{7.1.2}$$

where n_1 and n_2 are the counts on the photon detectors.

The effective number of modes K can then be defined, in the low gain regime, in terms of the $g^{(2)}$ function with [67]

$$K = \frac{1}{g^{(2)} - 1}. \tag{7.1.3}$$

As the number of modes k increases, so does K. For a single mode state, $g^{(2)} = 2$ and as K increases with higher number of modes, the $g^{(2)}$ function value approaches 1. The Schmidt number K also allows one to calculate the purity of the state with P= $1/K$ [29].

7.2 Generation of high-dimensional maximally entangled states

We use a pump spectrally shaped into different KC modes to demonstrate a PDC source of high-dimensional maximally entangled bi-photon states. The experimental setup is described in figure

7.2. The femtosecond laser source uses ultrashort pulses of 200fs at 1532 nm from a Ti:Sap pumped OPO system (Chameleon Compact OPO). The 1532 nm beam undergoes a second harmonic generation process in a bulk Lithium Niobate crystal, producing the 766 nm pump for the PDC process. The pump is shaped into the different KC modes in the 4f SLM setup and sent to the PDC crystal. The crystal is a rubidium exchanged KTP waveguide with a poling period of 9µm, 8mm length and waveguide width of 3µm. Before coupling for the PDC experiment, we characterise the intensity shaping of the pulses with an optical spectrum analyser (OSA) not shown in the final setup. The pump is in-coupled and out-coupled to the PDC source using aspheric lenses to match the input beam mode with the waveguide mode..

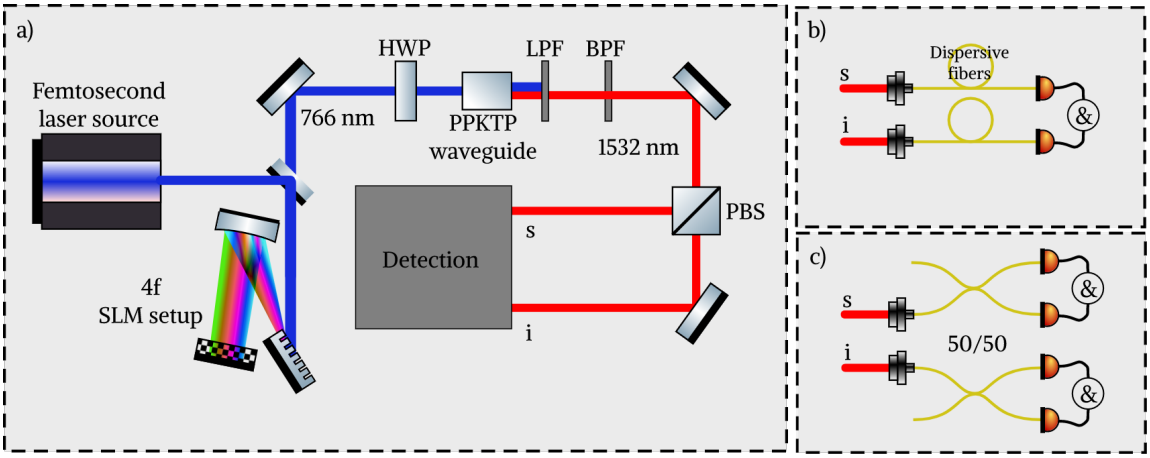

Figure 7.2: a) Experimental setup schematic. The femtosecond laser source produces the 766nm laser pulses for the pump. The pump beam goes through the folded 4f SLM setup for spectral shaping and is then reflected and coupled into the PDC source. After the long-pass filter (LPF) and the band-pass filter (BPF) the signal and idler are separated by polarisation with a polarizating beam splitter (PBS) and sent to the detection system. b) Detection configuration to acquire the JSI function of the PDC state. Signal and idler propagate through dispersive fibers and then the coincidences are measured with superconducting nanowire single photon detectors (SNSPDS). c) To measure the $g^{(2)}$ of signal and idler fields, they pass through fiber 50/50 beam splitters and the coincidences are measured in a Hanbury-Brown-Twiss interferometer configuration [156].

At the output of source, the unconverted pump is filtered out with a long-pass filter and the spectrum of the signal and idler photons is cleaned with a bandpass filter with a FWHM of 8 nm. The bandwidth of the filter is chosen such that it matches the width of the JSA function, thereby isolating the central lobe from the expected side lobes from the sinc^2 PDC PM function. This ensures uncorrelated JSA functions and increases the purity of the states [150]. Afterwards, signal and idler photons are coupled to single mode fibers and sent to the photon detectors for the measurements. Two different configurations are used to measure the JSI functions and $g^{(2)}$ values, shown in b) and c) in figure 7.2. They will be explained in the following sections.

The SLM used is a reflective liquid crystal oxide silicon SLM (Hamamatsu LCOS-SLM). The SLM is used in a folded 4-f line geometry, taking advantage of its reflectivity to reduce the number of components to a grating and a cylindrical mirror with focus f in place of the lenses. Any pulse

shape down to the resolution of the SLM setup can be imprinted in the pump pulses, up to the FWHM of the original pump field of 7 nm. The 4-f line SLM setup for pulse shaping is composed of a grating with 2400 lines per mm and a lens with 30 mm focal distance. The SLM itself has a screen with dimensions 15.8 × 12 mm and contains 800 × 600 pixels with 10μm pitch. With this configuration, the expected spectral shaping resolution of the SLM is 0.03 nm. To match the shaped pump modes with the PM function bandwidth, the KC modes have a 1.5nm FWHM. After shaping, the pump pulses are characterised for the different orders of KC functions with an OSA. Results are shown in the top row in figure 7.3.

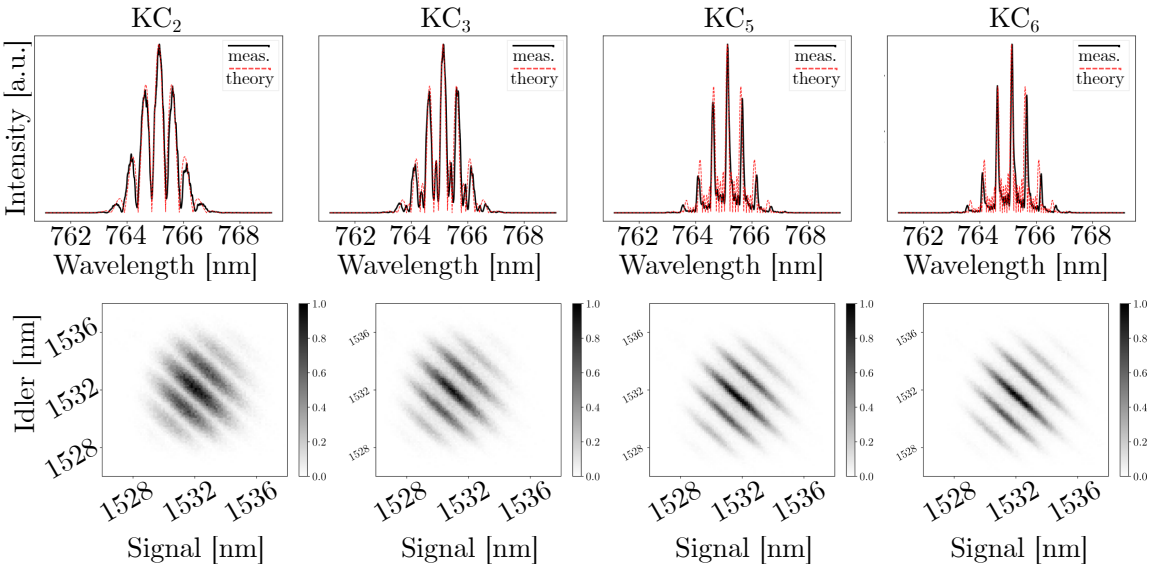

Figure 7.3: Measured pump spectrum (top) and JSI (bottom) for KC modes 2$^{\text{nd}}$, 3$^{\text{rd}}$, 5$_{\text{th}}$ and 6$^{\text{th}}$. The JSI intensity is plotted on the gray scale. From the 5$^{\text{th}}$ modes onward, it can be seen that the shaping of finer features is limited by the resolution of the SLM setup. For the JSI function measurements, the resolution is not enough to resolve the finer features from the 2$^{\text{nd}}$ mode onward.

7.2.1 JSI function measurements

The spectral properties of the tailored PDC states are characterised with the TOF fiber spectrometer in figure 7.2. Signal and idler photons travel through dispersive fibers before arriving at the photon detector. Due to the dispersion in the fibers, different frequencies arrive at different times, allowing one to correlate arrival times with frequencies in order to infer the spectrum of the photons. The resolution of the detection scheme is set by the interplay between the temporal resolution of the detectors and the amount of dispersion introduced. The coincidences on the detectors for signal and idler can then be measured to obtain the JSI function with a resolution of 0.12 nm. Smaller features on the JSA will not be seen by this measurement.

The measured JSI functions for each pump envelope function are shown in the bottom row in figure 7.3. The measured functions exhibit the expected profiles up to around 6 KC modes at

which point the resolution limit of the SLM setup degrades the measurements as the mode spectral features are smaller the spectral components of the pulse on the SLM 4f setup.

7.2.2 $g^{(2)}$ measurements

The $g^{(2)}$ values are measured for increasing orders of KC modes, with which we tailor the effective number of modes K in the bi-photon state. To measure the values we send signal and idler photons to the detectors through 50/50 fiber beam splitters in the Hanbury-Brown-Twiss configuration illustrated in figure 7.2b). From the measurements, we determine the K value using equation 7.1.3. The results are shown in figure 7.4.

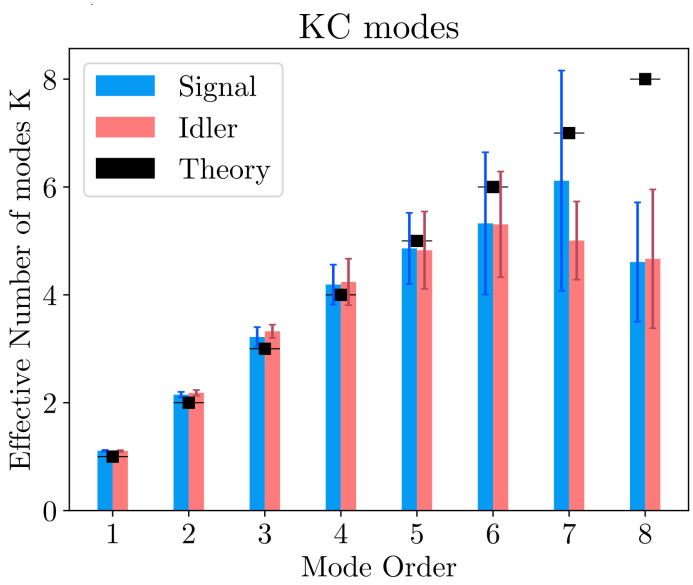

Figure 7.4: The order of the pump envelope function is plotted against the effective number of modes K. The effective number of modes K is inferred from $g^{(2)}(0)$ measurements for KC modes from 1 to 8. Error bars, representing the standard deviation of 20 measurements, are represented by vertical lines on top of the plot bars.

When increasing the order of the pump envelope function, we obtain an increasing number of effective modes. The results are within expected values up to 6 modes. The combination of the JSI and K measurement results show that using KC modes we can generate a controlled number of maximally entangled modes in the bi-photon state. Finally, when reproducing the uncorrelated pure state from [29] by shaping the pump with a Gaussian envelope of 1.5nm FWHM, we obtained a purity of $g^{(2)}(0) = 1.97 \pm 0.04$ improving over the former result and demonstrating a highly pure source of uncorrelated single-photons.

7.2.3 Resolution limit

Higher orders of the KC functions have increasingly smaller features. When these features reach the resolution limit of the shaping setup, the effective number of modes K in the state starts to

deviate from the expected value. From simulations of the JSA function with different pump shaping resolutions, we can obtain the expected K and explain the results obtained. The simulations are shown in figure 7.5.

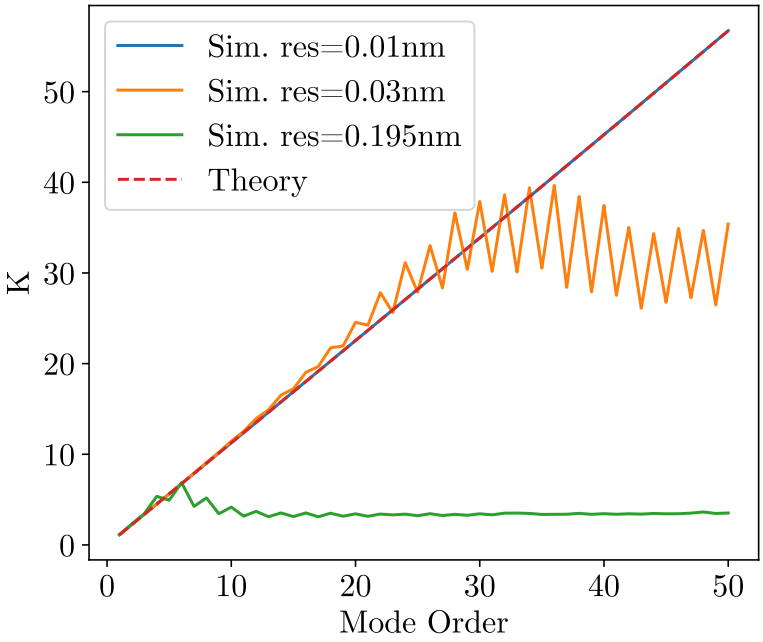

Figure 7.5: Expected effective number of modes in the PDC JSA function for different KC mode orders. The theory wiht no resolution limit and different pump spectral shaping resolutions are included for comparison. The simulation at 0.01 nm resolution lays directly below the theory line. The beating of the lines and differences with the perfect 1:1 KC mode order to K ratio are due to numerical errors in the simulation.

From the theoretical resolution of the SLM setup of 0.03 nm, we expect to achieve up to 20 modes. However, the experimental results only reached 6 modes. This matches with a simulated shaping resolution of 0.195nm. From this, we can conclude that the resolution of the SLM setup is ∼6.5 times higher than expected. This may be caused by an accumulation of slight missalignments of the different optical components of the SLM setup, unwanted spatiotemporal coupling from the interplay between the cylindrical mirror and grating or the defect on the screen of the SLM found after performing the experiments.

Improving the setup up to the expected resolution would already improve the results by a factor of 3. Increasing the resolution even further is desirable to reach mode numbers approaching 100. The simulation for 0.01nm resolution in figure 7.5 displays up to 50 modes and further. Increasing the resolution requires more pixels, this could be done by increasing the size of the SLM or by decreasing the size of the pixels[2].

[2]This is not as simple a fix as it sounds, as the last year of my PhD has proven.

In conclusion, we have presented an experimental setup to produce bi-photon states with a controlled number of TMs using KC modes. KC modes, in contrast to HG modes, produce the desired maximally entangled states. We exploited the sGVM condition of the PDC source and the spectral shaping of femtosecond laser pulses with an SLM to obtain an on-demand source of maximally entangled bi-photon states up to six dimensions. The system appears to be limited by the shaping resolution of the SLM setup.

Conclusions

Do not go gentle into that good night.
Rage, rage against the dying of the light.

Dylan Thomas

The development of quantum technologies relies on both theoretical research and experimental implementations. Many theoretical studies aim to describe quantum systems that can be exploited for real world applications: communications, cryptography, information processing... The task of experimental works is to transfer the ideal theoretical descriptions into experiments that either demonstrate their operation or whose results are fed back into the theory for its refinement. At the end of the road, experimental implementations will develop into working quantum devices that can be finally be exploited in day-to-day tasks. To do so, experimental implementations must be tailored to the needs of the quantum systems.

In the photonic framework, integrated optics are a cornerstone of future applications. They allow for miniaturisation of the devices and increase the efficiency of the processes. Together with non-linear optical effects, they present one of the most promising platforms for quantum technologies. Integrated non-linear devices can be engineered to interact with quantum information encoded in photons, accessing for example their spectral properties to generate highly interesting states of light or process the information within them. At the same time, these devices currently present a bottleneck. Further improvement in their performance relies on the fabrication of high-quality waveguides and extremely stable experimental conditions that are currently at the technological limit. To overcome these limits, we must develop a deep understanding of the fundamental classical working principles of waveguides and non-linear processes in order to ensure a solid base upon which to build tailored quantum devices. From there, we can design new devices and schemes to generate and process quantum light.

In chapter 4, a review of the state of the art of current quantum technologies revealed design flaws and technological restrictions that limit the performance of several quantum integrated devices. Additionally, this glance at the various kinds of devices (memories, light sources, processors, interfaces...) allowed us to asses the different requirements that the components of a quantum network need to work in harmony.

Following this, in chapter5 we investigated Ti:LN waveguide devices limits via comparison with simulations. Through the identification of the effects of waveguide and experimental inhomogeneities in the non-linear process of a QPG, the fabrication process is improved and a four-fold increase in the length of a QPG device demonstrates unprecedented performance under the benchmarks studied, namely: conversion efficiency, bandwidth compression and temporal mode

selectivity. Furthermore, guidelines for the design of QFC interfaces between quantum dots and streak cameras are given and a general design paradigm is proposed to make the most out of QFC processes.

Smart tailoring of the non-linear processes properties goes beyond addressing limitations and improving the state of the art. The spectral properties of non-linear processes can be exploited to implement TMs in photon states, a framework that allows one to encode information in the energy degree of freedom of photons. In chapter 7, the JSA function of a PDC process is engineered to produce a bi-photon state with a controlled number of maximally entangled TMs. The key is the dispersion engineering of a KTP waveguide and the spectral shaping of the pump field. The scheme is experimentally demonstrated, producing up to 6 maximally entangled dimensions in the bi-photon state. This first of a kind quantum light source sets a new precedent with applications in highly secure and high capacity quantum communication schemes.

Information encoded in TMs can be processed and read out using a QPG. This device that is shown to implement projection measurements on TMs is applied to three different quantum tasks in chapter 6. First, quantum single-parameter estimation is extended to a multi-parameter estimation technique. By implementing tailored phase-sensitive measurements with the QPG, the information of three parameters from the incoherent mixture of two pulses is retrieved. The results saturate the quantum bound as in the previously demonstrated single-parameter case.

Second, the presence of coherence in the pulse mixture is investigated to contribute to the recent debate. Different degrees of coherence are introduced into the mixture through spectral shaping to experimentally demonstrate its effect. The results show that coherence neither increases nor reduces the amount of information in the system. The information of the parameter estimators is simply redistributed into the different modes arisen from the presence of coherence.

Finally, the QPG is used in a new tomography technique to reconstruct photon states. RCT is introduced as a compressive sensing inspired scheme in which an unknown state is reconstructed from information accumulated through single-shot measurements. With this new method, we demonstrate state reconstruction fidelities above 80% while the number of measurements needed is an order of magnitude less than conventional scan tomography techniques. This remarkable results highlight once more the scalability and reconfigurability of the QPG as a temporal mode processor.

The results presented in this thesis aim at stressing the importance of looking at a problem from all sides possible. We are at the edge of a possible revolution, a quantum revolution that could change science and technology forever but to get there, we have to hop again on the shoulders of giants and understand the fundamentals of every new idea. From the history of science we can learn to never disregard any approach until the nature of a process is explained, and probably not even then.

Naturally, we have to look into the future as well. In the last two decades, the foundations of many real quantum technologies have been laid down and we have to keep moving forward. The PDC source presented here can still be improved if the shaping resolution limit is addressed, promising states with as high as 30 temporal modes. The enhanced QPG device has to be exploited and its improved mode selectivity applied to more quantum measurement schemes. Furthermore, the combination of the PDC source, QPG devices and for example quantum memories, could already be the base for a quantum network node. This node would source entangled photons that are stored and transmitted to another node while a QPG performs an efficient state tomography. Another QPG in the node could encode information by projecting the remaining PDC photons into a message. The quantum playground is set, we just need to never lose our curiosity and remember that science, even in failure, always moves forward.

Acknowledgements

> We are always more afraid than we wish to be, but we can always be braver than we expect.
>
> *"Sorilea" in the "Wheel of Time" by Robert Jordan*

It has been seven years since I arrived in Germany, starting the journey that led me to this thesis four and a half years ago. Through all these years, many people have made this possible with their support. With this humble words I want to thank everyone from the bottom of my heart[3].

First and foremost, I want to thank my supervisor, Christine. She gave me the opportunity to pursue a career in research to begin with. She trusted me, first with a bachelor's thesis and second with a master's that were decisive in bringing me into my PhD. This work would not have been possible without her deep insight and understanding of the field, and her careful guiding. She is a great group leader, one that recognizes the strongest suit of each person and makes sure they shine.

Next in line is Vahid, my "field" supervisor. We worked together for six years and I have to thank him for knowing all I know about experimental optics, the QPG and SLMs. I would not be half the scientist I am now without him. Over and above that, he is a kind, loving person, one that I'm proud to call friend. Thank you for everything, "El Vaho".

Many other people has helped and been there for me through the years. Sharing laboratory and work with Jhon was invigorating. He expels such a positive easy-going energy that makes nothing seem impossible. He is also an expert from which I learned many fundamentals and, coming from outside the group, different points of view on our projects. Markus was a lot of fun to share office with and I learned a lot from him too. Collaborating together in the Dortmund project, although only briefly, was a very enjoyable experience. In the last few years, since he came back from Albion, Benni has been a great support in my work. There are things that I would have never understood without his wisdom and I loved our conversations about random things whenever he came over to the office. Finally, working in the laboratory with Syam was very refreshing as he came from a different background and taught me different approaches to concepts I had set in stone.

In general, I have to thank everyone at the group for the amazingly welcoming working environment. It was really great that the group is so international. I have learnt so much about all your cultures! The group is a real treasure, one I trust you to keep nourishing for the years to come. Everyone was always ready to help with anything (work or personal related) and I shared pleasant discussions and conversations with all of you. As an immigrant, having a group of people to rely

[3] `https://bit.ly/32rhPlq`

on makes the difference between bearing with the distance from your loved ones and not. Believe me then, when I say that you were my abroad family and that I am immensely thankful with all of you, even if you weren't mentioned by name here.

There will always be a special place in my heart for Angelina, Marcello, Matteo, Michael and Tanya. Your friendship has been my energy source all these years. I don't know what would have been of me if I wouldn't have crossed paths with you. I will miss our board game nights, dinner parties, silly jokes and your company. Thank you for everything.

In the last year, many new PhD students joined the group. Although we have shared very little time (the pandemic to blame), I have greatly enjoyed it and I have learned a lot from you guys. Best of luck for you Dana, Laura, Federico, Franz and Patrick.

I would literally not be here if it weren't for my parents. Not only for the obvious biological reasons, but for their constant unconditional support and love. They nursed my curiosity and raised me to be the person that I am, for which I hope to make them proud. They have gone above and beyond to see me succeed and, because of that, this thesis is as much theirs as it is mine.

Last, but most definitely not least, I want to thank Natalia. This thesis wouldn't mean as much as it does if I wouldn't have been able to do it with her by my side. We made my dream of becoming a PhD part of our project and, knowing the price it would have, threw ourselves at it. Every letter in this work is written with the sheer force of our will to remain together, because we wanted to, because we love each other with no limit, over any distance and with unfettering confidence. Every single day of the last seven years I have known her by my side, felt her like my background radiation, and this has driven me forward. Her love has been my guiding light in this journey and it has never faltered. I love you Natalia, I am coming home.

Bibliography

[1] Oliver Heaviside. *Electromagnetic theory*. London: "The Electrician" Pub. Co., 1893.

[2] Lord Rayleigh. "XVIII. On the passage of electric waves through tubes, or the vibrations of dielectric cylinders". In: *London, Edinburgh, Dublin Philos. Mag. J. Sci.* 43.261 (Feb. 1897), pp. 125–132. ISSN: 1941-5982. DOI: 10.1080/14786449708620969.

[3] R C Alferness et al. *Guided-Wave Optoelectronics*. Ed. by Theodor Tamir. Vol. 26. Springer Series in Electronics and Photonics. Berlin, Heidelberg: Springer Berlin Heidelberg, 1988. ISBN: 978-3-642-97076-4. DOI: 10.1007/978-3-642-97074-0.

[4] Amnon Yariv and Pochi Yeh. *Photonics: optical electronics in modern communications (the oxford series in electrical and computer engineering)*. Oxford University Press, Inc., 2006, p. 696. ISBN: 0195179463.

[5] T. H. Maiman. "Stimulated Optical Radiation in Ruby". In: *Nature* 187.4736 (Aug. 1960), pp. 493–494. ISSN: 0028-0836. DOI: 10.1038/187493a0.

[6] P. A. Franken et al. "Generation of Optical Harmonics". In: *Phys. Rev. Lett.* 7.4 (Aug. 1961), p. 118. DOI: 10.1103/PhysRevLett.7.118.

[7] N. Bloembergen. "Nonlinear Optics: past, present and future". In: *Guid. Wave Nonlinear Opt.* (1992), pp. 1–9. DOI: 10.1007/978-94-011-2536-9_1.

[8] Robert W Boyd. "History of Research in Nonlinear Optics at The Institute of Optics". In: *A Jewel crown*. Ed. by Carlos R. Stroud and Gina A. Kern. Boydell & Brewer, University of Rochester Press, 2004. Chap. 56. Histor.

[9] Gilbert N. Lewis, David Lipkin, and Theodore T. Magel. "Reversible Photochemical Processes in Rigid Media. A Study of the Phosphorescent State". In: *J. Am. Chem. Soc.* 63.11 (Nov. 1941), pp. 3005–3018. ISSN: 0002-7863. DOI: 10.1021/ja01856a043.

[10] John Kerr. "XLIII. On rotation of the plane of polarization by reflection from the pole of a magnet". In: *London, Edinburgh, Dublin Philos. Mag. J. Sci.* 3.19 (May 1877), pp. 321–343. ISSN: 1941-5982. DOI: 10.1080/14786447708639245.

[11] John Kerr. "XXIV. On reflection of polarized light from the equatorial surface of a magnet". In: *London, Edinburgh, Dublin Philos. Mag. J. Sci.* 5.30 (Mar. 1878), pp. 161–177. ISSN: 1941-5982. DOI: 10.1080/14786447808639407.

[12] W. Kaiser and C. G. B. Garrett. "Two-Photon Excitation in Ca ¡math display="inline"¿ ¡mrow¿ ¡msub¿ ¡mrow¿ ¡mi mathvariant="normal"¿F¡/mi¿ ¡/mrow¿ ¡mrow¿ ¡mn¿2¡/mn¿ ¡/mrow¿ ¡/msub¿ ¡/mrow¿ ¡/math¿ : ¡math display="inline"¿ ¡mrow¿ ¡msup¿ ¡mrow¿ ¡mi mathvariant="normal"¿Eu¡/mi¿ ¡/mrow¿ ¡mro". In: *Phys. Rev. Lett.* 7.6 (Sept. 1961), pp. 229–231. ISSN: 0031-9007. DOI: 10.1103/PhysRevLett.7.229.

[13] J. A. Armstrong et al. "Interactions between Light Waves in a Nonlinear Dielectric". In: *Phys. Rev.* 127.6 (Sept. 1962), pp. 1918–1939. ISSN: 0031-899X. DOI: 10.1103/PhysRev.127.1918.

[14] N. Bloembergen and P. S. Pershan. "Light Waves at the Boundary of Nonlinear Media". In: *Phys. Rev.* 128.2 (Oct. 1962), pp. 606–622. ISSN: 0031-899X. DOI: 10.1103/PhysRev.128.606.

[15] D. B. Anderson and J. T. Boyd. "Wideband CO 2 Laser Second Harmonic Generation Phase Matched in GaAs Thin-Film Waveguides". In: *Appl. Phys. Lett.* 19.8 (Oct. 1971), pp. 266–268. ISSN: 0003-6951. DOI: 10.1063/1.1653912.

[16] George I. Stegeman and Roger H. Stolen. "Waveguides and fibers for nonlinear optics". In: *J. Opt. Soc. Am. B* 6.4 (Apr. 1989), p. 652. ISSN: 0740-3224. DOI: 10.1364/JOSAB.6.000652.

[17] Theo Hahn. *International Tables for Crystallography*. Ed. by Th. Hahn. Vol. A. International Tables for Crystallography. Chester, England: International Union of Crystallography, Oct. 2006. ISBN: 978-0-7923-6590-7. DOI: 10.1107/97809553602060000100.

[18] M. Yamada et al. "First-order quasi-phase matched LiNbO 3 waveguide periodically poled by applying an external field for efficient blue second-harmonic generation". In: *Appl. Phys. Lett.* 62.5 (Feb. 1993), pp. 435–436. ISSN: 0003-6951. DOI: 10.1063/1.108925.

[19] Shen Yue-Ron. *The principles of nonlinear optics*. Ed. by John Wiley & Sons Inc. New York: John Wiley & Sons Inc, 2002, p. 576. ISBN: 978-0-471-43080-3.

[20] Giulio Cerullo and Sandro De Silvestri. "Ultrafast optical parametric amplifiers". In: *Rev. Sci. Instrum.* 74.1 (Jan. 2003), pp. 1–18. ISSN: 0034-6748. DOI: 10.1063/1.1523642.

[21] E. Herlinger. "Untersuchungen über die Kristallstruktur von Sesquioxyden und Verbindungen ABO3,. Von W. H. Zachariasen. Skrifter utgitt av Det Norske Videnskap-Akademi i Oslo, I. Mat.-Naturw. Klasse 1928, Nr. 4. Oslo, in Kommission bei J. Dybwad 1928. Kr. 12,—". In: *Zeitschrift für Angew. Chemie* 42.30 (July 1929), pp. 797–797. ISSN: 00448249. DOI: 10.1002/ange.19290423015.

[22] Dieter H. Jundt. "Temperature-dependent Sellmeier equation for the index of refraction, n_e, in congruent lithium niobate". In: *Opt. Lett.* 22.20 (Oct. 1997), p. 1553. ISSN: 0146-9592. DOI: 10.1364/OL.22.001553.

[23] G. J. Edwards and M. Lawrence. "A temperature-dependent dispersion equation for congruently grown lithium niobate". In: *Opt. Quantum Electron.* 16.4 (July 1984), pp. 373–375. ISSN: 0306-8919. DOI: 10.1007/BF00620081.

[24] David N. Nikogosyan. *Nonlinear optical crystals: a complete survey*. Springer, 2005.

[25] P. A. Augstov and K. K. Shvarts. "The temperature and light intensity dependence of photorefraction in LiNbO3". In: *Appl. Phys.* 21.2 (Feb. 1980), pp. 191–194. ISSN: 0340-3793. DOI: 10.1007/BF00900683.

[26] E. Strake, G.P. Bava, and I. Montrosset. "Guided modes of Ti:LiNbO/sub 3/ channel waveguides: a novel quasi-analytical technique in comparison with the scalar finite-element method". In: *J. Light. Technol.* 6.6 (June 1988), pp. 1126–1135. ISSN: 07338724. DOI: 10.1109/50.4105.

[27] L. Ouvrard and M. Troost. "Rechearches sur les phosphates doubles de titane, d'etain et de cuivre". In: *Compt Rend* 111 (1890), pp. 177–179.

[28] Kiyoshi Kato and Eiko Takaoka. "Sellmeier and thermo-optic dispersion formulas for KTP". In: *Appl. Opt.* 41.24 (Aug. 2002), p. 5040. ISSN: 0003-6935. DOI: 10.1364/AO.41.005040.

[29] Georg Harder et al. "An optimized photon pair source for quantum circuits". In: *Opt. Express* 21.12 (June 2013), p. 13975. ISSN: 1094-4087. DOI: 10.1364/OE.21.013975.

[30] B. Boulanger et al. "Relative sign and absolute magnitude of d (2) nonlinear coefficients of KTP from second-harmonic-generation measurements". In: *J. Opt. Soc. Am. B* 11.5 (May 1994), p. 750. ISSN: 0740-3224. DOI: 10.1364/JOSAB.11.000750.

[31] L.K. Cheng et al. "Crystal growth and characterization of KTiOPO4 isomorphs from the self-fluxes". In: *J. Cryst. Growth* 137.1-2 (Mar. 1994), pp. 107–115. ISSN: 00220248. DOI: 10.1016/0022-0248(94)91256-4.

[32] John D. Bierlein et al. "Fabrication and characterization of optical waveguides in KTiOPO 4". In: *Appl. Phys. Lett.* 50.18 (May 1987), pp. 1216–1218. ISSN: 0003-6951. DOI: 10.1063/1.97913.

[33] Patrick T. Callahan et al. "Fiber-coupled balanced optical cross-correlator using PPKTP waveguides". In: *Opt. Express* 22.8 (Apr. 2014), p. 9749. ISSN: 1094-4087. DOI: 10.1364/OE.22.009749.

[34] Matteo Santandrea. "Design of nonlinear integrated devices for quantum optics applications". Doctoral dissertation. Paderborn University, 2019, p. 210. DOI: 10.17619/UNIPB/1-835.

[35] Sten Helmfrid, Gunnar Arvidsson, and Jonas Webjörn. "Influence of various imperfections on the conversion efficiency of second-harmonic generation in quasi-phase-matching lithium niobate waveguides". In: *J. Opt. Soc. Am. B* 10.2 (Feb. 1993), p. 222. ISSN: 0740-3224. DOI: 10.1364/JOSAB.10.000222.

[36] Laszlo Solymar. *Getting the message - A history of communications*. Oxford University Press, 1999.

[37] GE Moore. "Cramming more components onto integrated circuits". In: *Electron. Mag.* (1965).

[38] Stephen Wiesner. "Conjugate coding". In: *ACM SIGACT News* 15.1 (Jan. 1983), pp. 78–88. ISSN: 0163-5700. DOI: 10.1145/1008908.1008920.

[39] James L. Park. "The concept of transition in quantum mechanics". In: *Found. Phys.* 1.1 (1970), pp. 23–33. ISSN: 0015-9018. DOI: 10.1007/BF00708652.

[40] A. Holevo. "Bounds for the quantity of information transmitted by a quantum communication channel". In: *Probl. Peredachi Inf.* 9.3 (1973).

[41] Paul Benioff. "The computer as a physical system: A microscopic quantum mechanical Hamiltonian model of computers as represented by Turing machines". In: *J. Stat. Phys.* 22.5 (May 1980), pp. 563–591. ISSN: 0022-4715. DOI: 10.1007/BF01011339.

[42] Richard P. Feynman. "Simulating physics with computers". In: *Int. J. Theor. Phys.* 21.6-7 (June 1982), pp. 467–488. ISSN: 0020-7748. DOI: 10.1007/BF02650179.

[43] Roman S. Ingarden. "Quantum information theory". In: *Reports Math. Phys.* 10.1 (Aug. 1976), pp. 43–72. ISSN: 00344877. DOI: 10.1016/0034-4877(76)90005-7.

[44] Charles H. Bennett and Gilles Brassard. "Quantum cryptography: Public key distribution and coin tossing". In: *Theor. Comput. Sci.* 560 (Dec. 2014), pp. 7–11. ISSN: 03043975. DOI: 10.1016/j.tcs.2014.05.025.

[45] John Preskill. "Quantum computing and the entanglement frontier". In: *arXiv* arXiv:1203.5813 (Mar. 2012). arXiv: 1203.5813.

[46] John Preskill. *Why I Called It 'Quantum Supremacy' — Quanta Magazine*. URL: https://www.quantamagazine.org/john-preskill-explains-quantum-supremacy-20191002/ (visited on 11/08/2021).

[47] Gianfranco Cariolaro. *Quantum Communications*. Signals and Communication Technology. Cham: Springer International Publishing, 2015. ISBN: 978-3-319-15599-9. DOI: 10.1007/978-3-319-15600-2.

[48] P A M Dirac. *The Principles of Quantum Mechanics (1995 reprint of 4th ed)*. 4th ed. USA: Oxford University Press, 1930. ISBN: 0198520115.

[49] Paul G. Kwiat et al. "New high-intensity source of polarization-entangled photon pairs". In: *Phys. Rev. Lett.* 75.24 (1995), pp. 4337–4341. ISSN: 00319007. DOI: 10.1103/PhysRevLett.75.4337.

[50] B. Brecht et al. "Photon temporal modes: A complete framework for quantum information science". In: *Phys. Rev. X* 5.4 (2015), pp. 1–13. ISSN: 21603308. DOI: 10.1103/PhysRevX.5.041017. arXiv: 1504.06251.

[51] W. H. Louisell, A. Yariv, and A. E. Siegman. "Quantum Fluctuations and Noise in Parametric Processes. I." In: *Phys. Rev.* 124.6 (Dec. 1961), pp. 1646–1654. ISSN: 0031-899X. DOI: 10.1103/PhysRev.124.1646.

[52] J. P. Gordon, W. H. Louisell, and L. R. Walker. "Quantum Fluctuations and Noise in Parametric Processes. II". In: *Phys. Rev.* 129.1 (Jan. 1963), pp. 481–485. ISSN: 0031-899X. DOI: 10.1103/PhysRev.129.481.

[53] S. E. Harris, M. K. Oshman, and R. L. Byer. "Observation of Tunable Optical Parametric Fluorescence". In: *Phys. Rev. Lett.* 18.18 (May 1967), pp. 732–734. ISSN: 0031-9007. DOI: 10.1103/PhysRevLett.18.732.

[54] Douglas Magde and Herbert Mahr. "Study in Ammonium Dihydrogen Phosphate of Spontaneous Parametric Interaction Tunable from 4400 to 16 000 Å". In: *Phys. Rev. Lett.* 18.21 (May 1967), p. 905. DOI: 10.1103/PhysRevLett.18.905.

[55] Mikhail I. Kolobov. "The spatial behavior of nonclassical light". In: *Rev. Mod. Phys.* 71.5 (Oct. 1999), pp. 1539–1589. ISSN: 0034-6861. DOI: 10.1103/RevModPhys.71.1539.

[56] K. J. Blow et al. "Continuum fields in quantum optics". In: *Phys. Rev. A* 42.7 (Oct. 1990), p. 4102. DOI: 10.1103/PhysRevA.42.4102.

[57] W. P. Grice and I. A. Walmsley. "Spectral information and distinguishability in type-II down-conversion with a broadband pump". In: *Phys. Rev. A* 56.2 (Aug. 1997), pp. 1627–1634. ISSN: 1050-2947. DOI: 10.1103/PhysRevA.56.1627.

[58] C. K. Law, I. A. Walmsley, and J. H. Eberly. "Continuous Frequency Entanglement: Effective Finite Hilbert Space and Entropy Control". In: *Phys. Rev. Lett.* 84.23 (June 2000), pp. 5304–5307. ISSN: 0031-9007. DOI: 10.1103/PhysRevLett.84.5304.

[59] Andreas Eckstein, Benjamin Brecht, and Christine Silberhorn. "A quantum pulse gate based on spectrally engineered sum frequency generation". In: *Opt. Express* 19.15 (July 2011), p. 13770. ISSN: 1094-4087. DOI: 10.1364/OE.19.013770.

[60] D. V. Reddy, M. G. Raymer, and C. J. McKinstrie. "Efficient sorting of quantum-optical wave packets by temporal-mode interferometry". In: *Opt. Lett.* 39.10 (May 2014), p. 2924. ISSN: 0146-9592. DOI: 10.1364/OL.39.002924.

[61] D. V. Reddy, M. G. Raymer, and C. J. McKinstrie. "Sorting photon wave packets using temporal-mode interferometry based on multiple-stage quantum frequency conversion". In: *Phys. Rev. A* 91.1 (Jan. 2015), p. 012323. ISSN: 1050-2947. DOI: 10.1103/PhysRevA.91.012323.

[62] Markus Allgaier et al. "Highly efficient frequency conversion with bandwidth compression of quantum light". In: *Nat. Commun.* 8.1 (Jan. 2017), pp. 1–6. ISSN: 20411723. DOI: 10.1038/ncomms14288. arXiv: 1610.08326.

[63] D. V. Reddy et al. "Temporal mode selectivity by frequency conversion in second-order nonlinear optical waveguides". In: *Opt. Express* 21.11 (June 2013), p. 13840. ISSN: 1094-4087. DOI: 10.1364/OE.21.013840. arXiv: 1305.2165.

[64] H. J. Kimble. *The quantum internet*. June 2008. DOI: 10.1038/nature07127. arXiv: 0806.4195.

[65] Sergei Slussarenko and Geoff J. Pryde. "Photonic quantum information processing: A concise review". In: *Appl. Phys. Rev.* 6.4 (Dec. 2019), p. 041303. ISSN: 1931-9401. DOI: 10.1063/1.5115814.

[66] David P. DiVincenzo. "The Physical Implementation of Quantum Computation". In: *Prog. Phys.* 48.(9-11) (2000), pp. 771–783.

[67] Andreas Christ et al. "Probing multimode squeezing with correlation functions". In: *New J. Phys.* 13.3 (Mar. 2011), p. 033027. ISSN: 1367-2630. DOI: 10.1088/1367-2630/13/3/033027.

[68] Andreas Eckstein et al. "Realistic g(2) measurement of a PDC source with single photon detectors in the presence of background". In: *Phys. status solidi* 8.4 (Apr. 2011), pp. 1216–1219. ISSN: 18626351. DOI: 10.1002/pssc.201000876.

[69] P Grünwald. "Effective second-order correlation function and single-photon detection". In: *New J. Phys.* 21.9 (Sept. 2019), p. 093003. ISSN: 1367-2630. DOI: 10.1088/1367-2630/ab3ae0.

[70] Natasha Tomm et al. "A bright and fast source of coherent single photons". In: *Nat. Nanotechnol.* 16.4 (Apr. 2021), pp. 399–403. ISSN: 1748-3387. DOI: 10.1038/s41565-020-00831-x.

[71] Yating Lin, Yongzheng Ye, and Wei Fang. "Electrically driven single-photon sources". In: *J. Semicond.* 40.7 (July 2019), p. 071904. ISSN: 1674-4926. DOI: 10.1088/1674-4926/40/7/071904.

[72] Evan Meyer-Scott, Christine Silberhorn, and Alan Migdall. "Single-photon sources: Approaching the ideal through multiplexing". In: *Rev. Sci. Instrum.* 91.4 (Apr. 2020), p. 041101. ISSN: 0034-6748. DOI: 10.1063/5.0003320.

[73] Alexander Pickston et al. "Optimised domain-engineered crystals for pure telecom photon sources". In: *Opt. Express* 29.5 (Mar. 2021), p. 6991. ISSN: 1094-4087. DOI: 10.1364/OE.416843.

[74] Fumihiro Kaneda et al. "Heralded single-photon source utilizing highly nondegenerate, spectrally factorable spontaneous parametric downconversion". In: *Opt. Express* 24.10 (May 2016), p. 10733. ISSN: 1094-4087. DOI: 10.1364/OE.24.010733.

[75] Han-Sen Zhong et al. "12-Photon Entanglement and Scalable Scattershot Boson Sampling with Optimal Entangled-Photon Pairs from Parametric Down-Conversion". In: *Phys. Rev. Lett.* 121.25 (Dec. 2018), p. 250505. ISSN: 0031-9007. DOI: 10.1103/PhysRevLett.121.250505.

[76] C. Simon et al. "Quantum memories". In: *Eur. Phys. J. D* 58.1 (May 2010), pp. 1–22. ISSN: 1434-6060. DOI: 10.1140/epjd/e2010-00103-y.

[77] Khabat Heshami et al. "Quantum memories: emerging applications and recent advances". In: *J. Mod. Opt.* 63.20 (Nov. 2016), pp. 2005–2028. ISSN: 0950-0340. DOI: 10.1080/09500340.2016.1148212.

[78] Andreas Christ et al. "Theory of quantum frequency conversion and type-II parametric down-conversion in the high-gain regime". In: *New J. Phys.* 15.5 (May 2013), p. 053038. ISSN: 1367-2630. DOI: 10.1088/1367-2630/15/5/053038. arXiv: 1210.8342. URL: http://stacks.iop.org/1367-2630/15/i=5/a=053038?key=crossref.eccf8b249f720790a365b2d469500449%20http://www.njp.org/.

[79] Benjamin Brecht et al. "Demonstration of coherent time-frequency Schmidt mode selection using dispersion-engineered frequency conversion". In: *Phys. Rev. A* 90.3 (Sept. 2014), p. 030302. ISSN: 1050-2947. DOI: 10.1103/PhysRevA.90.030302.

[80] Vahid Ansari et al. "Temporal-mode measurement tomography of a quantum pulse gate". In: *Phys. Rev. A* 96.6 (Dec. 2017), p. 063817. ISSN: 24699934. DOI: 10.1103/PhysRevA.96.063817. arXiv: 1702.03336.

[81] J. M. Donohue et al. "Quantum-Limited Time-Frequency Estimation through Mode-Selective Photon Measurement". In: *Phys. Rev. Lett.* 121.9 (Aug. 2018), p. 090501. ISSN: 0031-9007. DOI: 10.1103/PhysRevLett.121.090501.

[82] M. Allgaier et al. "Pulse shaping using dispersion-engineered difference frequency generation". In: *Phys. Rev. A* 101.4 (Apr. 2020), p. 043819. ISSN: 24699934. DOI: 10.1103/PhysRevA.101.043819. arXiv: 1812.07904.

[83] Aaron P. VanDevender and Paul G. Kwiat. "High-efficiency single photon detection via frequency up-conversion". In: ed. by Eric Donkor, Andrew R. Pirich, and Howard E. Brandt. Aug. 2003, p. 216. DOI: 10.1117/12.487082.

[84] J. S. Pelc et al. "Long-wavelength-pumped upconversion single-photon detector at 1550 nm: performance and noise analysis". In: *Opt. Express* 19.22 (Oct. 2011), p. 21445. ISSN: 1094-4087. DOI: 10.1364/oe.19.021445.

[85] Abijith S. Kowligy et al. "Quantum optical arbitrary waveform manipulation and measurement in real time". In: *Opt. Express* 22.23 (Nov. 2014), p. 27942. ISSN: 1094-4087. DOI: 10.1364/OE.22.027942.

[86] J Gil-Lopez et al. "Improved non-linear devices for quantum applications". In: *New J. Phys.* 23.6 (June 2021), p. 063082. ISSN: 1367-2630. DOI: 10.1088/1367-2630/AC09FD. URL: https://iopscience.iop.org/article/10.1088/1367-2630/ac09fd%20https://iopscience.iop.org/article/10.1088/1367-2630/ac09fd/meta.

[87] Nicolás Quesada and J. E. Sipe. "High efficiency in mode-selective frequency conversion". In: *Opt. Lett.* 41.2 (Jan. 2016), p. 364. ISSN: 0146-9592. DOI: 10.1364/ol.41.000364.

[88] Vahid Ansari et al. "Achieving the Ultimate Quantum Timing Resolution". In: *PRX Quantum* 2.1 (Jan. 2021), p. 010301. ISSN: 2691-3399. DOI: 10.1103/PRXQuantum.2.010301.

[89] Matteo Santandrea et al. "Fabrication limits of waveguides in nonlinear crystals and their impact on quantum optics applications". In: *New J. Phys.* 21.3 (Mar. 2019), p. 033038. ISSN: 1367-2630. DOI: 10.1088/1367-2630/aaff13.

[90] Matteo Santandrea, Michael Stefszky, and Christine Silberhorn. "General framework for the analysis of imperfections in nonlinear systems". In: *Opt. Lett.* 44.22 (Nov. 2019), p. 5398. ISSN: 0146-9592. DOI: 10.1364/OL.44.005398.

[91] Nicolas J. Cerf et al. "Security of Quantum Key Distribution Using d-Level Systems". In: *Phys. Rev. Lett.* 88.12 (Mar. 2002), p. 127902. ISSN: 0031-9007. DOI: 10.1103/PhysRevLett.88.127902.

[92] Thomas Brougham and Stephen M. Barnett. "Information communicated by entangled photon pairs". In: *Phys. Rev. A - At. Mol. Opt. Phys.* 85.3 (Mar. 2012). ISSN: 10502947. DOI: 10.1103/PhysRevA.85.032322. arXiv: 1203.1537.

[93] Daniele Cozzolino et al. "High-Dimensional Quantum Communication: Benefits, Progress, and Future Challenges". In: *Adv. Quantum Technol.* 2.12 (Dec. 2019), p. 1900038. ISSN: 2511-9044. DOI: 10.1002/QUTE.201900038.

[94] S. Etcheverry et al. "Quantum key distribution session with 16-dimensional photonic states". In: *Sci. Rep.* 3 (2013). ISSN: 20452322. DOI: 10.1038/srep02316.

[95] Syamsundar De et al. "Effects of coherence on temporal resolution". In: *Phys. Rev. Res.* 3.3 (July 2021), p. 033082. ISSN: 2643-1564. DOI: 10.1103/PhysRevResearch.3.033082.

[96] Matteo Santandrea et al. "Interferometric method for determining the losses of spatially multi-mode nonlinear waveguides based on second harmonic generation". In: *Opt. Express* 28.4 (Feb. 2020), p. 5507. ISSN: 1094-4087. DOI: 10.1364/oe.380788. arXiv: 1910.07300.

[97] Derek Chang et al. "Complex-transfer-function analysis of optical-frequency converters". In: *Conf. Lasers Electro-Optics Eur. - Tech. Dig.* Vol. 2014-Janua. 17. Institute of Electrical and Electronics Engineers Inc., Sept. 2014, pp. 5106–5109. DOI: 10.1364/ol.39.005106.

[98] Yongsheng Fang and Jun Li. "A review of tournament selection in genetic programming". In: *Lect. Notes Comput. Sci. (including Subser. Lect. Notes Artif. Intell. Lect. Notes Bioinformatics)*. Vol. 6382 LNCS. M4D. Springer, Berlin, Heidelberg, Oct. 2010, pp. 181–192. ISBN: 3642164927. DOI: 10.1007/978-3-642-16493-4_19.

[99] Yeung Lak Lee et al. "Reshaping of a second-harmonic curve in periodically poled Ti:LiNbO3 channel waveguide by a local-temperature-control technique". In: *Appl. Phys. Lett.* 86.1 (Jan. 2005), p. 011104. ISSN: 0003-6951. DOI: 10.1063/1.1842854.

[100] T. C. Ralph et al. "Photon Sorting, Efficient Bell Measurements, and a Deterministic Controlled-Z Gate Using a Passive Two-Level Nonlinearity". In: *Phys. Rev. Lett.* 114.17 (Apr. 2015), p. 173603. ISSN: 0031-9007. DOI: 10.1103/PhysRevLett.114.173603.

[101] P Sutton. "Introduction to Fourier Optics". In: *Quantum Semiclassical Opt. J. Eur. Opt. Soc. Part B* 8.5 (Oct. 1996). ISSN: 1355-5111. DOI: 10.1088/1355-5111/8/5/014.

[102] M.B. Danailov and I.P. Christov. "Time-space Shaping of Light Pulses by Fourier Optical Processing". In: *J. Mod. Opt.* 36.6 (June 1989), pp. 725–731. ISSN: 0950-0340. DOI: 10.1080/09500348914550811.

[103] Antoine Monmayrant, Sébastien Weber, and Béatrice Chatel. "A newcomer's guide to ultrashort pulse shaping and characterization". In: *J. Phys. B At. Mol. Opt. Phys.* 43.10 (May 2010), p. 103001. ISSN: 09534075. DOI: 10.1088/0953-4075/43/10/103001.

[104] W. Gao et al. "Measurement technologies for precision positioning". In: *CIRP Ann.* 64.2 (2015), pp. 773–796. ISSN: 00078506. DOI: 10.1016/j.cirp.2015.05.009.

[105] Wooram Kim et al. "Absolute laser ranging by time-of-flight measurement of ultrashort light pulses [Invited]". In: *J. Opt. Soc. Am. A* 37.9 (Sept. 2020), B27. ISSN: 1084-7529. DOI: 10.1364/JOSAA.395157.

[106] Bingying Chen et al. "Extended depth of focus multiphoton microscopy via incoherent pulse splitting". In: *Biomed. Opt. Express* 11.7 (July 2020), p. 3830. ISSN: 2156-7085. DOI: 10.1364/BOE.393931.

[107] Ferenc Krausz and Misha Ivanov. "Attosecond physics". In: *Rev. Mod. Phys.* 81.1 (Feb. 2009), pp. 163–234. ISSN: 0034-6861. DOI: 10.1103/RevModPhys.81.163.

[108] E. Abbe. "Beiträge zur Theorie des Mikroskops und der mikroskopischen Wahrnehmung". In: *Arch. für Mikroskopische Anat.* 9.1 (Dec. 1873), pp. 413–468. ISSN: 0176-7364. DOI: 10.1007/BF02956173.

[109] Rayleigh. "XXXI. Investigations in optics, with special reference to the spectroscope". In: *London, Edinburgh, Dublin Philos. Mag. J. Sci.* 8.49 (Oct. 1879), pp. 261–274. ISSN: 1941-5982. DOI: 10.1080/14786447908639684.

[110] R. A. Fisher. "On the mathematical foundations of theoretical statistics". In: *Philos. Trans. R. Soc. London. Ser. A, Contain. Pap. a Math. or Phys. Character* 222.594-604 (Jan. 1922), pp. 309–368. ISSN: 0264-3952. DOI: 10.1098/rsta.1922.0009.

[111] R. A. Fisher. "Theory of Statistical Estimation". In: *Math. Proc. Cambridge Philos. Soc.* 22.5 (July 1925), pp. 700–725. ISSN: 0305-0041. DOI: 10.1017/S0305004100009580.

[112] L. Motka et al. "Optical resolution from Fisher information". In: *Eur. Phys. J. Plus* 131.5 (May 2016), p. 130. ISSN: 2190-5444. DOI: 10.1140/epjp/i2016-16130-7.

[113] Harald Cramer. *A New Approach to Probability Theory with Reference to Statistics and Statistical Physics*. Princeton: Princeton University Press, 1946.

[114] C. Radhakrishna Rao. "Information and the Accuracy Attainable in the Estimation of Statistical Parameters". In: 1992, pp. 235–247. DOI: 10.1007/978-1-4612-0919-5_16.

[115] Carl W. Helstrom. "Quantum detection and estimation theory". In: *J. Stat. Phys.* 1.2 (1969), pp. 231–252. ISSN: 0022-4715. DOI: 10.1007/BF01007479.

[116] D Petz and C Ghinea. "Introduction to quantum Fisher information". In: *Quantum Probab. Relat. Top.* WORLD SCIENTIFIC, Jan. 2011, pp. 261–281. ISBN: 978-981-4338-73-8. DOI: 10.1142/9789814338745_0015.

[117] Mankei Tsang, Ranjith Nair, and Xiao-Ming Lu. "Quantum Theory of Superresolution for Two Incoherent Optical Point Sources". In: *Phys. Rev. X* 6.3 (Aug. 2016), p. 031033. ISSN: 2160-3308. DOI: 10.1103/PhysRevX.6.031033.

[118] J. Rehacek et al. "Optimal measurements for resolution beyond the Rayleigh limit". In: *Opt. Lett.* 42.2 (Jan. 2017), p. 231. ISSN: 0146-9592. DOI: 10.1364/OL.42.000231.

[119] J. Řehaček et al. "Multiparameter quantum metrology of incoherent point sources: Towards realistic superresolution". In: *Phys. Rev. A* 96.6 (Dec. 2017), p. 062107. ISSN: 2469-9926. DOI: 10.1103/PhysRevA.96.062107.

[120] Alexander S. Holevo. *Probabilistic and statistical aspects of quantum theory*. Springer Science \& Business Media, 2011.

[121] Walker Larson and Bahaa E. A. Saleh. "Resurgence of Rayleigh's curse in the presence of partial coherence". In: *Optica* 5.11 (Nov. 2018), p. 1382. ISSN: 2334-2536. DOI: 10.1364/OPTICA.5.001382.

[122] Mankei Tsang and Ranjith Nair. "Resurgence of Rayleigh's curse in the presence of partial coherence: comment". In: *Optica* 6.4 (Apr. 2019), p. 400. ISSN: 2334-2536. DOI: 10.1364/OPTICA.6.000400.

[123] Walker Larson and Bahaa E. A. Saleh. "Resurgence of Rayleigh's curse in the presence of partial coherence: reply". In: *Optica* 6.4 (Apr. 2019), p. 402. ISSN: 2334-2536. DOI: 10.1364/OPTICA.6.000402.

[124] Zdeněk Hradil et al. "Quantum Fisher information with coherence". In: *Optica* 6.11 (Nov. 2019), p. 1437. ISSN: 2334-2536. DOI: 10.1364/OPTICA.6.001437.

[125] Kevin Liang, S. A. Wadood, and A. N. Vamivakas. "Coherence effects on estimating two-point separation". In: *Optica* 8.2 (Feb. 2021), p. 243. ISSN: 2334-2536. DOI: 10.1364/OPTICA.403497.

[126] S. A. Wadood et al. "Experimental demonstration of superresolution of partially coherent light sources using parity sorting". In: *Opt. Express* 29.14 (July 2021), p. 22034. ISSN: 1094-4087. DOI: 10.1364/OE.427734.

[127] Mankei Tsang. "Poisson Quantum Information". In: *Quantum* 5 (Aug. 2021), p. 527. ISSN: 2521-327X. DOI: 10.22331/q-2021-08-19-527.

[128] Kevin Liang, S. A. Wadood, and A. N. Vamivakas. "Coherence effects on estimating general sub-Rayleigh object distribution moments". In: *Phys. Rev. A* 104.2 (Aug. 2021), p. 022220. ISSN: 2469-9926. DOI: 10.1103/PhysRevA.104.022220.

[129] J.B. Altepeter, E.R. Jeffrey, and P.G. Kwiat. "Photonic State Tomography". In: 2005, pp. 105–159. DOI: 10.1016/S1049-250X(05)52003-2.

[130] Ermes Toninelli et al. "Concepts in quantum state tomography and classical implementation with intense light: a tutorial". In: *Adv. Opt. Photonics* 11.1 (Mar. 2019), p. 67. ISSN: 1943-8206. DOI: 10.1364/AOP.11.000067.

[131] Jano Gil-Lopez et al. "Universal compressive tomography in the time-frequency domain". In: *Optica* 8.10 (Oct. 2021), p. 1296. ISSN: 2334-2536. DOI: 10.1364/OPTICA.427645.

[132] J. Paye. "The chronocyclic representation of ultrashort light pulses". In: *IEEE J. Quantum Electron.* 28.10 (1992), pp. 2262–2273. ISSN: 00189197. DOI: 10.1109/3.159533.

[133] Ludmila Praxmeyer and Krzysztof Wodkiewicz. "Time and Frequency description of Optical Pulses". In: *Laser Phys.* 15.10 (Feb. 2005), p. 1477. DOI: arXiv:physics/0502079. arXiv: 0502079 [physics].

[134] Benjamin Brecht and Christine Silberhorn. "Characterizing entanglement in pulsed parametric down-conversion using chronocyclic Wigner functions". In: *Phys. Rev. A* 87.5 (May 2013), p. 053810. ISSN: 1050-2947. DOI: 10.1103/PhysRevA.87.053810.

[135] Poolad Imany et al. "50-GHz-spaced comb of high-dimensional frequency-bin entangled photons from an on-chip silicon nitride microresonator". In: *Opt. Express* 26.2 (Jan. 2018), p. 1825. ISSN: 1094-4087. DOI: 10.1364/OE.26.001825.

[136] Joseph M. Lukens. "Frequency bins for quantum information processing". In: *Photonics Quantum Work. 2019*. SPIE, Aug. 2021, p. 32. ISBN: 9781510647022. DOI: 10.1117/12.2610700.

[137] Tara Fortier and Esther Baumann. "20 years of developments in optical frequency comb technology and applications". In: *Commun. Phys.* 2.1 (Dec. 2019), p. 153. ISSN: 2399-3650. DOI: 10.1038/s42005-019-0249-y.

[138] Maroua Taghouti. "Compressed sensing". In: *Comput. Commun. Networks*. Elsevier, 2020, pp. 197–215. DOI: 10.1016/B978-0-12-820488-7.00023-2.

[139] Jaroslav Řeháček et al. "Diluted maximum-likelihood algorithm for quantum tomography". In: *Phys. Rev. A* 75.4 (Apr. 2007), p. 042108. ISSN: 1050-2947. DOI: 10.1103/PhysRevA.75.042108.

[140] Yong Siah Teo et al. "Quantum-State Reconstruction by Maximizing Likelihood and Entropy". In: *Phys. Rev. Lett.* 107.2 (July 2011), p. 020404. ISSN: 0031-9007. DOI: 10.1103/PhysRevLett.107.020404.

[141] Jiangwei Shang, Zhengyun Zhang, and Hui Khoon Ng. "Superfast maximum-likelihood reconstruction for quantum tomography". In: *Phys. Rev. A* 95.6 (June 2017), p. 062336. ISSN: 2469-9926. DOI: 10.1103/PhysRevA.95.062336.

[142] J Shang and Z Zhang. "Efficient MATLAB routines for quantum tomography". In: *Github* (2017).

[143] D. Ahn et al. "Adaptive Compressive Tomography with No a priori Information". In: *Phys. Rev. Lett.* 122.10 (Mar. 2019), p. 100404. ISSN: 0031-9007. DOI: 10.1103/PhysRevLett.122.100404.

[144] Rui Bo Jin et al. "Simple method of generating and distributing frequency-entangled qudits". In: *Quantum Sci. Technol.* 1.1 (Aug. 2016). ISSN: 20589565. DOI: 10.1088/2058-9565/1/1/015004.

[145] M. A. Finger et al. "Characterization and shaping of the time-frequency Schmidt mode spectrum of bright twin beams generated in gas-filled hollow-core photonic crystal fibers". In: *Phys. Rev. A* 95.5 (May 2017). ISSN: 24699934. DOI: 10.1103/PhysRevA.95.053814.

[146] N. Gisin and H. Bechmann-Pasquinucci. "Bell inequality, Bell states and maximally entangled states for n qubits". In: *Phys. Lett. Sect. A Gen. At. Solid State Phys.* 246.1-2 (Sept. 1998), pp. 1–6. ISSN: 03759601. DOI: 10.1016/S0375-9601(98)00516-7. arXiv: 9804045 [quant-ph].

[147] Thomas Durt et al. "Security of quantum key distributions with entangled qudits". In: *Phys. Rev. A - At. Mol. Opt. Phys.* 69.3 (Mar. 2004). ISSN: 10502947. DOI: 10.1103/PhysRevA.69.032313.

[148] Adetunmise C. Dada et al. "Experimental high-dimensional two-photon entanglement and violations of generalized Bell inequalities". In: *Nat. Phys.* 7.9 (2011), pp. 677–680. ISSN: 17452481. DOI: 10.1038/nphys1996. arXiv: 1104.5087.

[149] Christof Bernhard et al. "Shaping frequency-entangled qudits". In: *Phys. Rev. A - At. Mol. Opt. Phys.* 88.3 (Sept. 2013). ISSN: 10502947. DOI: 10.1103/PhysRevA.88.032322. arXiv: 1303.6202.

[150] Vahid Ansari et al. "Tailoring nonlinear processes for quantum optics with pulsed temporal-mode encodings". In: *Optica* (2018). DOI: 10.1364/OPTICA.5.000534.

[151] G. Patera et al. "Quantum coherent control of highly multipartite continuous-variable entangled states by tailoring parametric interactions". In: *Eur. Phys. J. D* 66.9 (Sept. 2012). ISSN: 14346060. DOI: 10.1140/epjd/e2012-30036-2.

[152] Bruno Robillart et al. "Spectral and temporal phase measurement by optical frequency-domain reflectometry". In: ed. by Siddharth Ramachandran. Mar. 2014, p. 896134. DOI: 10.1117/12.2039600.

[153] Alex O. C. Davis et al. "Measuring the Single-Photon Temporal-Spectral Wave Function". In: *Phys. Rev. Lett.* 121.8 (Aug. 2018), p. 083602. ISSN: 0031-9007. DOI: 10.1103/PhysRevLett.121.083602.

[154] Minas Sukiasyan et al. "Measurement of the ultrashort pulse spectral phase based on dispersive Fourier transformation". In: *Appl. Opt.* 58.11 (Apr. 2019), p. 2817. ISSN: 1559-128X. DOI: 10.1364/AO.58.002817.

[155] Malte Avenhaus et al. "Fiber-assisted single-photon spectrograph". In: *Opt. Lett.* 34.18 (Sept. 2009), p. 2873. ISSN: 0146-9592. DOI: 10.1364/OL.34.002873.

[156] P. R. Tapster and J. G. Rarity. "Photon statistics of pulsed parametric light". In: *J. Mod. Opt.* 45.3 (Mar. 1998), pp. 595–604. ISSN: 0950-0340. DOI: 10.1080/09500349808231917.